Heat Extraction for the CSPonD Thermal Storage Unit

MASSACHUSETTS INSTITUTE OF TECHNOLOGY
MAY 18 2011
LIBRARIES
ARCHIVES

by

Folkers Eduardo Rojas

Submitted to the Department of Mechanical on December 8, 2010 in partial fulfillment of the requirements for the degree of

Master of Science in Mechanical Engineering

at the

MASSACHUSETTS INSTITUTE OF TECHNOLOGY

February 2011

© Folkers Eduardo Rojas. All rights reserved.

The author hereby grants to MIT permission to reproduce and distribute publicly paper and electronic copies of this thesis document in whole or in part.

Author .....
Department of Mechanical Engineering
December 8, 2010

Certified by .....
Alexander Slocum
Pappalardo Professor of Mechanical Engineering
Thesis Supervisor

Accepted by.....
David E. Hardt
Professor of Mechanical Engineering
Chairman, ME Committee for Graduate Students

[Left Blank]

Heat Extraction for the CSPonD Thermal Storage Unit

by

Folkers Eduardo Rojas

Submitted to the Department of Mechanical Engineering
on December 8, 2010 in partial fulfillment of the requirements
for the degree of Master Science in Mechanical Engineering

Abstract

Three coiled tube heat exchanger prototypes were designed to extract heat from containers holding 0.5 kg, 2.3 kg, and 10.5 kg of Sodium Nitrate-Potassium Nitrate salt. All of the prototypes were left with an open surface free to undergo radiation losses and surface convection. The first objective was to measure the power extraction over time for each prototype. Coiled tube heat exchangers were modeled as a tube with a constant wall temperature. Air is used as the working fluid, with a maximum Reynolds number of 2000 at a maximum flow rate of 10 standard liters per minute (SLPM) at air flow temperatures above 90° C. The accuracy of the power extraction model for the three prototypes in increasing order: 46 %, 35 %, and 43 % of the measured data. The duration of power extraction with an open top container for the first (*P-I*), second (*P-II*), and third (*P-III*) prototype respectively are: 14 min, 29 min, 45 min producing an average power of 22 W, 23 W, and 22 W respectively. To compare across the prototypes, the data provided is for bath bulk temperatures starting at 330° C and ending at 275° C. Prototype three produced 25 W for 123 minutes for the same temperature change in the bulk temperature (330° to 275° C) with the lights off and a thermal lid, to reduce radiation and surface convection losses. The thermal lid improved the extraction duration by a factor of four. The second objective was to characterize the thermal loss rate (W) of the each prototype. The thermal loss rate model is accurate within 28.9 % (*P-I*), 28.7 % (*P-II*), and 24.7 % (*P-III*) of the measured values. There is evidence of convection cells in prototype two and three.

A high temperature Particle Image Velocimetry (PIV) system has been proposed to measure the magnitude of the convection cells, and a proof of concept setup has been tested. Particles native to the molten salt are illuminated using a Class 3b laser (power <5mW). The laser beam is converted into a plane using a polypropylene conical centrifuge tube filled with water.

Thesis Supervisor: Alexander Slocum

Title: Pappalardo Professor of Mechanical Engineering

Acknowledgements

While it has been an exhilarating experience, I am glad to be able to complete another project. First I would like to thank my family and friends. Madeline, thank you for the brainstorming sessions and companionship through out the process. Prof. Slocum, a special thanks to you, for the time and dedication to the intellectual growth process. After many revisions, we finally reached a final product. Thank you, PERG lab for the continual group support and look forward to working with you guys. I would also like to thank Pierce Hayward and Tom McKrell for letting me use their facilities to carry out the research.

The work could not have been done without the financial support of the Gates Millennium Scholarship program and the Cyprus.

Table of Contents

1. Introduction 11
   1.1. Motivation 11
   1.2. Prior Work 12
   1.3. Basic Heat Exchanger 13
   1.4. Basic Thermodynamics 13
2. Design Considerations 14
   2.1. Background 14
   2.2. Functional Requirements 18
   2.3. Container Structural Integrity 19
   2.4. Types & Methods for Solving HX 20
   2.5. Sizing Heat Exchangers 21
   2.6. Material Compatibility 21
3. Experimental Setup 22
   3.1. Integrated Unit 22
   3.2. Container Assembly 23
   3.3. Solar Simulator 23
   3.4. Configurations 24
   3.5. Penetration Depth on Insulation Section 25
   3.6. Instruments 26
   3.7. Materials 27
4. Heat Exchanger Model 29
   4.1. Steady State Losses 31
   4.2. Losses Over Time 33
   4.3. Calculated Heat Removal 34
5. 0.55 kg Coiled Tube Heat Exchanger 38
   5.1. Design 38
   5.2. Finite Element Analysis 43
   5.3. Preliminary Tests 43
   5.4. Data 45
   5.5. Results 48
   5.6. Lessons Learned 49
6. 2.20 kg Coiled Tube Heat Exchanger 50
   6.1. Design 50
   6.2. Finite Element Analysis 53
   6.3. Data 55
   6.4. Results 62
   6.5. Discussion 63
7. 10.5 kg Coiled Tube Heat Exchanger 66
   7.1. Design 66
   7.2. Data 71
   7.3. Results 74
8. Results 75
9. Conclusion 77
10. Future Work 77
11. Works Cited 78

List of Figures

Figure 1	CSPonD basic concept showing heliostat field reflecting solar energy into a molten salt reservoir.	11
Figure 2	Flat plate heat exchanger	13
Figure 3	Heat exchanger configurations: U-tube, and Straight tube	14
Figure 4	Procedure for prototype development, evaluation, and iteration.	18
Figure 5	Experimental setup: solar simulator, heat exchanger and pump assembly.	22
Figure 6	Container assembly layout	23
Figure 7	Solar simulator thermal images	24
Figure 8	Experimental configurations with Solar Simulator lights on	24
Figure 9	Experimental configurations with Solar Simulator lights off	25
Figure 10	Schematic representation of penetration depth	25
Figure 11	Basic coiled tube heat exchanger	29
Figure 12	Tubing wall temperature configuration	29
Figure 13	Volumetric heat capacity comparison between molten salt and air flow	30
Figure 14	Schematic diagram of container assembly showing steady state losses	31
Figure 15	Surface convection losses schematic diagram	32
Figure 16	Control volume for internal flow in a tube	34
Figure 17	Plot of output flow temperature as function of tubing length	36
Figure 18	Heat removal calculation flow chart	37
Figure 19	First prototype coiled tube heat exchanger	38
Figure 20	Coiled tube heat exchanger cross section view	39
Figure 21	Cross section diagram of *P-I*	39
Figure 22	Reynolds number versus exit air flow temperature for a 10 SLPM flow rate	41
Figure 23	Radial heat loss FEA model	43
Figure 24	Salt melting process	44
Figure 25	Melting process with copper inserts	44
Figure 26	T-junction air flow measurement comparisons	45
Figure 27	*P-I* energy harvesting with lights on	46
Figure 28	*P-I* energy harvesting with lights off	47

Figure 29	*P-I* Heat loss comparison between theory and data	47
Figure 30	FEA radial temperature gradient compared against collected data	48
Figure 31	Second prototype container and heat exchanger	50
Figure 32	Second prototype cross section view	51
Figure 33	Second prototype dimensions and materials	54
Figure 34	FEA radial temperature gradient for the second prototype	54
Figure 35	Radial temperature gradient measurements for the second prototype	55
Figure 36	Top view of prototype two with the insulation region covered	56
Figure 37	Insulation temperature gradient under different configurations	56
Figure 38	Energy extracted from prototype two: average and instantaneous	57
Figure 39	Molten salt temperature gradient as a function of depth	57
Figure 40	Thermal image of surrounding insulation temperature	58
Figure 41	Thermal image of flow measurements	59
Figure 42	P-II Bulk temperature as a function of time	59
Figure 43	P-II compare between theoretical and calculated bulk temperature over time	60
Figure 44	Heat Loss comparison between data and thermodynamic model	60
Figure 45	Darkened stainless steel vessel after usage and insulation degradation	62
Figure 46	Particle Image Velocimetry (PIV) schematic layout	64
Figure 47	PIV proof of concept images	65
Figure 48	*P-III* heat exchanger setup	66
Figure 49	*P-III* temperature measurement layout	67
Figure 50	*P-III* schematic layout of materials	67
Figure 51	Radial and depth temperature measurements inside molten salt bath	71
Figure 52	*P-III* Energy harvesting of with capped and open configuration	72
Figure 53	P-III bulk temperature comparison between data and theory	73
Figure 54	P-III Heat Loss model to data comparison	73
Figure 56	Effectiveness as a function of flow rate (SLPM) for the three prototypes	75
Figure 57	Time to reach 90% steady state versus mass for all three prototypes	76

List of Tables

Table 1	Prototype functional requirements	18
Table 2	Penetration depth calculation	26
Table 3	Hitec solar salt properties	28
Table 4	*P-I* thermal losses	40
Table 5	Internal flow inside a tube convection coefficient	41
Table 6	*P-I* heat removal	42
Table 7	*P-II* thermal losses	52
Table 8	*P-II* heat removal	53
Table 9	Heat loss calculation for exposed tubing length in *P-II*	58
Table 10	*P-II* molten salt convection	61
Table 11	*P-III* thermal losses open surface configuration	68
Table 12	*P-III* heat removal	69
Table 13	*P-III* Capped radiation and convection losses	70
Table 14	Prototype results summary table	75

List of Variables

Variable	Unit	Description
A	m^2	Cross sectional area
A_T	m^2	Cross sectional area of Open Container Surface
C_c	J/(kg*K)	Cold Fluid Heat Capacity
C_h	J/(kg*K)	Hot Fluid Heat Capacity
C_{max}	J/(kg*K)	Maximum heat capacity between Hx Cold Fluid and Hx Hot Fluid
C_{min}	J/(kg*K)	Minimum heat capacity between Hx Cold Fluid and Hx Hot Fluid
C_p	J/(kg*K)	Heat Capacity
C_r	-	Ratio of the heat capacities
d	m	Flow tubing diameter
D	m	Diameter
f	-	Darcy Friction Factor
f_{LAM}	-	Laminar Darcy friction factor
f_{TURB}	-	Turbulent Darcy friction factor
g	m/s^2	Gravity
Gr	-	Grashoff number
h	$W/(m^2*K)$	Convection Coefficient
h_{ext}	$W/(m^2*K)$	External convection outside of insulation
h_{surf}	$W/(m^2*K)$	Top surface convection coefficient
h_{bottom}	$W/(m^2*K)$	Convection coefficient
H	m	Height of Container
k	W/(m*K)	Thermal Conductivity
k_{case}	W/(m*K)	thermal conductivity of the case
k_f	W/(m*K)	Thermal Conductivity of the fluid
$k_{insulation}$	W/(m*K)	Thermal conductivity of the insulation
k_{tube}	W/(m*K)	Thermal conductivity of tubing
l	m	Tubing Length
l_c	m	critical length used for the finding the Rayleigh number
Nu	-	Nusselt Number
Pr	-	Prandtl Number
q	J	Heat transfer
Q'_P	W	Power Extraction
$Q'_{Radiation}$	W	Molten salt top surface radiation loss rate
Q'_{Radial}	W	Radial heat loss rate
Q'_{Surf}	W	Molten salt top surface convection loss rate
R_{tot}	K/J	Total Thermal Resistance
Ra	-	Rayleigh number
Re	-	Reynold's Number
S	J/K	Entropy
S_{gen}	J/K	Generated Entropy
t	sec	time
t	m	Thickness
t_{case}	m	Thickness of the case
$t_{insulation}$	m	Thickness of insulation
T	K	Temperature
$T_{c,i}$ $T_{Cold\ Side,In}$	K	Temperature of cold flow entering the heat exchanger
$T_{c,o}$ $T_{Cold\ Side\ Out}$	K	Temperature of cold flow exiting the heat exchanger
$T_{h,i}$ $T_{Hot\ Side\ In}$	K	Temperature of hot flow entering the heat exchanger

$T_{h,o}$ $T_{Hot\ Side\ Out}$	K	Temperature of hot flow exiting the heat exchanger
T_{room}	K	Room temperature
T_{salt}	K	Bulk temperature of the salt
UA	J/K	Heat Transfer Coefficient
V	m/s	Average Velocity
W	N*m	Work
α	m^2/sec	Thermal diffusivity
β	K^{-1}	thermal expansion coefficient
γ	-	view factor
ΔT_{LM}	K	Log mean temperature difference
ΔT_{out}	K	Exit temperature difference
ΔT_{in}	K	Inlet temperature difference
ΔS	J/K	Change in Entropy
ΔU	N*m	Change in Energy
ε	-	Emissivity
ε_{Hx}	-	Hx Effectiveness
ε_r	m	Tubing roughness coefficient
ζ	m	Exit temperature misalignment from center line
μ	kg/(m*sec)	Dynamic Viscosity
ν	m^2/sec	Kinematic viscosity
ρ	kg/m^3	Density
σ	$J/(K^4m^2s)$	Stefan-Boltzmann Const

1.Introduction

As world energy consumption increases, companies and governments alike are looking for renewable forms of energy. However, the problem with most green energy sources, like solar and wind, is that they are cyclical or sporadic. While predictions of energy availability are accurate, currently (other than pumped hydro-system) there is no widely accepted means by which to store large amounts of solar energy over a twenty-four hour period. Concentrated Solar Power on Demand (CSPonD) is a project at MIT, led by Prof. Alex Slocum, whose aim is to receive and store solar energy in the form of a molten salt bath. The molten salt bath can be heated by concentrated solar energy during the day using a heliostat array on the side of a mountain. Part of the goal is to provide continuous 24/7 power output from the high temperature salt bath. CSPonD can serve as a means to address the growing demand for greener energy sources [Slocum, et al].

The objective of this thesis is to develop an accurate thermodynamic model for removing heat from the CSPonD bath to produce electric power. The thermodynamic model created will require validation with experimental data. Once validated, the model will serve as a tool to calculate the effect of changing materials, geometry, fluid properties, etc. on alternative heat exchanger designs and heat transfer for large scale energy storage device.

1.1. Motivation

CSPonD is a multidisciplinary project investigating the entire systems operation of harvesting solar energy, storing it in a molten salt bath, and generating electricity at a later time. During the day the tank would function as a thermal capacitor (storing solar energy). In the evening, the thermal capacitor would be discharged to generate electric power. The molten salt bath is analogous to an electric capacitor. The group is looking at developing tools and bench level prototypes for proving the principal concepts and parameters to successfully design a megawatt size unit. The big picture consists of reflecting solar energy directly into a reservoir of molten salt, as shown in **Figure 1**. Individual projects are exploring each phase of system: 1) heliostat placement [Corey, et al], 2) heliostat cleaning [Figueredo], 3) volumetric salt receiver [Codd, et al], 4) power cycle, 5) optical attenuation characteristics [Passerini], 6) optical heating [Codd, et al], and 7) energy extraction (subject of this thesis).

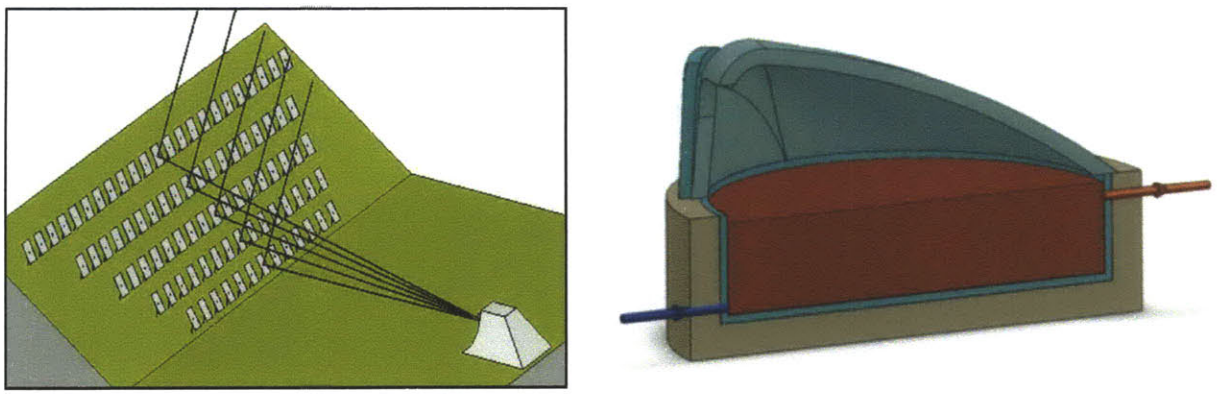

Figure 1: CSPonD basic concept showing a heliostat field reflecting solar energy into a reservoir. The reservoir (shown on the right) is a prototype design for a 4 MWe CSPonD system using 2500 m^3 of salt for a period of 40 hour storage (*figures courtesy Slocum, et al.*).

The focus of this thesis is the energy extraction from the molten salt reservoir. The heat extraction loop can vary greatly depending on the size of the unit and the operating temperature of the salt. Another source of variability is the composition of the salt along the temperature range 250-1000°C. For example, a kilowatt unit using salt temperature in the 300-500° C range (Nitrate salts) can use off the shelf components for pumps, piping, etc that can make up the heat extraction loop. Once the operating temperatures go above 660°C (Chloride salts), and the power rating is increased, the components have to be custom made and become more costly.

There are several ways to remove heat from the molten salt. One option is to use the molten salt as a working fluid. Another option is to use a solid metal interface to conduct heat out of the molten bath and transfer it into an intermediate working fluid. A third option is to use an intermediate working fluid to remove heat from the molten bath. The heat removal process will greatly depend on the functional requirements of the unit.

1.2. Prior Work

As stated by Green in 1976: *The steps required in the design of a thermal energy storage system include storage concept definition, storage material selection and characterization, and specification of methods of transferring heat to and from the storage unit* [Green]. While advances have been made in the field of materials, the basic concepts and topics proposed by Green are still as valid today as they were back then.

Several molten salt thermal storage designs have been developed and a few have been implemented in large scale. For example, Solar Two is a 10 MW electric prototype in the Californian Mojave Desert with a two-tank storage system. The basic operation of Solar Two consists of a system that bounces light from the heliostat field to the receiver tower, which heats salt pumped from the cold storage tank, and flows the hot salt into the hot salt storage tank. As discussed by Epstein there are several complications with the existing setup such as: 1) salt freezing in the loop, and 2) complicated start-up process.

A great deal of work has also been done in the field of thermal storage medium. The nitrate salts used in Solar Two plant are almost transparent to the solar spectrum, and the bottom of the tank can be used to absorb the solar heat and transmit it to the salt via natural convection or forced convection [Epstein]. The salt used in the Solar Two prototype is a mixture of 60% $NaNO_3$ and 40% KNO_3.

A complete integrated and operational design solar power plant has already been commercialized by Abengoa and is providing electricity for the grid. Located in southern Spain, PS10 is a 11 MW solar thermal tower plant, one of the first solar power tower to commercially generate electricity and deliver it to grid. Solar energy is reflected of an array of heliostats and focused onto a central receiver that generates saturated steam used for generating electricity [Afloresm]. There are plans to have PS20 with twice the capacity of PS10. The solar field for PS20 consists of 1255 heliostats and a 524 ft high tower. However, the PS10 unit lacks significant storage capability.

Another commercialized unit is Andasol-1 and 2 with a gross electric output of 50 MWe. This is also a tower based system similar to Solar Two. The storage system of the plants can provide up to 7.5 hours of electric power after sunset. The molten salt mixture used is also a 60/40 sodium nitrate-potassium nitrate mixture. The thermal storage is a dual tank indirect system. Each tank measures 36 meter in diameter with a depth of 14 meters. The total amount of salt is 28.5 kilotons which stores 1010 MWh [Andasol I].

While there are a plethora of designs, there are many complexities and unresolved intricacies with most of the current designs. For example, the work done by Epstein in 1999

using Solar Two can be improved by consolidating the dual tank design has proposed by Wang et al in 1985. The single tank approach using natural or "rafted" thermoclines is less expensive, and is a topic of current CSPonD research at MIT. Changing to a working fluid that does not freeze in the tubing is also an area for further improvement: One option for CSPonD to not have any salt filled tubes as the sunlight directly illuminates the salt in a single tank. While advances have been made in the existing technology, there are still many challenges that remain to be addressed.

1.3. Basic Heat Exchanger

The heat removal from the CSPonD bath can be accomplished by means of a heat exchanger. The main purpose of heat exchangers is to transfer energy in the form of heat between two bodies i.e. a flowing medium and a solid boundary or two separated fluid streams.[1] An automotive engine, for example, generates large quantities of heat. The heat is removed through the radiator, which can consist of a flat plate heat exchanger, exchanging two fluid streams. One fluid stream consists of coolant fluid inside the radiator. The second fluid is air flowing through the radiator. **Figure 2** shows a flat plate heat exchanger used in the automotive industry with the inlet and outlet ports for the coolant and the flat plate array where cold air crosses to cool the coolant strea

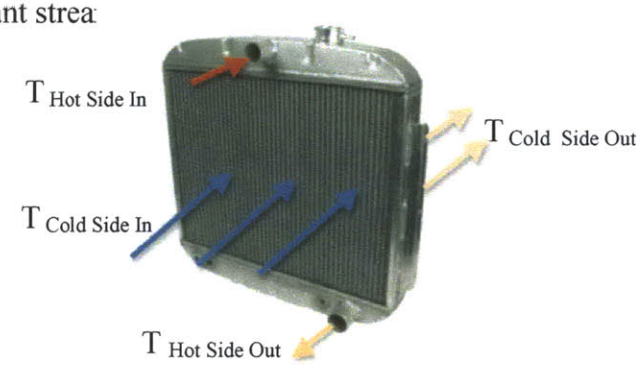

Figure 2: Flat plate heat exchanger used in the automotive industry. [2] The hot side consists of engine coolant while cold side is air flow. The hot fluid enters the flat plate heat exchanger hot and is cooled such that $T_{Hot\ Side\ In} > T_{Hot\ Side\ Out}$ and $T_{Cold\ Side\ Out} > T_{Cold\ Side\ In}$.

1.4. Basic Thermodynamics

The basic principles of thermodynamics dictate that heat flows from hot to cold, systems always try to reach the lowest energy state, and there is always a cost (entropy/chaos) for any change to the system.

The first law of thermodynamics is conservation of energy. Energy going into a system can either go into heating the system, reflected by the system, or altering the system permanently. For example, when melting a plastic cup with a hair dryer, some of the heat is absorbed, some goes to melt, and most of it is directed to the environment. The energy absorbed by the cup can go into heating the temperature of the cup (reversible), and permanently changing the structure of the cup (irreversible). By adding the energy required for the reversible process and irreversible process the total energy absorbed by the cup can be determined.

---

[1] MIT 2.006 Course Notes (Spring 2008) by Cravalho (Chp 12 Pg. 1)

[2] For more detailed explanation of heat exchangers refer to chapter 8 in Fundamentals of Heat and Mass Transfer by Incropera et al. Image from online: electric-radiator.net

The second law of thermodynamics describes entropy generation and it says that the change in entropy from state 1 to state 2 is equal to the transferred entropy plus the entropy generated. Heat exchangers must abide by the laws of thermodynamics. The mathematical representation and the analytical equations are covered in more depth in Section 4.3.

2. Design Considerations

The following are considerations for designing a heat extraction loop from the CSPonD molten bath. This chapter covers the following topics: 1) heat exchanger background, 2) functional requirements, 3) container structural integrity, 4) types of heat exchangers, 5) sizing heat exchangers, 6) material compatibility, and 7) list of thermodynamic correlations.

2.1. Background

There exists a plethora of heat exchanger configurations, each with its specific characteristics, applications, and functional range. Types of heat exchangers include: concentric parallel flow, concentric counter flow, shell and tube, plate, etc. **Figure 3** shows some of the configurations and types of heat exchangers.

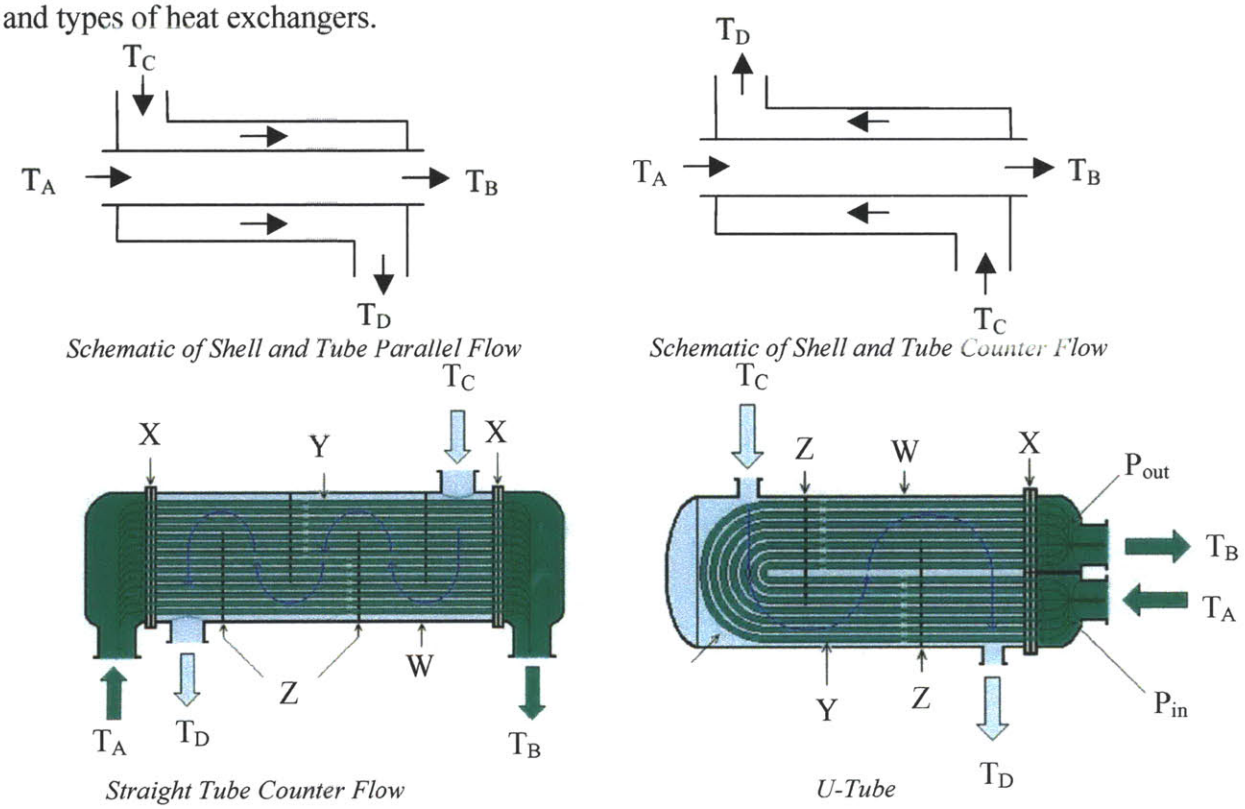

Figure 3: The top images show a shell and tube parallel flow and counter flow. $T_A = T_{cold\ in}$, $T_B = T_{cold\ out}$, $T_C = T_{hot\ in}$, $T_D = T_{hot\ out}$, W = shell, X= tube sheet, Y = tube bundle, Z = baffles, P_{in} = inlet plenum, P_{out} = outlet plenum. The bottom images show both a U-tube and a straight tube heat exchanger.[3]

Prior to beginning a heat exchanger design it is necessary to become accustomed to the language of heat exchangers and the components/calculations that are required to size a heat

[3] The images by Lamar Stonecypher (May 21, 2010). Article written published by Lamar Stonecypher (May 21st 2010). Location: http://www.brighthub.com/engineering/mechanical/articles/59713.aspx

exchanger. Many of the terms that are required to size a heat exchanger are in non-dimensional form. The following section covers an overview of non-dimensional parameters that are normally used when designing a heat exchanger. Designing heat exchangers is an art form that requires an understanding of thermodynamics, mathematics, manufacturing capabilities, and material properties. The following background section on heat exchangers covers the basic nomenclature/language of heat exchangers.

2.1.1. First Law

The first law of thermodynamics is the conservation of energy, as shown in Equation 1. The change in internal energy, ΔU [J], is equal to the heat added, Q [J] to the system minus the work done by the system, W [J].

$$\Delta U = Q - W \qquad \text{Equation 1}$$

2.1.2. Second Law

The second law of thermodynamics governs entropy generation, as shown in Equation 2[4].

$$S_2 - S_1 = \sum_i \left(\frac{Q}{T}\right)_i + S_{gen} \qquad \text{Equation 2}$$

Where T_i [K] is the temperature at the point where the heat transfer Q_i [J] is taking place, and S_{gen} [J/K] is the generated entropy by the process. The process is reversible when S_{gen} is zero, and irreversible when S_{gen} is greater than zero. For example if an isolated adiabatic system undergoes changes in state ($S_2 \neq S_1$) then the change in entropy is in S_{gen}, which makes the process irreversible.

2.1.3. Reynolds Number

The Reynolds number is a non-dimensional parameter that is defined as the ratio between inertial forces and viscous forces, as shown in Equation 3 for circular tubing.[5]

$$\mathrm{Re} = \frac{\rho \cdot V \cdot d}{\mu} \qquad \text{Equation 3}$$

$$\mathrm{Re} = \frac{4 \cdot \dot{m}}{\pi \cdot \mu \cdot d}$$

Where ρ [kg/m^3] is the density, V [m/s] is the average velocity of the medium, d [m] is the interior diameter of the tubing, and μ [kg/(m*s)] is the dynamic viscosity of the flowing fluid.

The transition between laminar and turbulent flow conditions inside a pipe occurs at Reynolds values around 2300. Under laminar conditions the heat transfer can be significantly smaller compared to turbulent conditions. Turbulent flow parameters allow for mixing which decreases temperature stratification in a flow thus increases amount of heat that can be removed by a working fluid. For the heat exchanger design process the Reynolds number represents properties of the working fluid and geometric parameters (i.e. diameter of pipe).

---

[4] MIT 2.005 Course Notes (Spring 2006) by Cravalho et al (Chp 8 pg 24)
[5] MIT 2.006 Course Notes (Spring 2008) by Cravalho (Chp 10 pg 48)

2.1.4. Prandtl Number

The Prandtl number is a non-dimensional parameter that is defined as the ratio between the momentum diffusivity and thermal diffusivity, as shown in Equation 4. The Prandtl number will be used in heat exchanger correlations for determining dominant convection coefficient forced/natural.

$$\mathrm{Pr} = \frac{\mu \cdot C_p}{k_f} \qquad \text{Equation 4}$$

Where C_p [J/ (kg*K] is the heat capacity of the medium, and k_f [W/(m*K)] is the thermal conductivity of the fluid, and μ [kg/(m*s)] is the dynamic viscosity of the fluid. A Prandtl number is much less than one then the temperature profile develops much faster than the velocity profile in a tube, the opposite applies for Prandtl greater than one.

2.1.5. Thermal Diffusivity

Thermal diffusivity (α), Equation 5, is a ratio that expresses how quickly a material can transfer rather than store heat.

$$\alpha = \frac{k}{\rho \cdot C_p} \qquad \text{Equation 5}$$

Where k is the thermal conductivity of the material, ρ is the density and C_p is the heat capacity.

2.1.6. Darcy Friction Factor

The Darcy friction factor is used to calculate the pressure drop across a pipe section given geometric and flow parameters. The Darcy friction factor correlation for laminar and turbulent flow are shown in Equation 6 and Equation 7, respectively. The correlations will be important to calculate the required pressure drop across a circular coiled tube heat exchanger and for the heat exchanger performance calculations.

$$f_{LAM} = \frac{64}{\mathrm{Re}} \qquad \text{Equation 6}$$

$$f_{TURB} = \frac{1.325}{\left[\ln\left(\frac{\varepsilon_r}{3.7 \cdot d}\right) + \frac{5.74}{\mathrm{Re}^{0.9}}\right]^2} \qquad \text{Equation 7}$$

Where f [unitless] is the darcy friction factor, ε_r [unitless] is the roughness of the tube, and d [m] is the interior diameter of the tube.

2.1.7. Nusselt Number

The Nusselt number is the ratio between convection and conduction, as shown in Equation 8. Low Nusselt numbers imply that conduction is the primary form of heat transfer. High Nusselt number are indicative of systems where convection is the dominant form of heat transfer.

$$Nu_D \equiv \frac{h \cdot D}{k_f} \qquad \text{Equation 8}$$

Where h [W/(m^2*K)]] is convection coefficient, k_f [W/(m*K)] is the conduction coefficient, and D [m] is the characteristic length. In the case of a tube it is the interior wall diameter in contact with the fluid.

2.1.8. Effectiveness

Effectiveness (ε), Equation 9, is defined as the ratio of the actual heat transfer rate to the maximum ideal heat transfer rate. The actual heat transfer rate is C_{cold} multiplied by the change in temperature of the cold side. The maximum heat transfer rate is the minimum heat capacity, C_{min}, between the hot and cold side multiplied by the maximum temperature gradient in the heat exchanger. The effectiveness works as a quality factor for characterizing a heat exchanger type or configuration.

$$\varepsilon = \frac{C_c \cdot (T_{c,o} - T_{c,i})}{C_{\min} \cdot (T_{h,i} - T_{c,i})} \qquad \text{Equation 9}$$

Where C [J/kg*K] is the heat capacity, and T [K] is the temperature. The lower scripts denote the following: c = cold side, i = inlet, h = hot side, and o = outlet.

2.1.9. NTU

The *number of heat transfer units* (NTU) is a non-dimensional parameter used to characterize/analyze heat exchanger performance, defined in Equation 10.

$$NTU = \frac{UA}{C_{\min}} \qquad \text{Equation 10}$$

Where C_{min} is the minimum heat capacity of the working fluid. The overall heat transfer coefficient, UA, is defined as the inverse of the total resistance, as shown in Equation 11.

$$UA = \left(\sum R_{tot}\right)^{-1} \qquad \text{Equation 11}$$

Where R_{tot} is the total thermal resistance. R_{tot} is the sum of the different thermal resistant layers between two set points. For the experimental setup the two boundary conditions are at the wall of the container and at the outer surface of the insulation. The experimental calculations are covered in more detailed for each prototype.

2.1.10. Rayleigh Number

The Rayleigh number, Ra, is used to characterize natural convection, it is the multiplication of the Grashof and the Prandtl number, as shown in Equation 12. The Grashof number is the multiplication of the buoyant forces and inertial forces divided by the viscous forces squared.

$$Ra = Gr \cdot \Pr = \left(\frac{\beta \cdot (\Delta T) \cdot g \cdot l_c^3}{v^2}\right) \cdot \left(\frac{v}{\alpha}\right) \qquad \text{Equation 12}$$

Where β [1/K] is the thermal expansion coefficient, g [m/s^2] is the acceleration due to gravity, v [m^2/sec] is the kinematic viscosity, and l_c [m] is the characteristic length.

The Rayleigh number will be used to calculate the heat loss due to natural convection at the surface of the molten salt bath.

2.2. Functional Requirements

The functional requirements of each CSPonD heat exchanger design will vary with the size of the unit. There will be several iterations to be developed and tested on the way to a large megawatt unit. The first prototype should hold the volume of a coffee cup, and be capable of extracting 40 W of thermal power. The second prototype should be between five and ten times the size of the first prototype, and heat extraction on the order of 40 W. The third prototype should once again be between five and ten times the size of the second prototype, and heat extraction on the order of 40 W. The duration of extraction is expected to increase with each prototype. Each prototype will undergo the procedure shown in **Figure 4** to evaluate system performance and comparison.

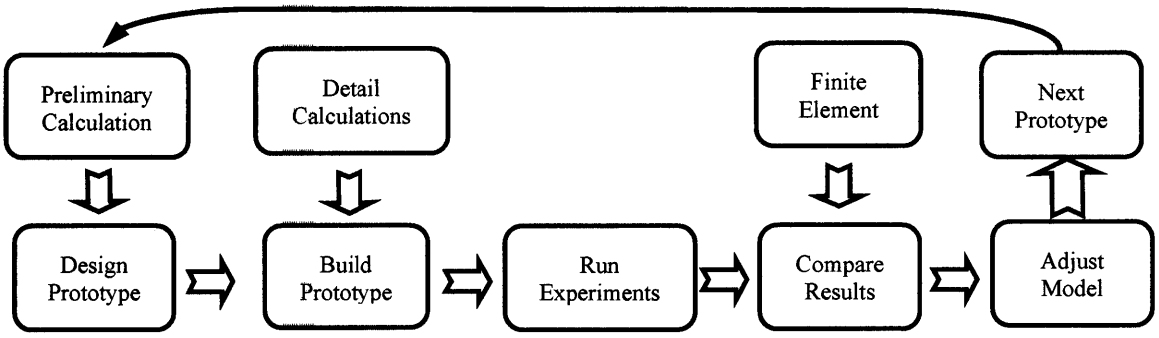

Figure 4: Procedure for prototype development, evaluation, and iteration.

All of the prototypes are designed with manufacturing considerations. **Table 1** shows an overview of the functional requirements for each prototype.

Table 1: Prototype functional requirements.

	Objective	Functional Requirements
Prototype I (*P-I*) $m_{salt} \approx 0.5$ kg	Heating with solar simulator	Nitrate Salt compatibility
	Verify heat removal proof of concept.	Withstand temperatures 400° C
	Radial measurements to compare against model	Hold 0.5 kg of molten salt
	Determine heat removal calculations	
Prototype II (*P-II*) $m_{salt} \approx 2.0$ kg	Heating with solar simulator	
	Increase thermal mass	
	S.S. temperature gradient inside salt	Nitrate Salt compatibility
	S.S. insulation temperature measurements	Withstand temperatures 400° C
	Heat removal time longevity	Hold 2.0 kg of molten salt
	Convection in the salt	
Prototype III (*P-III*) $m_{salt} \approx 10.0$ kg	Heating with solar simulator	Nitrate Salt compatibility
	Radial temperature measurements	Withstand temperatures 400° C
	S.S. salt temperature gradient	Hold 10.0 kg of molten salt
	Heat removal time longevity	
	Convection in salt	

2.3. Container Structural Integrity

There are many possible geometric considerations for holding the molten salt bath. The final geometry of the storage tank takes into account manufacturing considerations as well as ease of thermodynamic modeling geometries.

2.3.1. Casing Shape

Two identified ways for holding the required volume of the molten bath are cubical or cylindrical structures, and section is based on manufacturing complexity, thermodynamic modeling, and structural integrity. Although both shapes are about the same difficulty in manufacturing, the cylindrical structure is often readily available as an off the shelf item, while the cubical shape involves a more of manufacturing complexity. The advantage of using a cylinder over a cube is the ease thermodynamic modeling and manufacturing.

For the cube, the thermodynamic model can vary on the orientation of the structure. A twist or a tilt in the geometry of the structure can lead to a different thermodynamic configuration. The cube also has regions (i.e. corner edges) where the salt losses more heat. For the cylinder, the thermodynamic models can vary significantly with a tilt but not with rotation. While the cylindrical geometry is slightly more complex for a model based on particle interactions, an axisymmetric model can reduce the complexity.

From the structural integrity perspective the preferred shape would be the cylinder. Depending on how the cube is manufactured it may be prone to leaks, and weak points. Therefore, the shape of the casing should be a cylinder, based on manufacturing and structural integrity, which outweigh the alterations of the thermodynamic models based on orientation.

2.3.2. Holding Vessel & Insulation

A critical functional parameter is the insulation of the molten bath. There are several ways of insulating effectively; however one of the most efficient methods is employed in the home refrigeration industry. The insulation of a refrigerator is a three layer composite. The first layer is the plastic in the inside of the fridge. Surrounding the plastic is about an inch of insulation material with high thermal resistance coefficient. The third layer is casing which provides structural integrity.

Admittedly, the insulation section appears simple at a glance; however, that is not the case. The molten bath in a high temperature megawatt (MW) unit is expected in the order of 700 to 1000° C. Therefore, the interior sleeve containing the molten bath must be able to withstand the high temperatures. A high temperature insulation layer surrounding the interior sleeve should be used to reduce the amount of radial heat loss. Using salts to store energy also benefits the insulation system. As the salt solidifies at the perimeter of the container, it has a very low thermal conductivity further reducing the heat losses. Also in the case of catastrophic breach of the container the salt solidifies preventing a larger spill.

2.4. Types & Methods for Solving HX

As mentioned in Section 2.1, there exists a plethora of heat exchanger types and flow configurations. Two common ways of solving heat exchanger dynamics are: 1) finite element analysis (FEA), and 2) Effectiveness-Number heat Transfer Units (NTU) better known by its acronym (ε-NTU). A third method for modeling Hx performance is by using fittings to collected data in the form of correlations. A fourth method is the Log Mean Temperature Difference (LMTD), which is simple given the fluid inlet and outlet temperatures. However, if only the inlet temperatures are known then the LMTD method requires an iterative process.

One of the most popular approach, ε-NTU, relates the effectiveness (ε) to the number of heat transfer units (NTU). The primary tool for solving heat exchanger problems with ε-NTU is a series of relations that relate ε to NTU and vice versa (also includes fluid properties). The relations are in terms of non-dimensional parameters such as effectiveness, heat capacity ratio, and NTU's. For example, provided an NTU value the effectiveness can be found certain geometries using tabular relations. The relation for concentric tube parallel flow is given in **Figure 12**.

$$\varepsilon = \frac{1 - \exp[-NTU \cdot (1 - C_r)]}{1 - C_r} \qquad \text{Equation 13}$$

Where C_r is heat capacity ratio $C_r = C_{min}/C_{max}$. The effectiveness can be related to Equation 9 to find the exit temperatures. An entire list of relations for frequently used flow arrangements can be found in Incropera et al[6]

There are several FEA packages that can be used to model the detailed thermodynamics of a heat exchanger design (ANSYS, ADINA, etc.) There is a plethora of proprietary codes for modeling specific heat exchanger geometries that are used in the industry. Pro-Engineer and Solidworks have also developed flow packages that have the capabilities for modeling heat exchangers. One of the challenges of using FEA packages is verification. An FEA model must be verified with simple geometries to verify the fundamental behavior prior to modeling a complex system.

For given geometries/models, correlations can be used to characterize the performance of a Hx design. For example, there are correlations for laminar flow between parallel plates with fully developed hydrodynamics that can be used as an approximation for a heat exchanger model, or turbulent flow in smooth ducts, etc. There is a plethora of correlations that are available with given sets of boundary conditions.[7] It is customary to have the correlations with respect to non-dimensional parameters such as *Nu, Pr, Re*, etc. The challenge of using correlations is finding the correlation that can best capture the thermodynamics of the new Hx design.

The LMTD method uses a weighted average temperature ΔT_{LM} defined by Equation 14, with the heat transfer rate, Q' [W], calculated by Equation 15. The main challenge of using the LMTD method is the continuous iteration when the inlet or outlet temperatures are not fully defined.

$$\Delta T_{LM} = \frac{\Delta T_{out} - \Delta T_{in}}{Ln\left(\frac{\Delta T_{out}}{\Delta T_{in}}\right)} \qquad \text{Equation 14}$$

[6] Heat and Mass Transfer (5th Ed) by Incropera, DeWitt Chp 11, Pg 662
[7] MIT 2.006 Course Notes (Spring 2008) by E. Cravalho Chp 11, Pg 58

Where the ΔT_{out} is the difference of the exit temperatures and ΔT_{in} is the difference of the entry temperatures.

$$Q^{'} = UA \cdot \Delta T_{LM} \qquad \text{Equation 15}$$

Heat exchanger performance ultimately has to be measured and the thermodynamic model validated or corrected for future use in scaling the designs.

2.5. Sizing Heat Exchangers

The design process for sizing a heat exchanger usually begins with the power transfer specifications for a unit. Since the objective of the project is to study the behavior of both the heat exchanger and the bath, it is not recommended to have a heat exchanger that can remove the heat at an extreme speed. The desired heat exchanger is a slow consistent removal that can be used to characterize the energy extraction from the pond with a given configuration. The objective of a megawatt size unit is to provide continuous removal for a 24/7 period.

2.6. Material Compatibility

Molten salt mixtures can be corrosive to certain materials. In some circumstances the salts can become corrosive only above a certain temperature. For example, *nitrate salts can not exceed temperatures higher than 600° C as it reaches chemical instability and becomes corrosive* [Epstein].

Coastal Chemical Co., the manufacture of Hitec Solar salts lists some material compatibilities in their brochure [Coastal Brochure]. Bronze, phosphorous, and Hastelloy have a corrosion rate in the order of several micro inches per month, which over time can lead significant corrosion to the casing. For example an interior stainless steel casing (304L) with a 2.54 cm (1 inch) wall thickness will last less than 14 years before it is completely corroded at operational temperatures in the range of 550° C. Open hearth steels (ASTM A273, A274), operating at temperature around 590° C can last anywhere between 1.7 (0.05 in/month) to 8.3 (0.01 in/month) years with a 2.54 cm (1 inch) casing. The same hearth steels have corrosion destruction in the order of 30 micro inches per month at temperatures ~450° C. The corrosion rate increases with temperature. For a more complete list of the materials see *Table II Corrosion of metals by Hitec* in the Hitec Solar Salt brochure provided by *Coastal Chemical Company.*

3. Experimental Setup

The experimental setup consists of the physical setup and the data instrumentation, used to tests the three prototypes. The physical setup consists of the solar simulator, container assembly, and pump assembly. The instrumentation section covers materials properties and temperature measurement devices.

3.1. Integrated Unit

The complete system consists of the solar simulator [Codd et al], container assembly, and pump assembly, shown in **Figure 5**. The solar simulator concentrates light from seven metal halide lamps (1.5 kW each) to the container assembly filled with nitrate salt. Over time the salt in the container reaches its melting point and gradually melts. Energy can be removed from the molten salt by pumping air through a coiled tube heat exchanger, which is part of the container assembly. The pump assembly consists of an air pump with a flow meter to measure the air flow rate used to extract heat from the salt container.

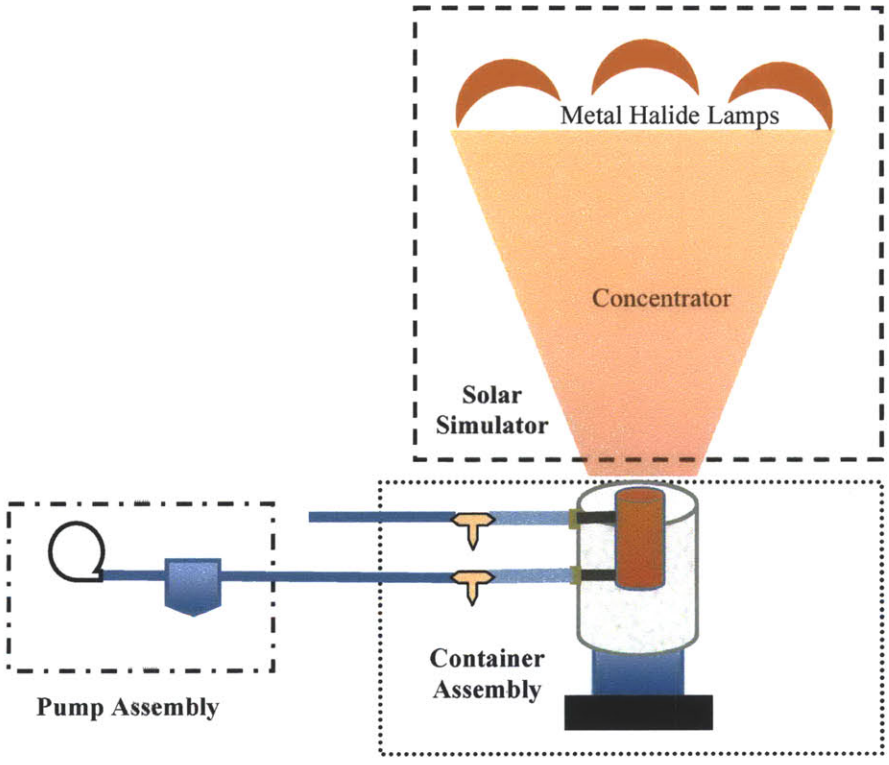

Figure 5: System setup showing solar concentrator, heat exchanger assembly, pump assembly. The solar concentrator is composed of seven metal halide (MH) lamps (1500 W each). The heat exchanger assembly houses the salt container/heat exchanger unit, insulation, piping, etc. The pump assembly consists of an air compressor and tank equipped with a flow meter. The current flow meter is rated between zero and ten liters per minute.

3.2. Container Assembly

The container assembly consists of the salt container, heat exchanger, and insulation. The detailed layout of each prototype can be found in each prototype section. **Figure 6** shows the experimental setup of a generic container assembly. For the purpose of testing the heat exchangers the salt inside the salt container is melted using the solar simulator. The steady state molten salt temperature is a function of the type and amount of insulation in the radial direction and below the container and the radiation losses to the environment.

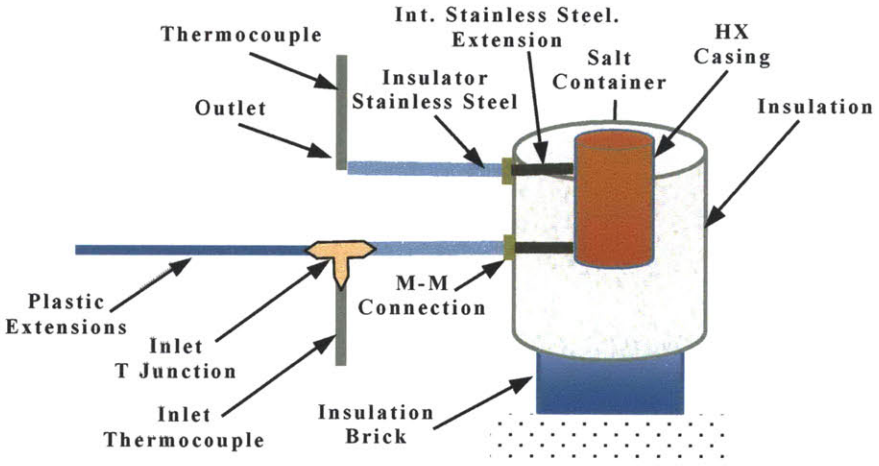

Figure 6: Experimental setup of the container assembly showing the HX casing, insulation surrounding the heat exchanger, piping, location of the thermocouples that measure flow temperatures. The container assembly is used in conjunction with the solar concentrator, air pump, and electronic readouts. The direction of the setup shown is from bottom to top. The k-thermocouple is not in direct contact with the flow tube.

The interior stainless steel extension serves to reduce the temperature that is conducted to the environment. An additional insulation region (stainless steel tube) was added to isolate the effects of the thermal concentrator from interfering with the flow temperature measurements. For the entry air temperature measurements T-junctions can be used to hold the k-thermocouple for measuring the temperature of the passing air. The hot air temperature is measured by placing a k-thermocouple in the exiting stream.

3.3. Solar Simulator

The solar simulator is an essential part of the experiment, as it is used instead of a heliostat reflector field. The solar simulator used through out the experiments is a custom low budget solar simulator [Codd et al]. The simulator as an output flux greater that 50 kW/m^2, generated across an output aperture of 38 cm using an array of seven metal halide lights in combination with concentrating optics. **Figure 7** shows the solar simulator setup and two thermo images that show the steady state temperatures of the concentrator unit. The initial radiation losses are calculated using the environmental temperatures obtained from the thermal images of the solar simulator.

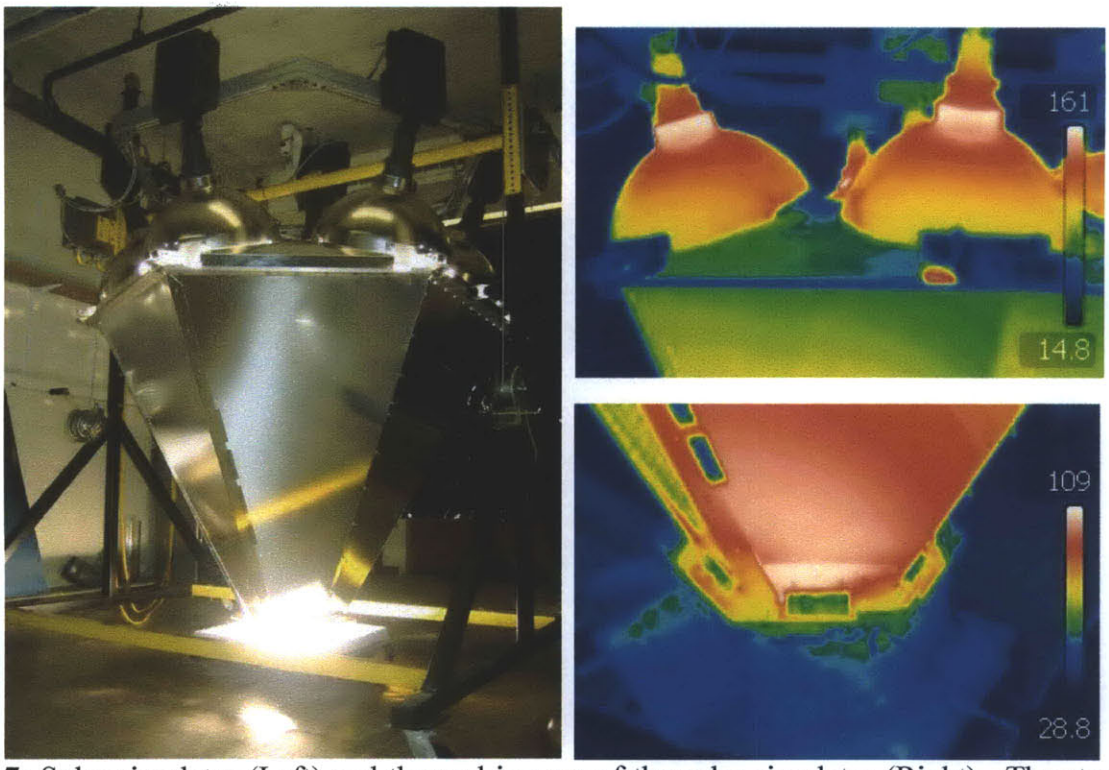

Figure 7: Solar simulator (Left) and thermal images of the solar simulator (Right). The steady state temperature of the housing for the metal halide bulbs is in the vicinity of 150° C, while the concentrator section of the simulator reaches temperatures in the order of 100° C. The steady state temperatures can be used to calculate the initial radiation losses to the environment.

3.4. Configurations

There are several configurations that are used through out the experiment. The first two configurations with the solar simulator lights on are shown in **Figure 8**. Configuration III and IV are with the lights off, shown in **Figure 9**.

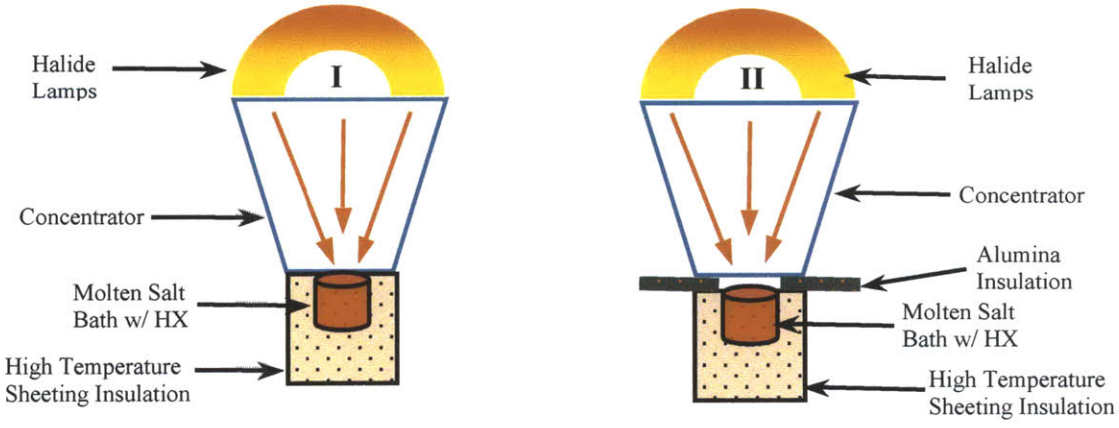

Figure 8: There are two experimental configurations with the solar simulator lights on. I) Solar simulator deposits energy to unshielded container assembly. II) Solar simulator deposits energy to a shielded container assembly. The shielding for configuration II consists of a high temperature alumina insulation plate 6.35 mm (1/4 in) thick.

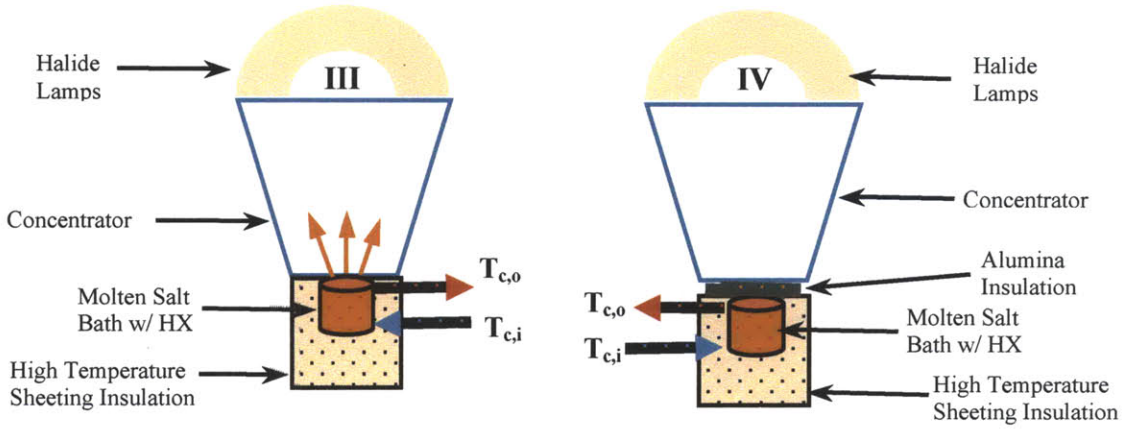

Figure 9: There are two experimental configurations with the solar simulator lights off. III) Heat removal with open container assembly. IV) Heat removal with a closed/insulated container assembly. The shielding cap for configuration IV consists of a high temperature alumina insulation plate 3.81 cm (1.5 in) thick.

3.5. Penetration Depth on Insulation Section

With the experimental setup in configuration I, a non-trivial amount of energy is deposited on the radial high temperature sheeting insulation through out the heating process. The deposited energy lowers the heat loss during the heating process there by lowering the amount of time to reach steady state. Initially the top surface of the insulation is at room temperature. When the lights are turned on the top layer begins to heat up. Over time, heat is transferred through the thickness of the insulation. The vertical depth into the insulation region that is affected by the energy deposited at the surface is called the penetration depth, as shown in **Figure 10**.

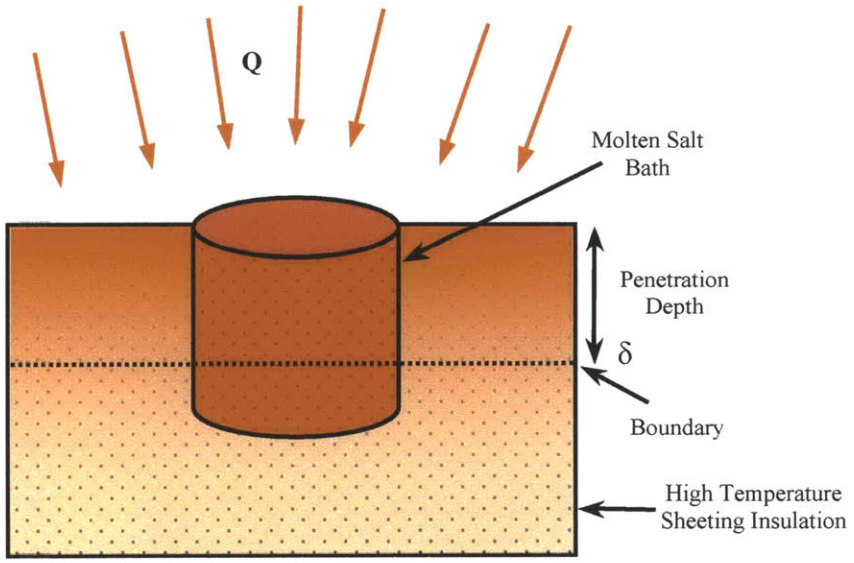

Figure 10: Schematic of penetration depth in the insulation material surrounding the molten salt container. Material below the boundary line is un affected by the energy deposited at the surface.

The penetration depth can be used to characterize the minimum depth to place the thermocouples such that the energy deposited from the solar simulator does not interfere with the measurement radial thermal measurements. The penetration depth for a semi-infinite system can be characterized using Equation 17[8]. The penetration depths for a three and four hour heating period are shown in **Table 2**.

$$\delta = 3.65\sqrt{\alpha \cdot t} \qquad \text{Equation 16}$$

Table 2: Penetration Depth Calculation for generic high temperature sheeting insulation over three and four hours. Items in **black bold** are inputs, and **red bold** are outputs.

Governing Equations	Parameters	
$\delta = 3.65\sqrt{\alpha \cdot t}$	t_{3hr} = **10,800 sec**	t_{4hr} = **14,400 sec**
$\alpha = \frac{k}{\rho \cdot C_p}$	$k_{Insulation}$ = **0.0375 W/(m*K)**	$(\rho * C_p)_{Insulation} \approx 3X10^6$ **J/(m^3*K)**
Results	δ_{3hr} = **4.2 cm**	δ_{4hr} = **4.9 cm**

From the calculation it follows that the penetration depth for a period of three hours is 4.2 cm, and with a period of four hours it is closer to 4.9 cm. Which means that the temperature in the radial direction as measured by the thermocouples should not be greatly affected by the applied heat flux from the top.

3.6. Instruments

K-Thermocouples

Temperatures are measured using air/immersion thermocouple probes[9]. The probes are connected to an Omega (TC-08 YSR80/249) logging tool reader that allows for the data to be stored electronically. The measurement error is less than 0.5° C. The response time is 0.5 seconds.

Flow meter

The mass flow rate is measured using an Omega mass flow meter with a digital readout[10], with a range from 0 to 10 standard liters per minutes (SLPM) calibrated with nitrogen gas. The maximum pressure that the flow meter can withstand is 250 Psig. The measurement error is one percent of the maximum flow rate, therefore 0.1 L/min. The flow meter has a response time of five seconds.

---

[8] Modeling and Approximation Heat Transfer by Glicksman and Lienhard, Section 3.2 pg 18

[9] 316SS Air/Immersion Thermocouple Probe Fiberglass Cable, Type K, 32-1700 F, 12" L Probe. (McMaster Part Number 39095K54). Some of the thermocouples were also manufactured in lab, using off the shelf components.

[10] Omega Massflow 0-10 SLM (FMA-A2309) . Accuracy : 1% full scale. Repeatibility: ±0.15% full scale. Gas Ambient temperature: 0 to 50 C. Temperature Coefficient: 0.05% full scale per 1 C or better. Input/Output Connection: 9 pin sub-D connector. Weight: 1.25 kg with power supply.

Air Compressor

The air compressor used to pump air through the heat exchanger is a Campbell Hausfeld model WL510005AJ, with a flow rate of 2.7 SCFM[11] @ 40 Psi. The air compressor cycles on and off to maintain a constant pressure thru the secondary valve. The pressure on the secondary valve is set to 40 bar through out the experiments. The pressure could drop down to as low as 35 bar when the pump is charging during operation. The air compressor was chosen based on availability.

FLIR Thermal Camera

A FLIR T300 thermal camera is used to identify thermal leaks in the setup. The temperature range is from -20° C to 600° C. The specifications for the camera show a spectral range between 7.5 and 13 μm. The temperature measurements have an accuracy of two percent.

3.7. Materials

3.7.1. Stainless Steel 316

The first salt bath container is from type 316 stainless steel. The alloy 316 has been used in the past with molten Sodium Nitrate Potassium-Nitrate salts, and in open systems exposed to oxygen it is virtually non reactive. Its low thermal conductivity of stainless steel 316 of 16.2 W/(m*K) at 100° C and 21.4 at 500° C makes it a reasonable material for housing 350° C salt bath.

3.7.2. Stainless Steel Wine Cooler

The second salt bath container is an off the shelf Chefmate Stainless Steel Wine Cooler[12], which has a air insulating plenum that helps minimize radial heat loses. The distributor verified that the plenum consists of air and not a vacuum. While the specific stainless steel alloy is not provided by the manufacturer, preliminary research shows that it can be type 304 which is typically used for cooking equipment, food processing equipment, etc.

3.7.3. Copper (Alloy 122) Tubing

The copper tubing used to make coiled tube heat exchangers is copper alloy 122[13]. The tube (characterized by outside diameter) has an outer diameter of 6.35 mm (0.25 inches), an inside diameter of 4.83 mm (0.19 inches), and wall thickness of 1.52 mm (0.03 inches). The melting point of the material is 1083° C. The technical operational range is between 0 and 205° C. However, the experiment will take the copper farther to temperatures as high as 360° C. The thermal conductivity of the copper alloy is 385 W/(m*K). The intended use is for natural gas, oil, or water. The tubing is soft annealed.

3.7.4. High Temperature Sheeting Insulation

The insulation material used is a high temperature sheeting insulation[14]. The insulation has the following properties: temperature range is -17 to 538° C (0-1000° F), thermal conductivity 0.0375 W/m^2*K (k factor 0.26 Btu/hr x in/sq ft @75° F), and density of 38.4 kg/m^3 (2.4 lbs/cu ft).

---

[11] Standard Cubic Feet per Minute
[12] ASIN: B001HIRL2Y, DPCI:070-05-3874
[13] ASTM B280
[14] Mcmaster part number 9356K11, high temperature insulation 1 inch thick used to wrap around the container.

3.7.5. *Zircar Alumina Insulation*

A sheet of 1/4 inch rigid alumina insulation is used to minimize the energy deposited by the solar simulator on the insulation region. The maximum rated temperature is 1700° C. The conductivity properties vary with temperature: $k_{250°C}$ = 0.16 W/m^2*K and $k_{525°C}$ = 0.20 W/m^2*K [Zircar Insulation]. The high temperature insulation has a specific heat of 0.25 J/(kg*K).

3.7.6. *Sodium Nitrate & Potassium Nitrate Mixture*

The salt used through out the experiments is a Sodium Nitrate Potassium Nitrate (50/50 wt%) salt mixture (5.1, UN1487, Pg I1) distributed by Coastal Chemical, Co. The thermodynamic properties of the salt in both solid and liquid form are given in **Table 3**.

The Sodium Nitrate-Potassium Nitrate mixture was chosen for its low melting point, around 220° C. One challenge with using the mixture is during the melting process, in its solid state the salt is highly reflective. The reflectivity concern can be addressed by inserting vertical conducting materials during startup to absorb the heat and transfer it down. Another option to solve the problem is by covering the solidified salt with little metal spheres that absorb light readily and conduct it to the solid salt. In the liquid state the molten salt can undergo convection, which helps with the mixing and eliminate temperature stratification in the pond. In the event of a catastrophic break in the container the salt can solidify thus preventing a major spill and making it easy to clean up.

Table 3: Hitec Salt Properties in the solid and melted phase.

	English Units		SI	
Solid				
Property	*ENGLISH*		*METRIC*	
Bulk Density	70-80	lb/ft^3	1200	Kg/ m^3
Melting Point	432	F	222	C
Specific Heat	0.29	BTU/(lb F)	1214	1214.17 J/(kg K)
Latent Heat of Fusion	57	BTU/lb	132582	m^2/s^2
Energy Required to melt and Bring melt to 550 F (288C)	206	BTU/lb	479156	m^2/s^2
Thermal Expansion	2.85 x 10^{-5}	F^{-1}	5.13 x 10^{-5}	C^{-1}
Liquid				
Specific Heat average	0.37	BTU/ (lb F)	1549	J/(kg K)
Density	112	lb/ft^3	1794.07	kg/m^3
Viscosity	2.1	cp	0.0021	Pa sec
Thermal conductivity	0.31	BTU/(hr ft F)	0.537	W/(m K)
Heat Transfer Coefficient	1164	BTU/(hr ft^2 F)	6609.5	W/(m^2 K)
Energy Density	43	BTU/(ft^3 F)	1.602x10^6	J/m^3
Thermal Expansion	2.016 x 10^{-4}	F^{-1}	3.629 x 10^{-4}	C^{-1}

4. Heat Exchanger Model

The objective of the thermodynamic model is to characterize heat exchanger performance for comparison against experimental data. The heat exchangers developed for the prototypes, designed for simplicity and low cost, is a series of helical coiled tubing, shown in Figure 11. The calculations for the helical coiled tube heat exchangers can be simplified as a straight tube with a constant exterior wall temperature or a temperature gradient in the outer wall, shown in **Figure 12**. The proposed model is a constant temperature source with a rising temperature receiver.

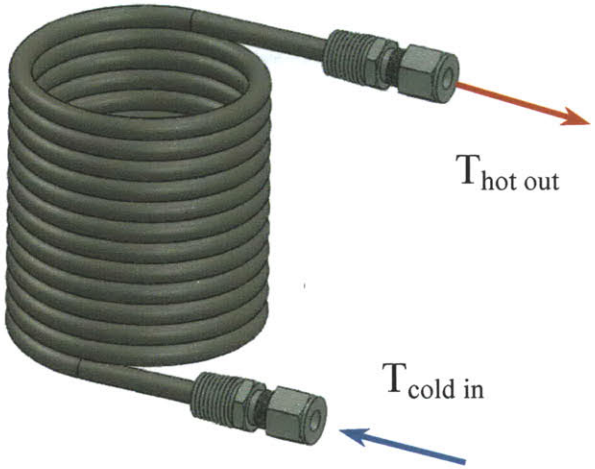

Figure 11: Basic coiled tube heat exchanger.

The helical coiled tube heat exchanger can be in direct or indirect contact with the molten salt bath. Direct contact implies that the coiled tubing is in contact with the molten salt. Indirect contact is when the coiled tube heat exchanger is outside of the salt container and in contact with the container wall. The temperature across the length of the heat exchanger can be constant or have a gradient through out the length as shown in **Figure 12**. A constant wall temperature assumes that the molten salt bath behaves like a heat reservoir transferring heat and entropy without lowering temperature.

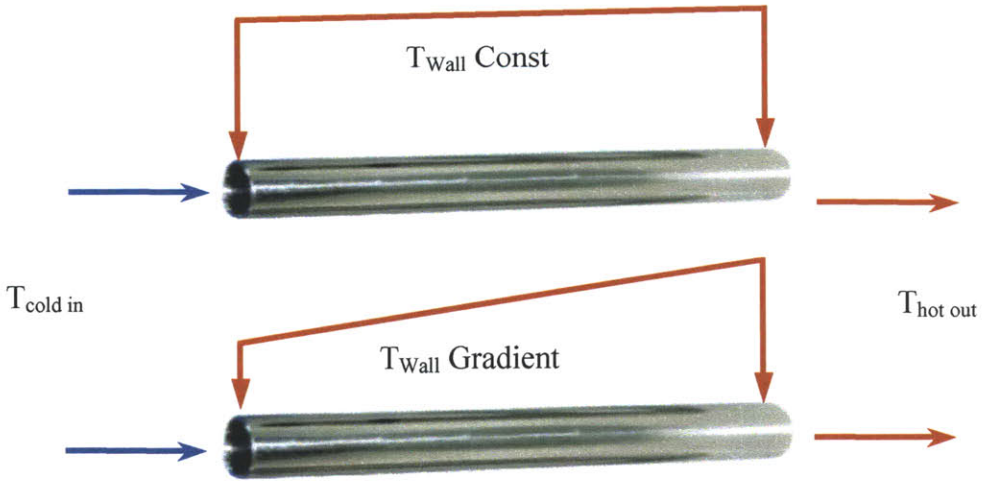

Figure 12: Heat exchanger tubing simplification with the temperature of the wall constant and the wall temperature as a gradient.

As heat is removed, the salt bulk temperature drops but the temperature along the tube length remains constant since the volumetric heat capacity for the molten salt is greater than that for the airflow. The medium with the lower volumetric heat capacity has the largest change in temperature. **Figure 14** shows a schematic of the temperature change for the molten salt and the air flow (not to scale) over the travel length.

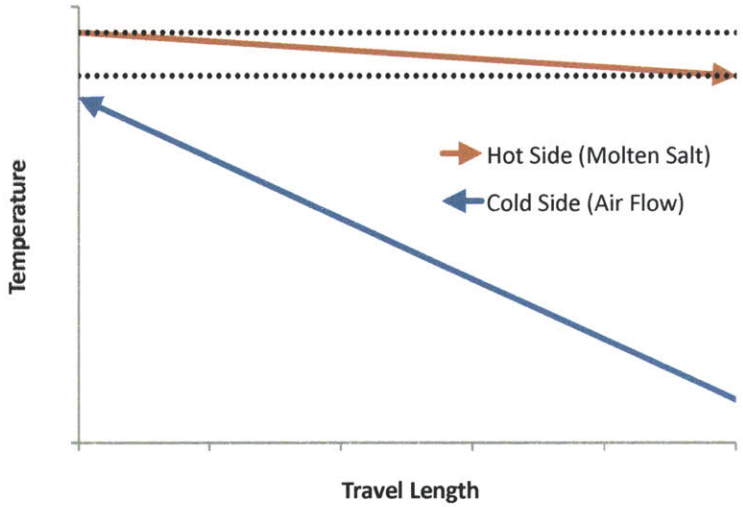

Figure 13: Volumetric heat capacity comparison between the molten salt and the air flowing inside the coiled tubing.

The volumetric heat capacity of the airflow is in the order ~$1x10^3$ J/(K*m^3), while the volumetric heat capacity of the molten salt is ~ $2.8x10^6$ J/(K*m^3); therefore, the temperature change is primarily in the airflow (cold side). The change in temperature of the hot side is considered much smaller than the temperature change of the cold side. The high thermal conductivity of the copper tubing also helps maintain the constant wall temperature.

4.1. Steady State Losses

There are four forms of heat losses that are accounted for in the steady state losses: 1) radial, 2) axial, 3) radiative, and 4) surface convection. **Figure 14** shows a cross sectional schematic diagram of the container assembly showing the loss regions.

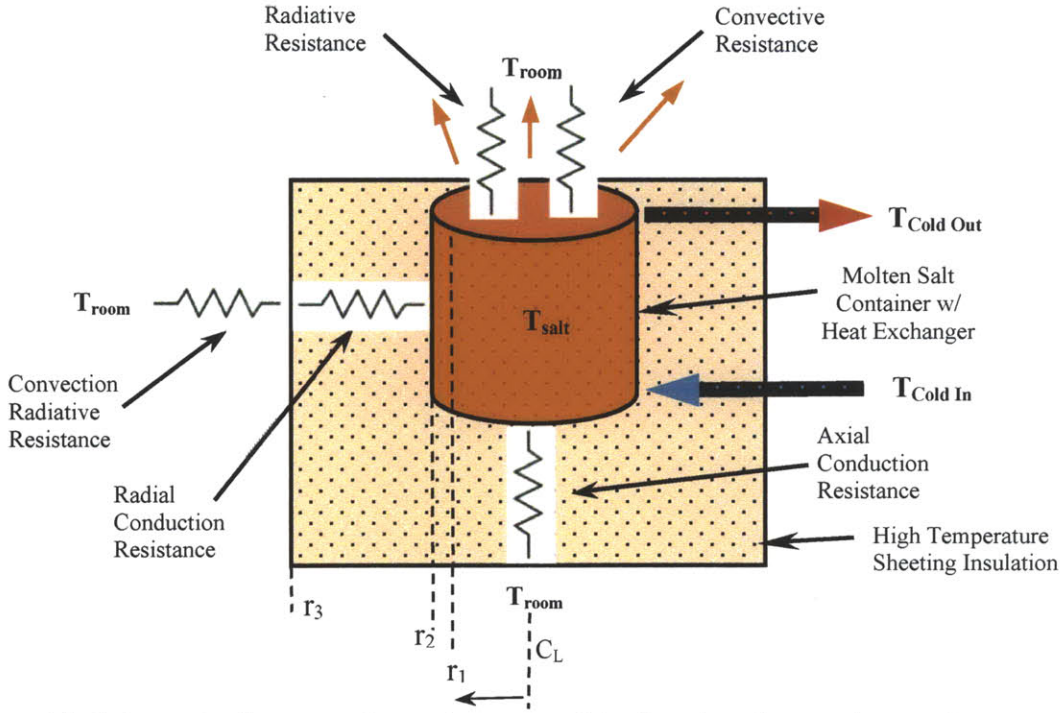

Figure 14: Schematic diagram of container assembly showing the steady state losses.

4.1.1. Radial Heat Loss

The radial heat loss Q'_{Radial} [W] is calculated using Equation 17, where T_{salt} is the bulk hot bath temperature, T_{room} is the ambient room temperature, and R_{tot} is the total thermal resistance[15]. R_{tot} is calculated using Equation 18, a simplified form of the total thermal resistance which does not include the following effects: 1) radiation heat transfer, 2) conduction inside the hot bath region, or 3) vertical temperature gradients. The following equations also assume that H_{length} is much larger than the radius, which may not be the case in some of the prototypes.

$$Q'_{Radial} = \frac{(T_{salt} - T_{room})}{R_{tot}} \qquad \text{Equation 17}$$

$$R_{tot} = \frac{\ln(r_2/r_1)}{2\pi \cdot k_{case} \cdot H} + \frac{\ln(r_3/r_2)}{2\pi \cdot k_{Insulation} \cdot H} + \frac{1}{h_{ext} \cdot 2\pi \cdot r_3 \cdot H} \qquad \text{Equation 18}$$

The thermal resistance due to conduction through the interior case, insulation, and exterior can be calculated using materials properties along with geometric parameters. The convection term may require the use of correlations in order to calculate an approximate the external convection term (h_{ext}).

[15] Heat and Mass Transfer (5th Ed) by Incropera, DeWitt Chp 3, Pg 106

4.1.2. Axial Heat Loss

One method for modeling the vertical heat loss through the bottom of the assembly is simplifying the system as composite plates with the total thermal resistance given by Equation 19. The heat loss from the bottom can be calculated using Equation 18 with the total thermal resistance R_{Bottom}.

$$R_{Bottom} = \frac{t_{case}}{k_{case} \cdot A} + \frac{t_{insulation}}{k_{insulation} \cdot A} + \frac{1}{h_{Bottom} \cdot A} \qquad \text{Equation 19}$$

4.1.3. Radiative Heat Loss Through the Top

When the top of the container is left open and the lights are off there are radiative losses $Q'_{Radiation}$ [W] to the environment. The losses due to radiation can be calculated using Equation 20.

$$Q'_{Radiation} = A \cdot \gamma \cdot \sigma \cdot (T_{salt}^4 - T_{room}^4) \qquad \text{Equation 20}$$

Where γ is the view factor, and σ is the Stefan Boltzmann constant, 5.670 x 10^{-8} J/(K^4*m^2*s).

4.1.4. Convection Top

The surface conduction/convection losses from the top of the salt can be simplified to a solid plate at a constant temperature under natural convection. The bulk temperature of the salt can be assumed to be uniform. The Rayleigh number is used to calculate the convection at the surface. Equation 21[16] is used to calculate the Rayleigh number, which is then used to calculate the Nusselt number using Equation 22 or Equation 23 depending on the Rayleigh number.

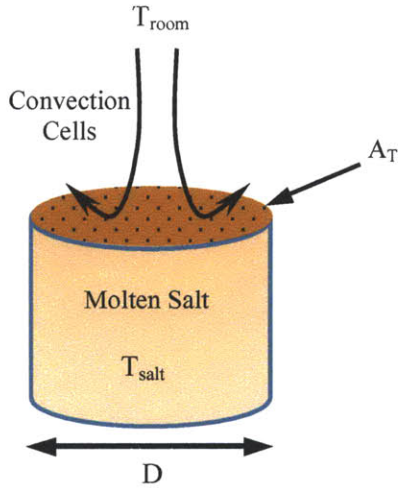

Figure 15: Surface convection losses schematic diagram

$$Ra_{l_c} = \frac{\beta_{air} \cdot (T_{salt} - T_{room}) \cdot g \cdot l_c^3}{v_{air} \cdot \alpha_{air}} \qquad \text{Equation 21}$$

Where l_c is the critical length of the surface, which is the diameter of the disk D.

[16] MIT 2.006 Course Notes (Spring 2008) by E. Cravalho Chp 10 pg 48

$$Criteria: \quad 10^5 < Ra_{lc} < 2x10^7$$

$$\overline{Nu_L} = 0.54 \cdot Ra_{lc}^{1/4} \qquad \text{Equation 22}$$

$$Criteria: \quad 2x10^7 < Ra_{lc} < 3x10^{10}$$

$$\overline{Nu_L} = 0.14 \cdot Ra_{lc}^{1/3} \qquad \text{Equation 23}$$

The heat loss due to the natural convection can be calculated with the calculated Nusselt number for the surface. The Nusselt number can be used to find an average surface convection coefficient using Equation 24. The heat loss per unit time due to natural surface convection can be determined using Equation 25.

$$Nu = \frac{h_{surf} \cdot l_c}{k_{air}} \qquad \text{Equation 24}$$

$$\dot{Q}_{Surf} = h_{surf} \cdot A_T \cdot (T_{salt} - T_{room}) \qquad \text{Equation 25}$$

Where h_{surf} is the natural convection coefficient at the surface of the salt, A_T is the top cross sectional area of the salt.

4.2. Losses Over Time

The time calculation of the steady state is done in step increments. At time zero (t = 0) the bath is assumed have a uniform bulk temperature. The thermal losses (watts) at time zero are calculated. The calculated losses (watts) are multiplied with the time step (seconds) to find the energy lost (J) during that time step. The energy loss (J) is subtracted from the total energy of the molten salt bath (J). With the new total energy of the system at time one (t = 1), a new bulk temperature for the molten salt mass is found using the first law. The new bulk temperature is used to calculate the thermal losses at time one. The thermal losses from time one allow are then used to calculate the energy loss from time one to time two, which lead to a new bulk temperature at time two. The calculations presented are carried out with one minute time steps. It is recommended to use a computer to carry out the calculation.

4.3. Calculated Heat Removal

The heat removal using a working fluid can be calculated using Equation 26[17]. The temperature values refer to the bulk temperatures of the working fluid.

$$q = m \cdot c_p \cdot (T_{C,O} - T_{C,I}) \qquad \text{Equation 26}$$

The heat removal from the molten salt bath can be done by passing water or air through the coiled tube heat exchanger shown in **Figure 11**. The thermal model used for characterizing the heat removal process is a tube with a constant wall temperature, as shown in **Figure 16**.

The heat transfer rate (Q'_P) from the walls of the coiled tube heat exchanger to the working fluid is described by Equation 27.

$$Q'_P = \dot{m} \cdot c_p \cdot (T_{C,O} - T_{C,I}) \qquad \text{Equation 27}$$

Where $T_{C,I}$ is the bulk temperature entering the tube, and $T_{C,O}$ is the bulk temperature exiting the tube. The mass flow rate can be described in terms of density of the medium, diameter of tubing, and average velocity, as shown by Equation 28.

$$\dot{m} = \rho \cdot A_c \cdot V_{avg} = \rho \cdot \left(\frac{\pi \cdot d_{tube}^2}{4} \right) \cdot V_{avg} \qquad \text{Equation 28}$$

Where ρ is the density of the medium, d_{tube} is the interior tube diameter, and V_{avg} is the average velocity of the working fluid.

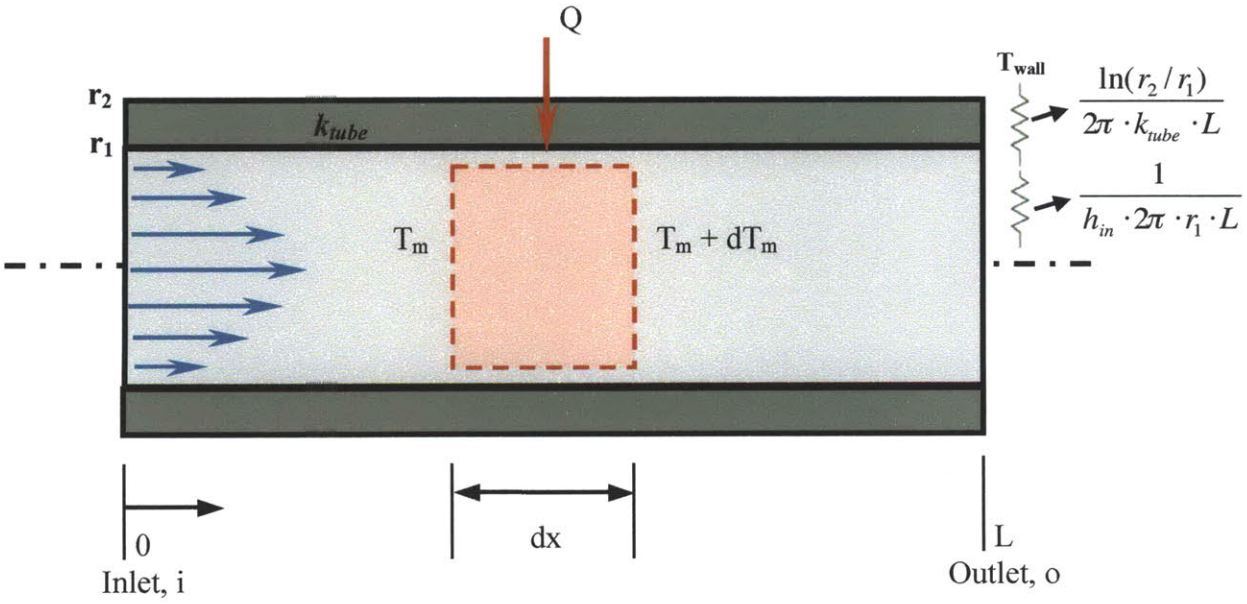

Figure 16: Control volume for internal flow in a tube with either a constant wall temperature or temperature gradient.

For a constant wall temperature the total resistance of the tube is shown in Equation 29. In a first order approximation the thermal resistance through the tubing is considered small.

[17] Heat and Mass Transfer (5th Ed) by Incropera, DeWitt Chp 2 pg 73

Refer to **Figure 16** for a schematic showing each thermal resistance in the radial direction for the tubing flow configuration.

$$R_{tot-tube} = \frac{1}{2\pi \cdot r_1 \cdot h_{in} \cdot L} + \frac{\ln(r_2/r_1)}{2\pi \cdot k_{tube} \cdot L} \qquad \text{Equation 29}$$

Where L is the length of the tubing, h_{in} is the forced convection coefficient.

The model is solved in conjunction with Equation 30, which applies for a tube with inner flow with a constant wall temperature. Equation 31 is obtained by simplifying $R_{tot-tube}$ (convection only) and rearranging Equation 30[18,19].

$$\frac{T_{c,i} - T_{salt}}{T_{c,o} - T_{salt}} = \exp\left(\frac{-1}{\dot{m} \cdot c_p \cdot R_{tot-tube}}\right) \qquad \text{Equation 30}$$

$$\frac{\Delta T_{out}}{\Delta T_{in}} = \exp\left(\frac{-\dot{m} \cdot c_p}{h_{in} \cdot 2\pi \cdot r_1 \cdot L}\right) \qquad \text{Equation 31}$$

Where R_{tot} can be set as the in terms of UA using Equation 11.

The convection coefficients must fall within the following parameter: fluids {min 150 W/(m^2*K), max 5000 W/(m^2*K)} and for gases {min 10 W/(m^2*K), max 250 W/(m^2*K)}[20]. The convection coefficients can be calculated by using the correlation shown in Equation 32[21], valid for fully developed laminar flow for centimeter-sized passages. For air, with k = 0.026 W/(m*K), a 5.8 mm diameter tube has a h = 20 W/(m^2*K). Another set of correlations for the flow inside a channel are provided in Equation 33[22] and Equation 34[23].

$$h_{in} = \frac{4.364 \cdot k_{air}}{d_{tube}} \qquad \text{Equation 32}$$

$$\textit{Criteria}: \quad (d/l) \cdot \mathrm{Re}_D \cdot \mathrm{Pr} < 0.03$$

$$\overline{Nu_D} = 1.953 \cdot \left[(d/l) \cdot \mathrm{Re}_D \cdot \mathrm{Pr}\right]^{1/3} \qquad \text{Equation 33}$$

$$\textit{Criteria}: \quad (d/l) \cdot \mathrm{Re}_D \cdot \mathrm{Pr} > 0.03$$

$$\overline{Nu_D} = 4.364 + 0.072 \cdot (d/l) \cdot \mathrm{Re}_D \cdot \mathrm{Pr} \qquad \text{Equation 34}$$

The calculated convection coefficient for air using Equation 34 is 33 W/(m^2*K), also within the established limits and close to the first calculated value.

Figure 17 shows the air output temperature, $T_{b,out}$, as a function of the length of the tubing, l, for the minimum, maximum, and calculated convection coefficient along with the heat

[18] Heat and Mass Transfer (5th Ed) by Incropera, DeWitt Chp 8 pg 483
[19] MIT 2.006 Course Notes (Spring 2008) by E. Cravalho Chp 11 Pg 13
[20] Modeling and Approximation Heat Transfer by Glicksman and Lienhard Chp 1, pg 7 Table 2.1
[21] Modeling and Approximation Heat Transfer by Glicksman and Lienhard Chp 4.2, pg 13
[22] MIT 2.006 Course Notes (Spring 2008) by E. Cravalho Chp 11 Pg 20
[23] MIT 2.006 Course Notes (Spring 2008) by E. Cravalho Chp 11 Pg 20

removal for the calculated heat transfer coefficient. As mentioned earlier, the convection coefficient for a gas has to be between 10 and 250 W/(m^2*K)[24].

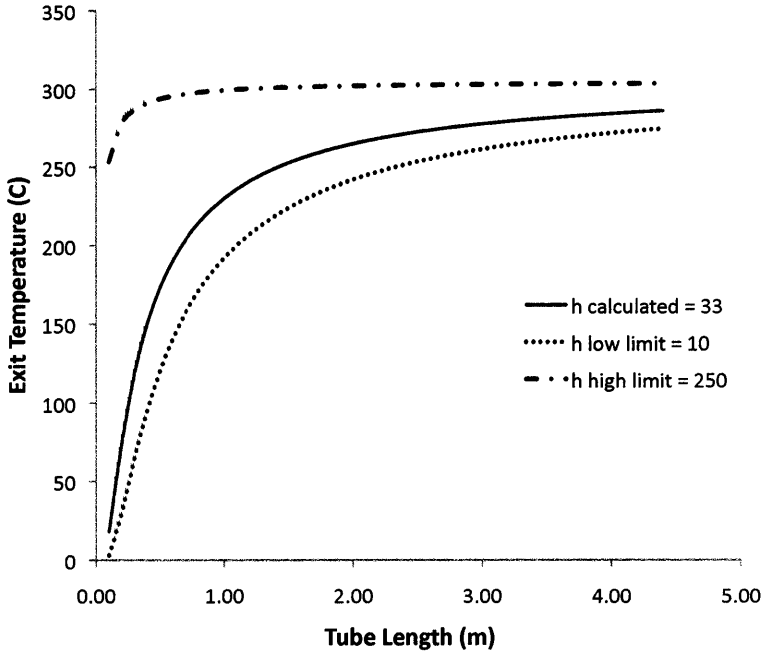

Figure 17: Output temperature of air as a function of tube length for the following convection coefficients: minimum (10 W/(m^2*K)), maximum (250 W/(m^2*K)), and calculated (33 W/(m^2*K)) using Equation 34. The outer surface temperature of the tube is assumed to be 330° C. The calculation assumes uniform temperature through out the tube and perfect contact.

4.3.1. Predicted Heat Extraction

The predicted heat extraction is obtained by using the salt bulk temperature (for the given data) at an instantaneous point in time to calculate the ideal change in temperature (ΔT) of the fluid (air flowing through tubing). The ideal ΔT for the air temperature is then used in the first law of thermodynamics to calculate the theoretical heat extraction. As the bulk temperature decreases so does the theoretical heat extraction. An important factor is that the theoretical heat extraction is calculated using the salt bulk temperature of the data; therefore, any error in the bulk temperature approximation (from theory) is removed from the calculation.

[24] Modeling and Approximation Heat Transfer by Glicksman and Lienhard Chp 1, pg 7 Table 2.1

4.3.2. Heat Removal Calculation Flow Chart

In order to better follow the calculation procedure the flow chart shown in **Figure 18**, which can be used for reference through out the calculation process.

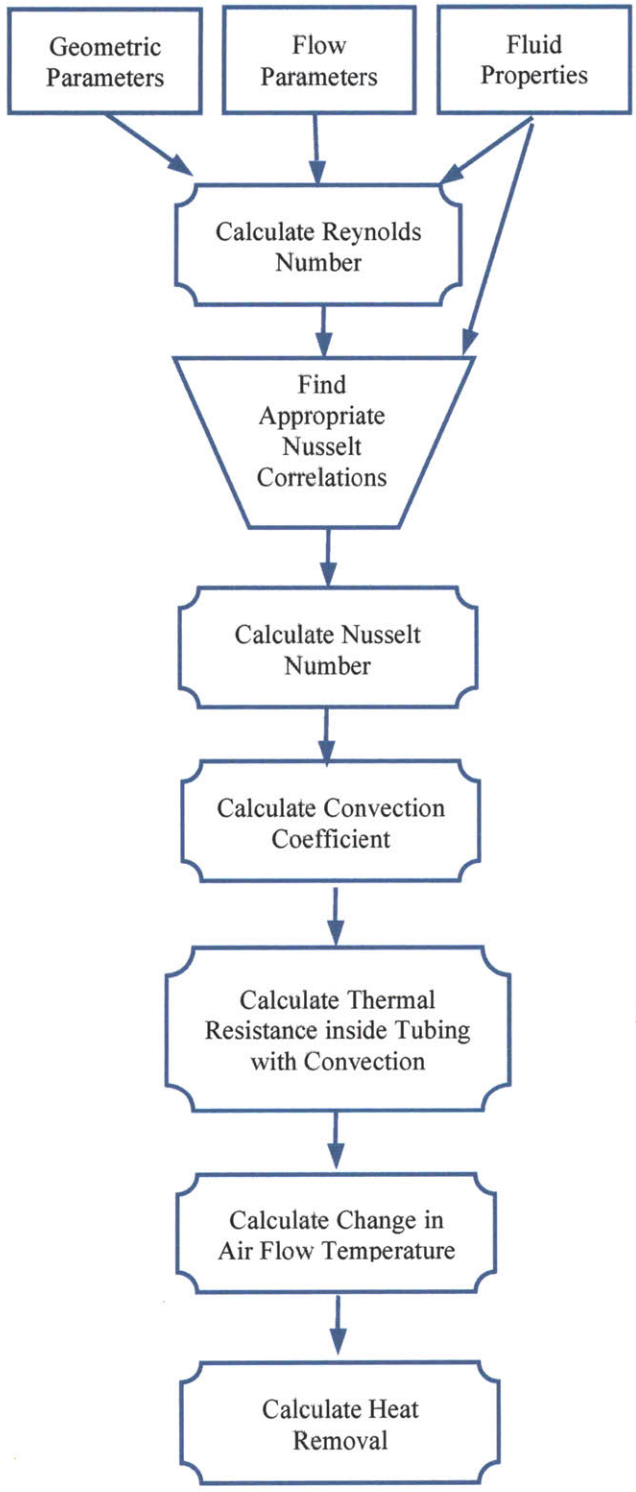

$$\mathrm{Re} = \frac{4 \cdot \dot{m}}{\pi \cdot \mu \cdot d}$$

$$Nu = f(D, L, \mathrm{Re}, \mathrm{Pr})$$

$$Nu = \frac{h_{in} \cdot D}{k_f}$$

$$R_{tot-tube} = \frac{1}{2\pi \cdot r_1 \cdot h_{in} \cdot L} + \frac{\ln(r_2 / r_1)}{2\pi \cdot k_{tube} \cdot L}$$

$$\frac{T_{c,i} - T_{salt}}{T_{c,o} - T_{salt}} = \exp\left(\frac{-1}{\dot{m} \cdot c_p \cdot R_{tot-tube}}\right)$$

$$Q_P' = \dot{m} \cdot c_p \cdot (T_{C,O} - T_{C,I})$$

Figure 18: Heat removal calculation flow chart

5. 0.55 kg Coiled Tube Heat Exchanger

The first prototype (*P-I*) can hold a mass of 0.55 kg of molten salt. The salt mixture is melted using the solar simulator. The objectives of *P-I* are the following: 1) melt salt with solar simulator, 2) proof heat removal concept, 3) compare radial temperature gradient, and 4) determine heat removal calculation.

5.1. Design

As discussed earlier, there are many possible heat exchanger designs for removing the heat form a molten salt reservoir. Evaluating between the different heat exchangers (i.e. parallel flow, counter flow, shell and tube, etc.) one of the better choices for the prototype heat exchanger is a coiled tube heat exchanger in direct contact with the molten salt; however, the first iteration of the design has the coils outside of the salt bath for safety purposes. An explosive exothermic reaction can result if water were to come into contact with the molten salt. The working fluid was also chosen to be air to further minimize accidents during the experimental process. **Figure 19** shows a coiled tube heat exchanger that can hold an estimated 0.55 kg of salt.

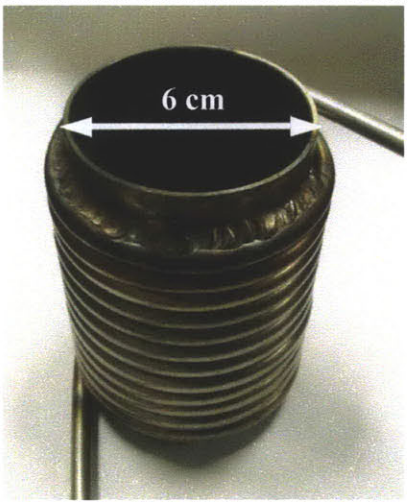

Figure 19: Test bed heat exchanger first prototype. Coiled tube heat exchanger made from a stainless steel casing surrounded by ¼ inch stainless steel tubing, with a total contact length of 2.74 meters. The tubing was coiled and welded at the top and bottom contact surfaces of the helical coil. Therefore, the middle section between the tubing and container is only under pressing contact, there is no brazing along the length.

The materials and diameters of the test bed model were chosen by availability of the parts, ease of manufacturing process, and thermal properties. Although the stainless steel casing reduces the amount of heat conducted to the coils, it functions effectively as an insulator.

5.1.1. Coiled Tube Heat Exchanger

The coiled tube heat exchanger consists of stainless steel cylinder capped at one end and surrounded by ¼ inch tubing in a helical shape. The tube outer diameter is 6.35 mm (0.25 inch), interior diameter 4.83 mm (0.19 inch), and has a total contact length of 2.74 meters with the container wall. The tube is welded at the top and bottom to the stainless steel tubing. Both the bottom and upper tube have male 1/4 inch Yor-Lok tube fittings. The mass calculated with the

Solidworks model is 0.525 kg, compared to the experimental setup 0.558 kg. **Figure 20** shows the model of the coiled tube heat exchanger and a cross section view.

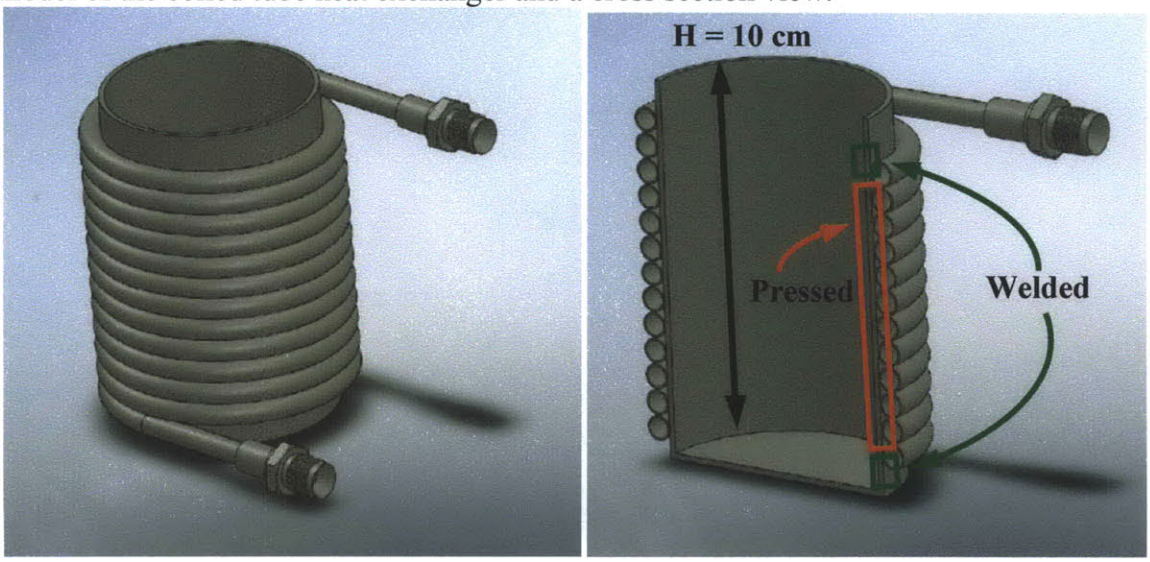

Figure 20: Coiled tube heat exchanger model with cross section view. Maximum volume 270 cm^3. Total contact length of 2.74 meters. Ends are male Yor-Lok fittings for ¼ inch tubing. The calculated mass is 0.525 kg (no welding included). The weighted mass is 0.558 kg. The coiled tubing is welded to the cylinder at the top and bottom only and not continuously.

5.1.2. *P-I* Schematic Layout

The schematic diagram for P-I is shown in **Figure 21**. The bold line is the location of the temperature versus radius plot measurements. The depth of the radial temperature measurements is greater than the penetration depth.

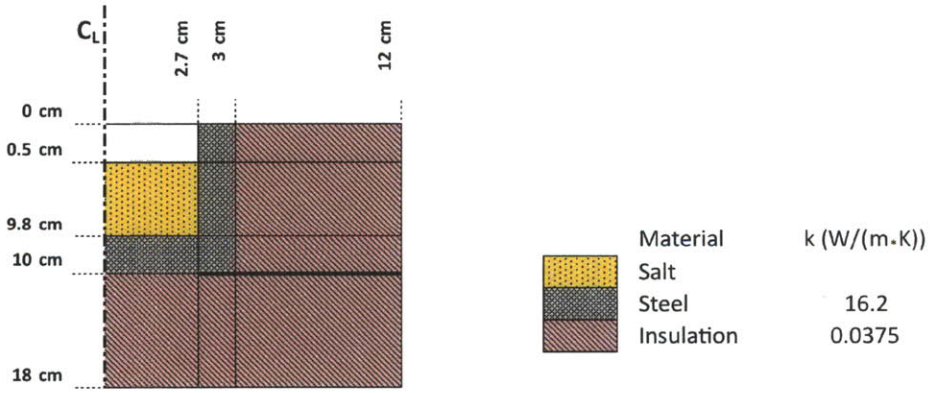

Figure 21: Cross section diagram of *P-I*. The dashed line is the axial location of the temperature versus radius plot.

5.1.3. Energy Deposited

At the center the solar simulator can deliver 50 kW/m^2. The diameter of the container is around 5.4 cm, which yields an area of 2.29×10^{-3} m^2. The energy deposited on the molten salt is 114.5 Watts.

5.1.4. Initial Losses

There are four main types of losses: 1) radial conduction, 2) axial conduction from the bottom surface, 3) radiative and convective top surface losses to the environment. **Table 4** shows the losses calculations for the four main losses, totaling ~ 42 W. The calculated losses are upper bound estimates.

Table 4: *P-I* initial thermal losses due to conduction, surface radiation and surface convection losses. Items in **black bold** are inputs, and **red bold** are outputs.

Objective: Calculate Thermal Losses				
Radial Conduction $R_{tot} = \frac{\ln(r_2/r_1)}{2\pi \cdot k_{case} \cdot H} + \frac{\ln(r_3/r_2)}{2\pi \cdot k_{Insulation} \cdot H} + \frac{1}{h_{ext} \cdot 2\pi \cdot r_3 \cdot H}$				
r_1 = 2.7 cm	**r_2 = 3 cm**	**h ~ 10 W/(m*K)**	**k_{case}= 20 W/(m^2*K)**	**$T_{2=Salt}$ = 360° C**
r_3 = 12 cm	**H = 10 cm**		**$k_{insulation}$= 0.038 W/(m^2*K)**	**$T_{3=Room}$ = 30° C**
R_{tot} ~ 60 K/W				
				Q'_{Radial} ~ 5.4 W
Axial Conduction $R_{Bottom} = \frac{t_{case}}{k_{case} \cdot A} + \frac{t_{insulation}}{k_{insulation} \cdot A} + \frac{1}{h_{Bottom} \cdot A}$				
$t_{insulation}$ = 8 cm	**k_b= 0.038 W/(m^2*K)**	**T_1 = 360° C**		
r = 3 cm		**T_2 = 30° C**		
R_{Bottom} ~ 750 K/W				
				Q'_{Bottom} ~ 1/2 W
Surface Radiation $Q'_{Radiation} = A \cdot \gamma \cdot \sigma \cdot (T_{salt}^4 - T_{room}^4)$				
A_T = 2.83x10^{-3} m^2	**T_{room} = 30° C**	**T_{salt} = 360° C**	**σ = 5.670 x 10^{-8} J/(K^4*m^2*s)**	
				$Q'_{Radiation}$ ~ 24.4 W
Surface Convection $Ra_{lc} = \frac{\beta_{air} \cdot (T_{salt} - T_{room}) \cdot g \cdot l_c^3}{\nu_{air} \cdot \alpha_{air}}$				
β_{air} = 3.55 x 10^{-3} K^{-1}	**g = 9.8 m/s^2**	**T_{room} = 30° C**	**l_c = 5.7 cm**	
ν_{air} =14.2x10^{-6} m^2/s	**α_{air} = 2.25x10^{-5} m^2/s**	**T_{salt} = 350° C**		
Ra_{lc} = 6.05 x 10^6				
Criteria : $10^5 < Ra_{lc} < 2x10^7$ $\Rightarrow$ $Nu = \frac{h_{surf} \cdot l_c}{k_{air}}$ $\Rightarrow$ $Q'_{surf} = h_{surf} \cdot A_T \cdot (T_{salt} - T_{room})$ $\overline{Nu_L} = 0.54 \cdot Ra_{lc}^{1/4}$				
Nu_{Lc} ≈ 28.5	given **k_{air} = 0.0264 W/(m*K)**		**h_{surf} ≈ 12.5 W/(m^2*K)**	
				Q'_{Surf} ~ 11.7 W
				Total Heat Loss Rate: 42 Watts

5.1.5. Heat Extraction Calculation

The calculation for finding the convection coefficient inside of the tube with flowing air is shown in **Table 5**. Using the values from the experimental setup, a convection coefficient of 33.3 W/m^2*K was determined. The calculated convection coefficient is in the lower end of the spectrum. Since the air flow temperature changes as a function of time a Reynolds number versus exit air temperature plot is provided, see **Figure 22**. The Reynolds vs. exit air temperature plot shows that for air temperatures greater than 90° C the Reynolds number is below 2000 (laminar).

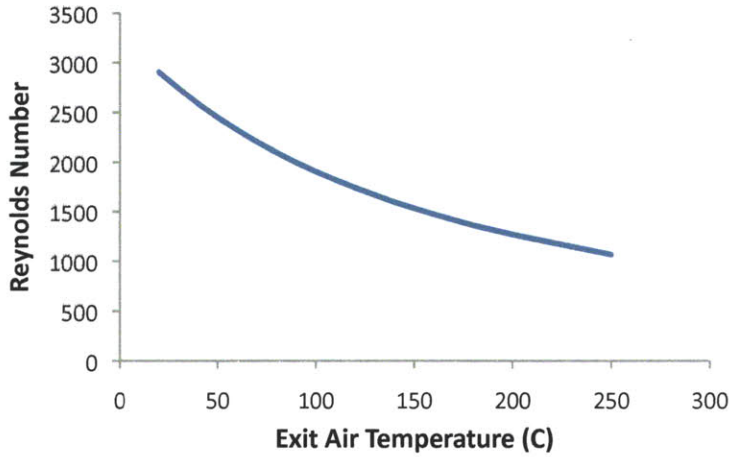

Figure 22: Reynolds number versus exit air flow temperature for a 10 SLPM flow rate. Since the properties of air vary over the range of temperatures, therefore the Reynolds number must also change. Notice that exit temperatures greater than 90° C have Reynolds values less than 2000, therefore the flow is laminar.

Table 5: Calculation for small heat exchanger maximum convection coefficient for 0.5 kg Size Unit. A flow of 10 SLPM results in a convection coefficient of 33.3 W/(m^2*K). Reducing the mass flow rate to 5 SLPM changes the convection coefficient to 32.8 W/(m^2*K) which is a minimal change. Items in **black bold** are inputs, and **red bold** are outputs.

Objective: Calculate convection coefficient inside the tubing with flowing air		$\mathrm{Re} = \frac{4 \cdot \dot{m}}{\pi \cdot \mu \cdot d_{tube}}$
d_{tube} = 0.00483 m	**Pr_{160C} = 0.69** **μ_{160C} = 2.43x10^{-5} kg/(m*sec)**	**$\dot{m}$ = 10 SLPM** **$\dot{m}_{160C}$ = 1.36 x 10^{-4} kg/sec**
Re_D=1471		
Correlation Criteria $(D/H) \cdot \mathrm{Re}_D \cdot \mathrm{Pr} > 0.03$		*Correlation* $\overline{Nu_D} = 4.364 + 0.072 \cdot (d_{pipe}/H) \cdot \mathrm{Re}_D \cdot \mathrm{Pr}$
Nu_D = 4.5		
		$\overline{Nu_D} = \frac{h_{in} \cdot d_{tube}}{k_f}$
k_f = 0.0358 W/(m*K)		
		h_{in} = 33.3 W/(m^2*K)

The calculated initial energy removal rate for *P-I* is 37.9 watts, as shown in **Table 6**. The calculation for the energy removal is an upper bound estimate due to the following assumptions: uniform wall temperature along tube diameter, constant wall temperature through out the length of the tube.

Table 6: Heat Removal for *P-I*. The final data has bath bulk temperatures in the 330° C range. Items in **black bold** are inputs, and **red bold** are outputs.

Objective: Calculate heat removal for *P-I*		
		$R_{tot-tube} = \frac{1}{2\pi \cdot r_1 \cdot h_{in} \cdot L} + \frac{\ln(r_2/r_1)}{2\pi \cdot k_{tube} \cdot L}$
r_1 = 0.00483 m **r_2 = 0.00635 m**	**L = 2.7 m**	**h_{in} = 33.3 W/(m^2*K)** **k_{tube}=380 W/(m*K).**
$R_{tot-tube}$ = 1.81x10^{-3}		
c_P = 1013 J/(kg*K) **T_{wall} = 330° C**	**$\dot{m}$ = 10 SLPM** **$\dot{m}_{150C}$ = 1.4x10^{-4} kg/sec**	$\frac{\Delta T_{out}}{\Delta T_{in}} = \exp\left(\frac{-\dot{m} \cdot c_p}{h_{in} \cdot 2\pi \cdot r_1 \cdot L}\right)$
ΔT = 285° C		
		$Q'_P = \dot{m} \cdot c_p \cdot (T_{b,out} - T_{b,in})$
		Q'$_P$ = 37.9W

5.2. Finite Element Analysis

The finite element analysis assumes that the temperature of the casing is 360° C based on preliminary data. The radial temperature distribution is a lower bound estimate given that the heat flux through the top is overlooked, since the penetration depth of the system is smaller than the depth of the container.

The model has 5 cm of fictitious insulation at the bottom created to minimize the thermal losses at the bottom. The 5 cm of insulation are to account for an insulation brick where the assembly is mounted. The convection coefficient at the exterior wall of the unit is assumed to be 10 W/(m*K) for natural convection. The first order approximation shows little dependence on the natural convection coefficient.

Figure 23 shows the radial temperature distribution and a color schematic cross section for the first prototype container, assuming that the energy deposited across the top surface of the insulation is insignificant. The insulation temperature versus radius plot shows that the temperature through the insulation should an exponential decay appearance, which agrees with the analytical simplified model. The plot also shows that the conduction through the bottom of the container does not create axial temperature gradients in the exterior insulation.

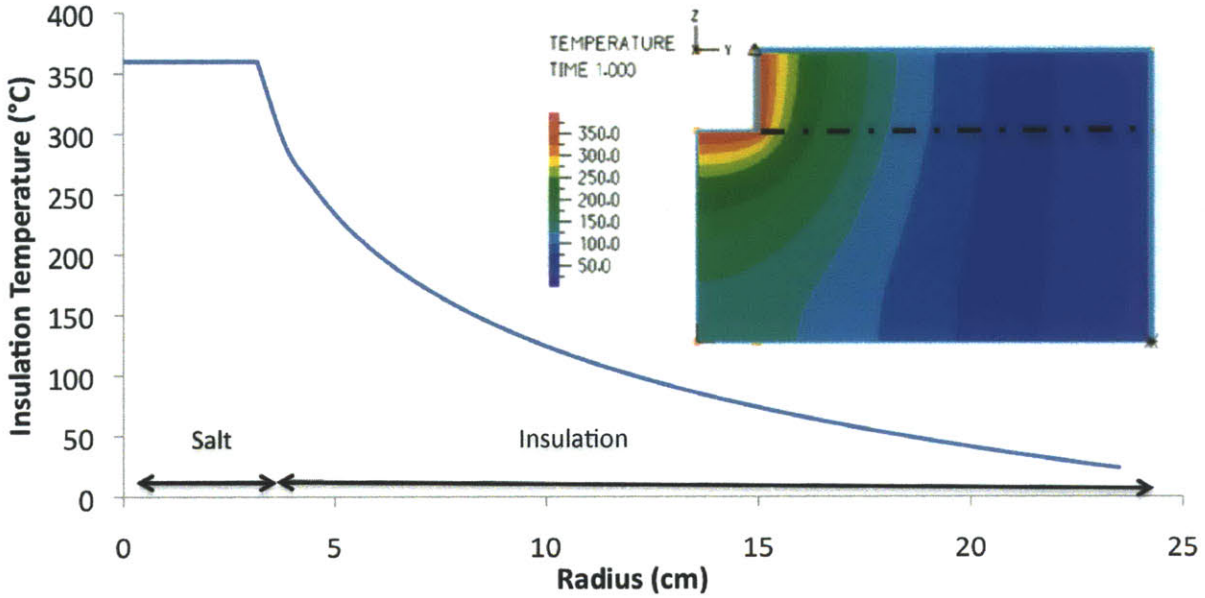

Figure 23: Finite Element Analysis for heat dissipation through out the insulation. The insulation has a thermal conductivity of 0.0375 W/(m*K). The model does not take into account the energy deposited on top insulation surface by the solar simulator. The energy deposited at the top will not affect measurements taken beyond the penetration depth. The dashed line is the axial location of the temperature versus radius plot.

5.3. Preliminary Tests

A series of preliminary tests were performed in order to get an understanding for the system behavior and the influence of changing certain parameters in the experimental setup.

5.3.1. Melting Process

The melting process of a solid piece of nitrate salt mixture takes place from the exterior wall towards the inside since the salt is reflective in the solid state. **Figure 24** shows how the melting process goes from the outside to the inside of the container. Thermocouples in the center of the container reveal that in the melting process there is a significant temperature gradient in the vertical direction. As the salt reaches steady state conditions the vertical temperature gradient disappears.

Figure 24: Series of images showing the melting process of the salt through out time. The image on the left is at the onset of melting. The center image shows the progression of melting from the sides and the sinking of the solid salt. The image on the right shows the fully melted salt bath.

5.3.2. Copper Tubing Insertions

While the copper inserts are not necessary to melt the salt, the inserts change the melting profile and are expected to shorten the time to reach full melt. The salt in its solid state is highly reflective; therefore, during the heating process the absorption decreases hence increasing the time to melt the sample. In order to decrease the time to reach the melting point copper tubing was added to increase the conduction to the salt. The melting process was changed but a significant time reduction was not measured with this prototype. **Figure 25** shows time sequenced photos of the melting process.

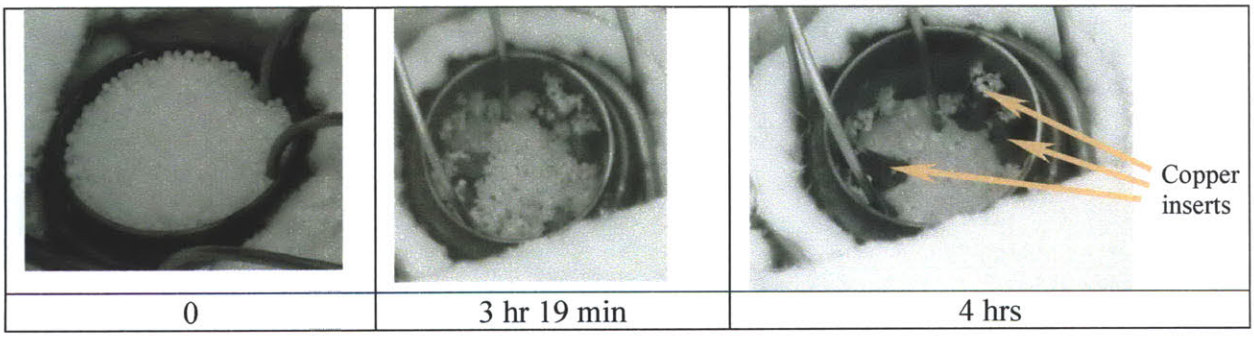

Figure 25: Nitrate Salt mixture undergoing the melting process with copper insertions to speed up the melting process.

5.3.3. Air Flow Temperature Measurements

The air flow temperature measurements are done with two different setups. The inlet temperature which is approximately 30° C is measured with a T-junction setup, where the k-thermocouple measures the temperature of the passing air. The exit air flow temperature is done with a wire k-thermocouple. The bead is a weld that connects the nickel-chromium (+ lead) and nickel-aluminum (- lead). The resistance between the wires is correlated to the temperature of the bead. The placement of the bead along centerline of the tubing can cause error in the

temperature measurement. **Figure 26** shows the entry and exit air flow temperature measurement geometries.

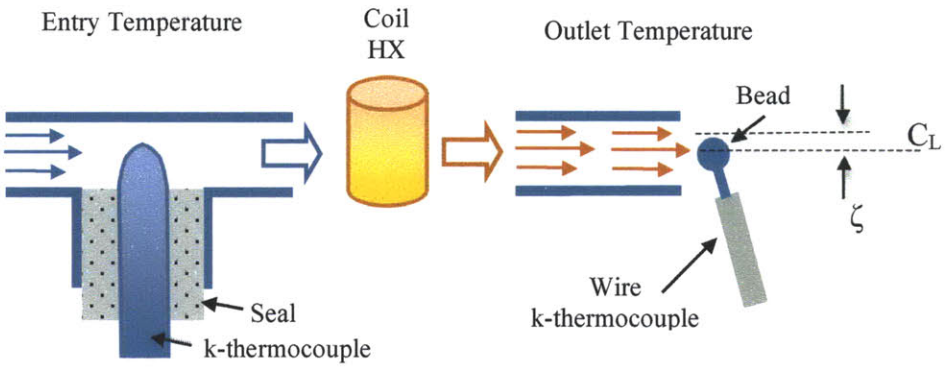

Figure 26: Air flow temperature measurement at the entry and at outlet. Misalignments in the placement of the bead (ζ) from the centerline of the exit flow can lead to error in the temperature measurement.

5.4. Data

The data collected for the small heat exchanger prototype was focused on capturing the following: 1) the temperature gradient in the insulation, 2) comparing flow configuration, and 3) determining energy removal capabilities.

5.4.1. Insulation Temperature Gradient

The temperature gradient through out the insulation is measured using three k-thermocouples placed inside the insulation. The thermocouples were placed at 10 cm below the top surface. Given that the penetration depth after four hours is less than 5 cm, the radial temperature measurements should remain unaffected by the energy deposited on the uncovered insulation region. **Figure 30** compares the radial temperature measurements, the FEA model, and the analytical solution. The dashed line shown in **Figure 23** is the axial location of the temperature versus radius plot.

5.4.2. Flow Configuration

The flow configuration for the coiled tube heat exchanger can be either from top to bottom or vice versa. With the concentrator lights on, the temperatures are highest near the top of the bath. As shown by the data in **Figure 31** the amount of energy harvested varies with the configuration. The top to bottom flow collects less energy the bottom to top configuration with the same flow rate. The collected data ends when the bulk temperature reaches 275° C, with the exception of flow rates lower than 5 SLPM which were not taken to completion. The more energy is extracted by the flow the shorter it takes to cool the thermal mass.

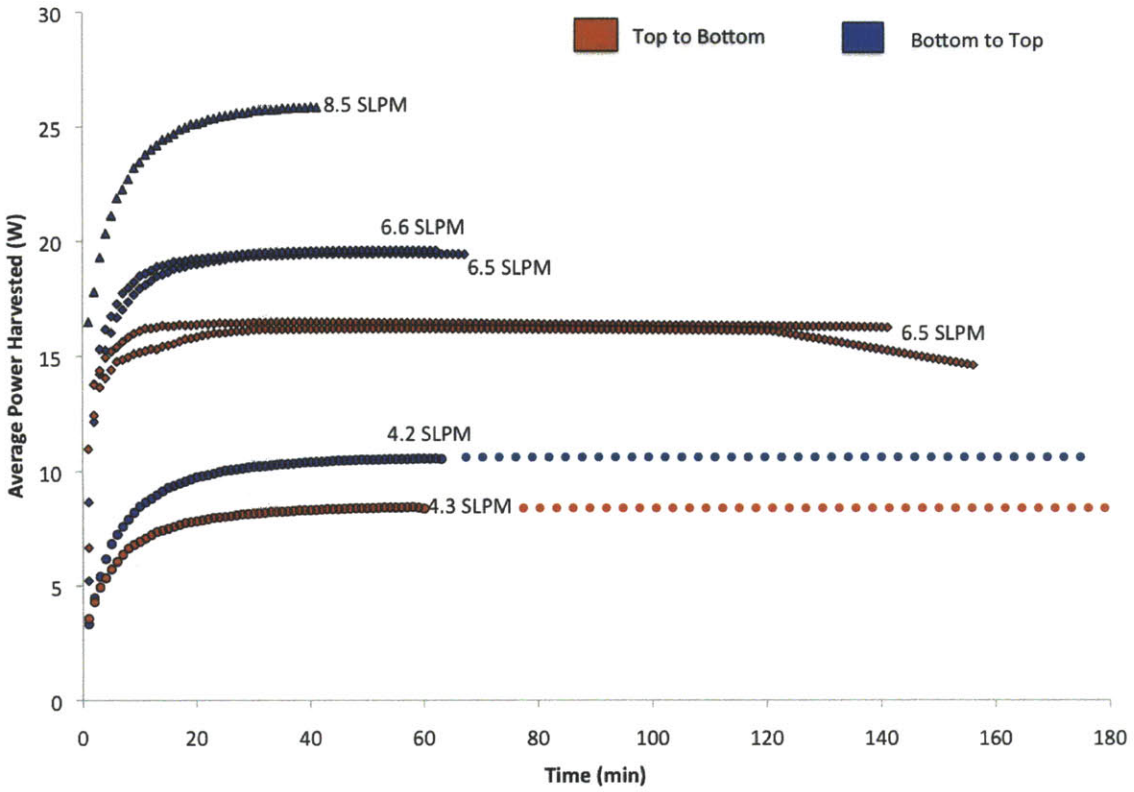

Figure 27: Comparing the average power harvested for the same configuration with the exception of flowing from top to bottom and from bottom to top. The lights were left "on" for the configuration in order to prove the effect. Flowing from bottom to top preheats the working fluid allowing it to reach higher temperature. The flow from top to bottom does not allow for preheat but it can last longer as much of the energy is harvested from the newly deposited heat. Flow rates below 5 SLPM were not carried out until the average bath temperature reached 275° C.

5.4.3. Spheres Additives

The adding 14 stainless steel spheres (0.5" outer diameter) reduced the time to melt from a solid block of salt from 4.25 hours to 3.42 hours. Adding spheres reduced the time to reach steady state by ~45 minutes on a 0.55 kg mass of sodium-nitrate potassium-nitrate salt.

5.4.4. Lights Off

Harvesting thermal energy with the lights off is representative of the night time conditions. With the lights off a 0.550 kg mass undergoes a temperature change of 60° C (335 to 275° C) in 15-20 minutes. **Figure 28** shows the energy harvesting capabilities *P-I* for a bottom to top (BT) flow configuration at two different flow rates with there respective theoretical values.

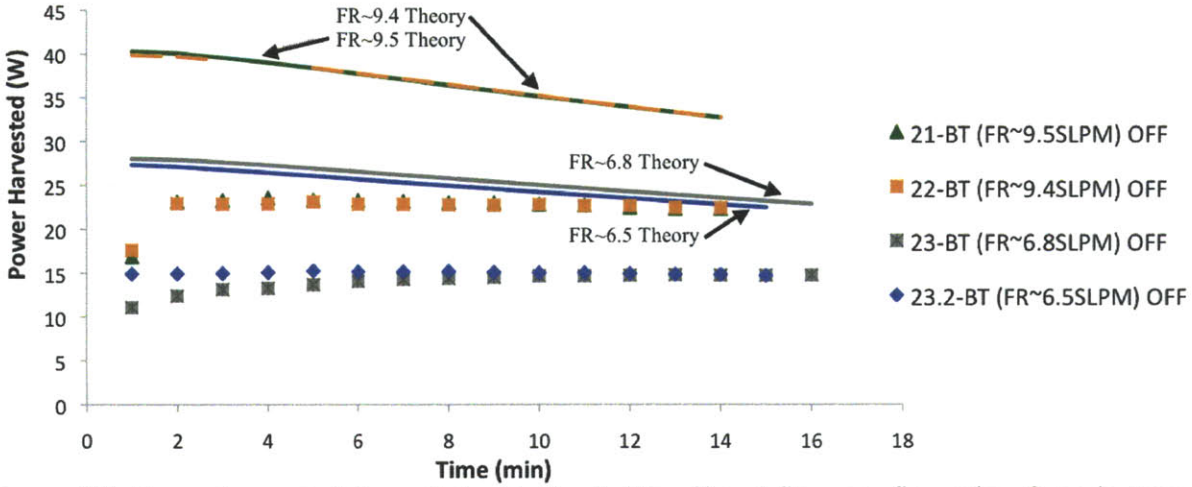

Figure 28: Power harvested from *P-I* with the lights off and flow configuration from bottom to top. The curves for the theoretical values are also plotted as solid lines. Bulk temperature drops from 330 to 275° C. The theoretical values are obtained from using the expected change in temperature at the given salt bath bulk temperature. Data set 21-BT and data set 22-BT lie one on top of the other.

The temperature loss calculation does not capture accurately model the thermodynamic behavior of *P-I*. The collected data is precise, comparing two data samples under the same geometry boundary conditions. It is hypothesized that the error in the heat loss model is from not accounting for the k-thermocouples (3 used to measure depth temperature) acting like fins. Heat can be loss by conducting through the thermocouples and convecting to the environment. Even though there is an experimental setup error, the measured losses are within 25 percent of the theoretical values, see **Figure 29**. The discrepancy between the model and data can be addressed by either 1) accounting for the heat loss through the thermocouples, or 2) change the type of k-thermocouples.

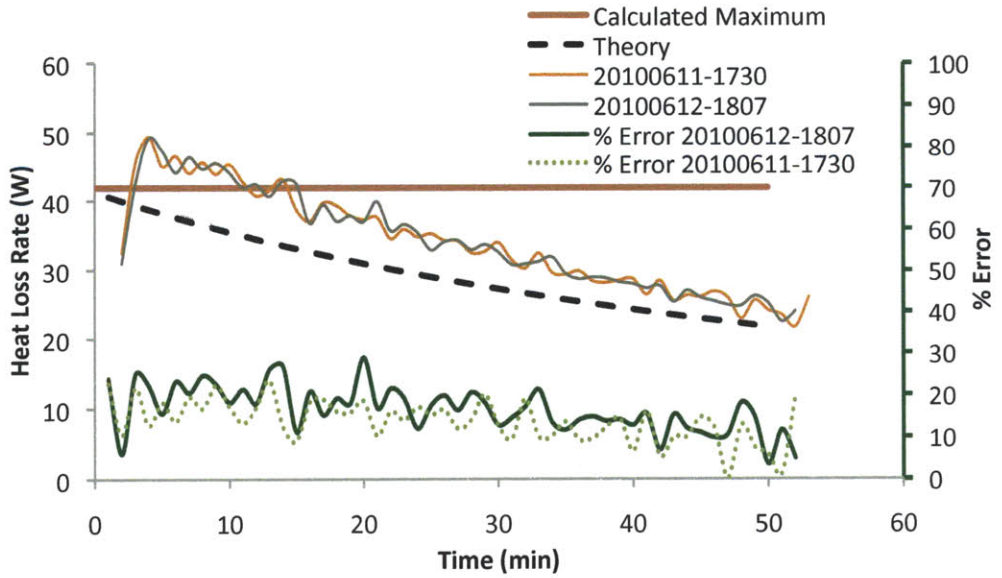

Figure 29: *P-I* heat loss comparison between theory and data. The maximum error between theory and data is 29 percent.

5.5. Results

The four objectives of the first prototype were met: 1) melt salt with solar simulator, 2) proof heat removal concept, 3) compare radial temperature gradient, and 4) determine heat removal calculation. The sodium nitrate (60 %) potassium nitrate (40 %) salt was melted using the solar simulator. The power extraction concept was confirmed and captured by the thermodynamic model. The radial temperature gradient through out the insulation was characterized. The accuracy of the power extraction model is within 46 % for the first prototype. The error in the power extraction calculation is reasonable considering that the stainless steel heat exchanger is not immersed in the molten salt and the thermal conductivity through the geometry. The heat loss rate model is lower than measured data. The model has an average error of 17 %, and a maximum error 28.9 %. The discrepancy between the measured data and model is attributed to the k-thermocouples behaving like fins thus increasing the losses.

5.5.1. Insulation Temperature Gradient

Comparing the temperature profile inside the insulation to the FEA model with a fixed temperature at the vessel wall shows that the model is not accurate. To account for the discrepancy, a second model was developed that includes both the radial conduction and energy deposited on top of the surface of the insulation. Adding 180 W/m^2 from the center of the container decreasing in the radial direction proves to be a more accurate thermal model. **Figure 30** compares the collected model to the radial model, and the radial model with top energy. Work done on the following prototypes will show that there may be another effect that is leading

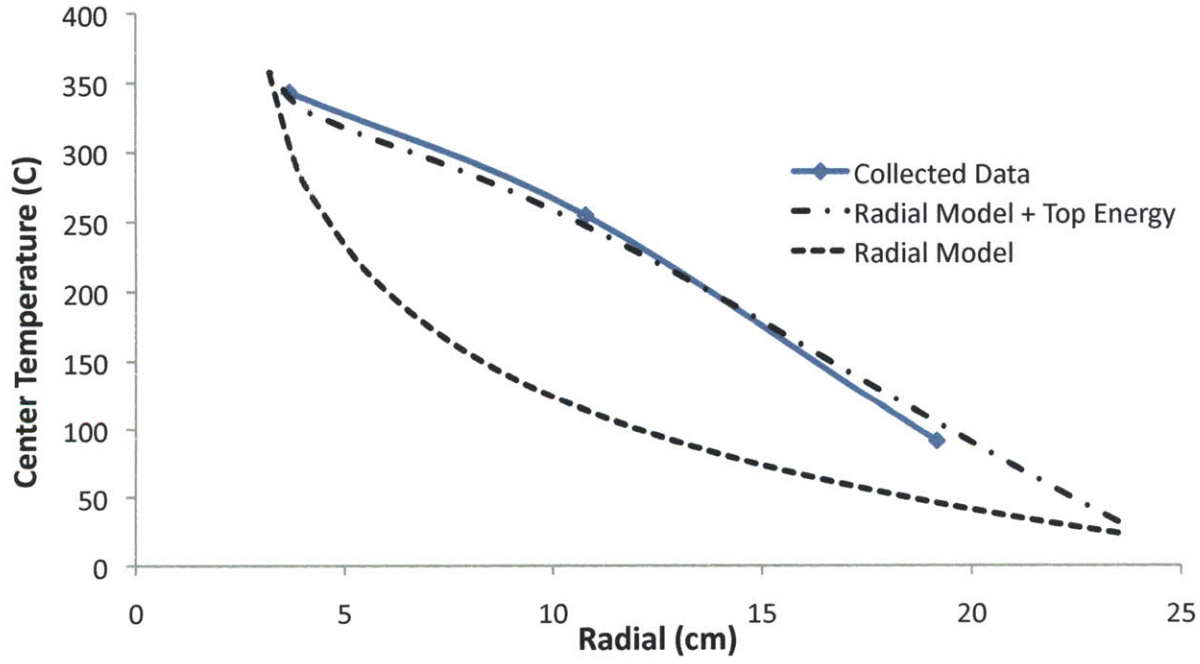

Figure 30: The FEA model without the heat flux to the top of the insulation (---) shows a significant lower temperature than that measured. Adding a decreasing radial energy distribution to the top of the insulation provides a more accurate model that compares well to the collected data. Adding 180 W/m^2 from the center of the container decreasing in the radial direction proves to be a more accurate thermal model.

5.5.2. Flow Configuration

The flow configuration shows that with the lights on the bottom to top configuration can collect more energy than the top to bottom configuration. The reason is due to preheating that occurs with the bottom to top configuration. In the TB configuration the fluid gets most of its energy in the beginning and losses some of the energy to the lower temperatures at the bottom of the tank. Therefore, when it comes down to producing energy during the day it may be best to extract more energy from the top of the reservoir.

5.6. Lessons Learned

5.6.1. Start Up Heating Process

A solid chunk of salt inside the reservoir begins to melt inwards from the receiver walls in the radial direction. Has the wall of the container reaches the salt melting point the salt begins to melt. Due to the high reflectivity of the salt in its solid state the center of the container does not melt in comparison to the salt in contact with the edges of the container.

5.6.2. Flow Temperature Measurements

Some of the first round temperature measurements were under measuring the hot air flow temperature measurement due to the large thermal mass associated of the thermocouple. Originally the thermocouples were held in a T-junction. Placing another type of K-thermocouple, welded wire thermocouple, in front of the hot flow stream demonstrated that the original temperature measurements were low due to the heating of the thermal mass. More accurate temperature measurements are obtained by placing the wire k immersion thermocouples in the exiting stream, which results in a higher and more accurate calculated heat removal. Using the thermocouple wire and placing the bead in the center of the flow significantly decreased the delay in the temperature response; however, it is much more sensitive to placement.

5.6.3. Start Up

The salts should be pre-melted and all of the contaminants removed prior to introducing into the large reservoir. Melting a large container of solid salt may require additives such as copper tubing or spheres for the start up procedure. A preliminary experiment showed that the time to reach 90 % S.S value was reduced by 18 % by adding spheres to the surface of the solid salt. The improvements of the additives should be further examined with the larger prototypes.

5.6.4. Heat Loss Calculation

The discrepancy in the heat loss calculation to the data is attributed to conduction through the k-thermocouples, which are acting as fins in the current configuration. *P-II* should look at changing the k-thermocouples to reduce the thermal mass. One option is to use welded bead thermocouples, which would minimize conduction and reduce the thermal mass.

6. 2.20 kg Coiled Tube Heat Exchanger

Prototype II (*P-II*) is a coiled tube heat exchanger inside the salt bath to reduce the radial thermal gradient with a 2.20 kg salt capacity. The purpose of the larger unit is to: 1) provide larger thermal mass, 2) measure steady state temperature gradient inside the salt, 3) compare insulation temperature gradient, 4) heat removal longevity, and 5) confirm convection in the salt.

6.1. Design

The heat exchanger implemented is a coiled tube heat exchanger that is placed inside the salt bath. The placement of the coiled tube heat exchanger was altered in order to minimize the temperature difference between the molten salt bath and the surface temperature of the heat exchanger tubing. The heat exchanger tubing material was also changed to copper (alloy 122) to further reduce thermal gradients. The copper tubing is expected to corrode due to the molten nitrate salt; however, the lifetime of the experiments is much less than the time for the corrosion to be a serious concern. A production industrial unit could sacrifice the thermal conductivity of copper for corrosion resistant properties of other materials (i.e. stainless steel 316). The coiled tube heat exchanger is in the top half of the vessel to remove the most thermal heat during the day and to produce a natural convection cycle by cooling the hot salt and the top and forcing it to sink to the bottom. The establishment of the natural convection cycle aids the heat transfer of the molten bath.

The container for the bath is a dual wall stainless steel container that is usually used as a wine cooler. The dual wall feature provides an air plenum insulation layer that serves to reduce radial thermal losses. **Figure 31** shows the copper heat exchanger inside of the stainless steel container. The diameter of the entire assembly is 0.46 m (18 in). The outer diameter of the container is 6.3 cm (4.95 in). There is 0.127 m (5 in) of insulation at the bottom of the container.

Figure 31: Medium coiled tube heat exchanger is inside of the chefmate stainless steel double wall cooler that serves as the bath container. The stainless steel wine cooler provides an additional air plenum to reduce thermal losses. The ends of the heat exchanger are female Yor-Lok fittings for ¼" tubing, which connect to male-male adapter for connecting to the other tube sections that lead outside of the heating region. The image on the left shows the heat exchanger inside the cooler surrounded by fiberglass insulation. The image on the right shows the double layer cooler. The total height of the cooler is 19.4 cm (7.625 inches) with an interior height of 18.1 cm (7.125 inches). The mass of the cooler is 0.529 kg. The material wall thickness was measured to be 0.1 mm (0.004 in) from a sample cut to backup container at the center of the container.

6.1.1. Coiled Tube Heat Exchanger

The coiled tube heat exchanger consists of ¼ inch copper (alloy 122) tubing shaped into an eleven turn coil with an outer diameter of 11.18 cm (4.4 inches). The outer diameter of the copper tubing is 6.35 mm (0.25 inch), with a total wall thickness of 0.76 mm (0.03 inches). The total contact length of the copper tube with the salt bath is 3.8 m (150 inches). Both the ends of the heat exchanger have Yor-Lok tube fittings for ¼ inch. **Figure 32** shows the model of the coiled tube heat exchanger and a cross section view.

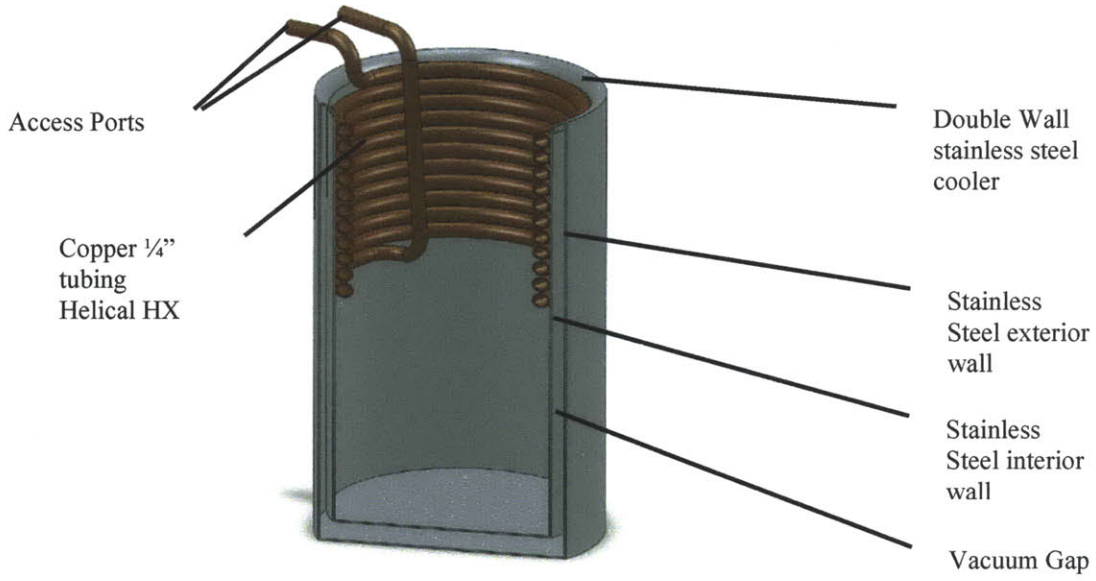

Figure 32: Coiled tube heat exchanger model with cross section view showing the parts of the container and coiled tube heat exchanger. The maximum volume of the cooler without the heat exchanger is 1775 cm^3. The total contact length is 3.8 meters (150 in). Ends are female Yor-Lok tube fittings for ¼ inch. The mass of the cooler is 0.529 kg. The mass of the copper is 0.421 kg.

6.1.2. Energy Deposited

The top cross sectional area of the cooler is 9.9×10^{-3} m^2 (15.4 in^2). Assuming the concentrator is delivering 50 kW/m^2, the energy deposited on the pond is 495 watts (~0.5 kW).

6.1.3. Initial Losses

There are four main types of losses: 1) radial conduction, 2) bottom surface conduction, 3) radiation losses. **Table 7** shows the losses calculations for the four main losses, totaling 126 W. The radial losses are estimated at 5.6 W. The losses through the bottom due to conduction are 1.2 W, radiation losses from the top are 85 W, and surface convection losses 34 W. The losses are upper bound estimates, as the bulk temperature of the container decreases so will the losses.

Table 7: *P-II* initial thermal losses due to conduction and radiation. The initial thermal losses are at least 126 watts. Items in **black bold** are inputs, and **red bold** are outputs.

Objective: Calculate Thermal Losses
Radial Conduction $$R_{tot} = \frac{\ln(r_2/r_1)}{2\pi \cdot k_{case} \cdot H} + \frac{\ln(r_3/r_2)}{2\pi \cdot k_{Insulation} \cdot H} + \frac{1}{h_{ext} \cdot 2\pi \cdot r_3 \cdot H}$$
r_1 = 5.2 cm r_2 = 5.3 cm r_3 = 6.2 cm $h \sim 10$ W/(m*K) k_{23}= 0.049 W/(m²*K)@350 $T_{2,Salt}$= 360° C **r_4 = 6.3 cm r_5 = 22.9 cm H = 10 cm k_{34}= 0.038 W/(m²*K) $T_{5,Room}$= 30° C**
$R_{tot} \sim$ 58.6 K/W **$Q'_{radial} \sim$ 5.6 W**
Axial Conduction $$R_{Bottom} = \frac{t_{case}}{k_{case} \cdot A} + \frac{t_{insulation}}{k_{insulation} \cdot A} + \frac{1}{h_{Bottom} \cdot A}$$
t = 12.7 cm $k_{insulation}$ = 0.038 W/(m²*K) T_1 = 360° C **r = 6.2 cm T_2 = 30° C**
$R_{Bottom} \sim$ 277 K/W **$Q'_{Bottom} \sim$ 1.2 W**
Surface Radiation $$Q'_{Radiation} = A \cdot \gamma \cdot \sigma \cdot (T_{salt}^4 - T_{room}^4)$$
A_T = 9.9x10⁻³ m² T_{room} = 30° C T_{salt} = 360° C σ = 5.670 x 10⁻⁸ J/(K⁴*m²*s)
$Q'_{Radiation} \sim$ 85 W
Surface Convection $$Ra_{lc} = \frac{\beta_{air} \cdot (T_{salt} - T_{room}) \cdot g \cdot l_c^3}{\nu_{air} \cdot \alpha_{air}}$$
β_{air} = 3.55 x 10⁻³ K⁻¹ g = 9.8 m/s² T_{room} = 30° C l_c = 10.4 cm **ν_{air} =14.2x10⁻⁶ m²/s α_{air} = 2.25x10⁻⁵ m²/s T_{salt} = 350° C**
Ra_{lc} = 3.67 x 10⁷
Criteria: $2x10^7 < Ra_{lc} < 3x10^{10} \Rightarrow Nu = \frac{h_{surf} \cdot l_c}{k_{air}} \Rightarrow Q'_{surf} = h_{surf} \cdot A_T \cdot (T_{salt} - T_{room})$ $\overline{Nu_L} = 0.14 \cdot Ra_{lc}^{1/3}$
$Nu_{Lc} \approx$ 47 given k_{air} = 0.0264 W/(m*K) ***$h_{surf} \approx$ 11.8 W/(m²*K)*** **$Q'_{Surf} \sim$ 34 W**
Total Heat Loss Rate: 125.8 Watts

6.1.4. Heat Extraction Calculation

The convection coefficient for the air flow inside the coil tubing is 33.3 W/(m*K) as calculated for the previous HX in **Table 5**. The calculated initial energy removal rate for *P-II* is 41.7 watts, as shown in **Table 8**. The calculation for the energy removal is an upper bound estimate.

Table 8: Power Removal for *P-II* given is 41.7 watts. Items in **black bold** are inputs, and **red bold** are outputs.

Objective: Calculate heat removal for P-II		
		$R_{tot-tube} = \frac{1}{h_{in} \cdot 2\pi \cdot r_1 \cdot L} + \frac{\ln(r_2/r_1)}{2\pi \cdot k_{pipe} \cdot L}$
r_1 = 0.00483 m **r_2 = 0.00635 m**	**L = 3.8 m**	**h_{in} = 33.3 W/(m^2*K)** **k_{tube}= 380 W/(m*K)**
$R_{tot-tube}$ = 0.26 K/W		
C_P = 1013 J/(kg*K) **T_{wall} = 360° C**	**$\dot{m}$ = 10 SLPM** **$\dot{m}_{150C}$ = 1.4x10^{-4} kg/sec**	$\frac{\Delta T_{out}}{\Delta T_{in}} = \exp\left(\frac{-\dot{m} \cdot c_p}{h_{in} \cdot 2\pi \cdot r_1 \cdot L}\right)$
ΔT = 297° C		
		$Q'_P = \dot{m} \cdot c_p \cdot (T_{b,out} - T_{b,in})$
		Q'$_P$ = 41.7W

6.2. Finite Element Analysis

A finite element model can be used to trace the temperature profile through out the insulation given the wall temperature of the container. The first order models assumes that the temperature inside of the casing is 360° C as shown by preliminary experiments.

6.2.1. Geometry & Boundary Conditions

Figure 33 shows the cross section of prototype two with the dimensions that pertain to the model. The model is made as an axisymmetric model about the center line (C_L). There are two boundary conditions applied to the FEA model. The salt is set to be a uniform temperature of 360° C and the surface of the insulation at 30° C.

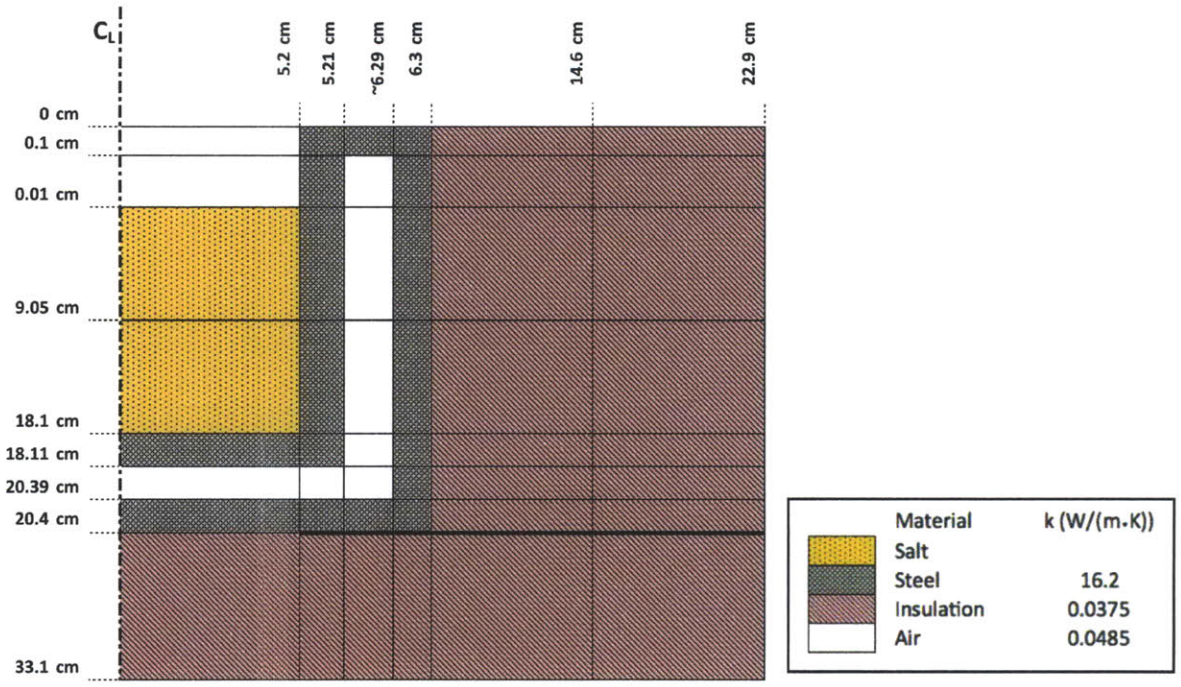

Figure 33: *P-II* geometry dimensions and the materials for each region. The bold line is the location of the temperature measurements and where the radial temperatures are compared. The thermal conductivity for air is at 350° C.

6.2.2. Results

The radial temperature gradient from the finite element analysis is shown in **Figure 34**.

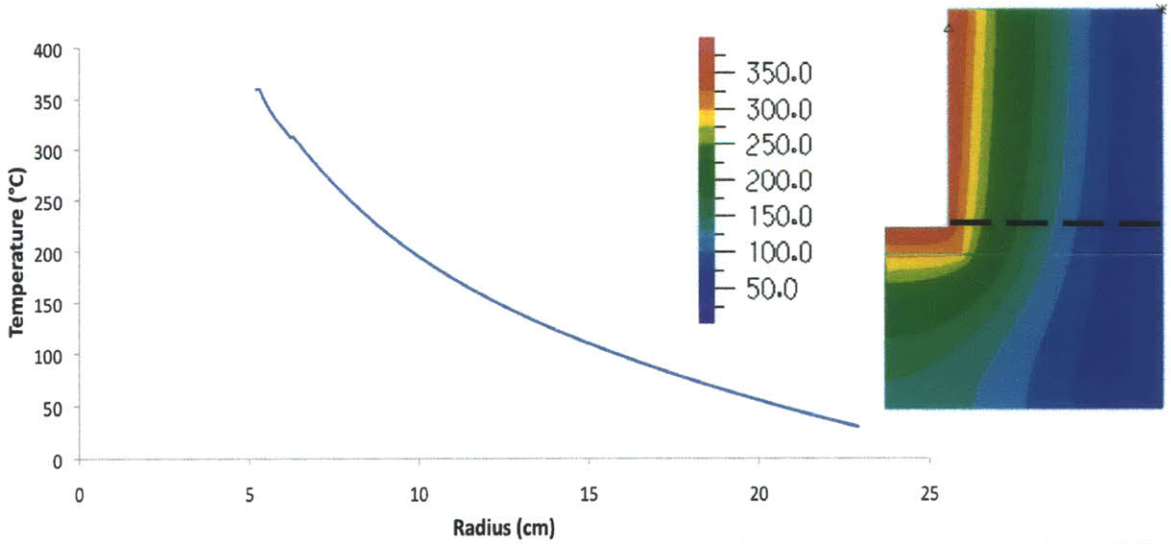

Figure 34: FEA Radial temperature profile and image of the thermal cross section of the unit. The dashed line is the axial location of the temperature versus radius plot.

6.3. Data

The data collected for second prototype focuses on capturing the following: 1) insulation temperature gradient, 2) energy harvesting, 3) molten salt temperature gradient, 4) exterior thermal image, 5) flow thermal image, and 6) molten salt convection.

6.3.1. Insulation Temperature Gradient

The insulation temperature gradient of *P-II* also shows higher temperatures in the center region of the insulation, as shown in **Figure 35**. The theoretical model and the FEA reasonably agree. The temperature measurements don't agree with the theory or FEA model. The location of the thermocouples coincides with the dashed line is in the FEA model shown in **Figure 34**. In order to find the reason for the discrepancy, a high temperature insulation plate was then placed to see the effect on the radial temperature gradient, as shown in **Figure 36** (experimental configuration II shown in **Figure 8**).

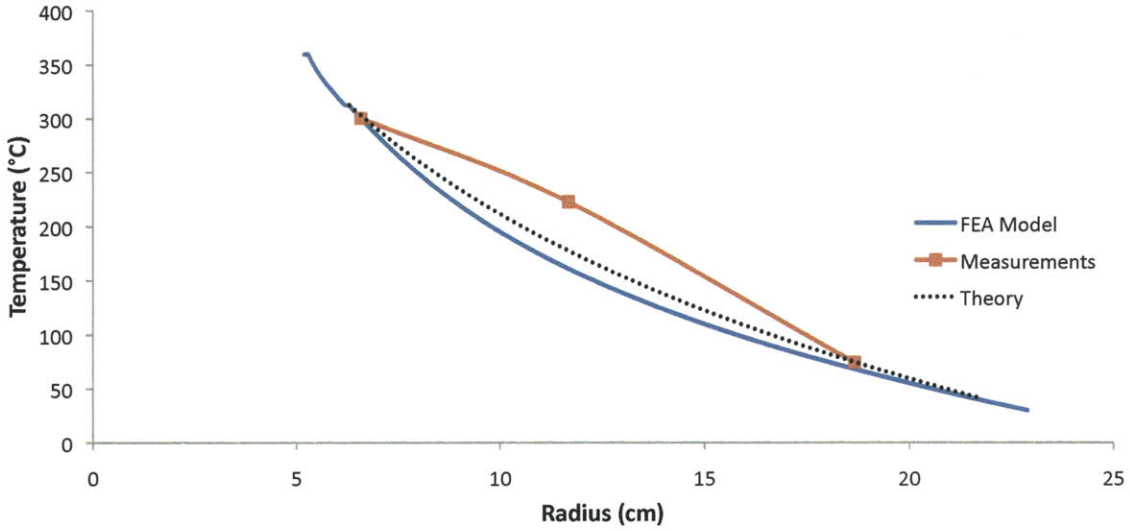

Figure 35: Radial temperature gradient averaged over six data samples. The standard deviation for data is below 6.5. The high temperature sheeting insulation was used in the radial direction.[25]

In order to determine if the high mid insulation temperature is due to the energy deposited over the insulation going beyond the calculated penetration depth, a layer of high temperature Zircar alumina insulation was placed above the insulation region, see **Figure 36**. The experimental setup is configuration II as shown in **Figure 8**.

[25] Updated 20100811 from MediumHX data collection v2

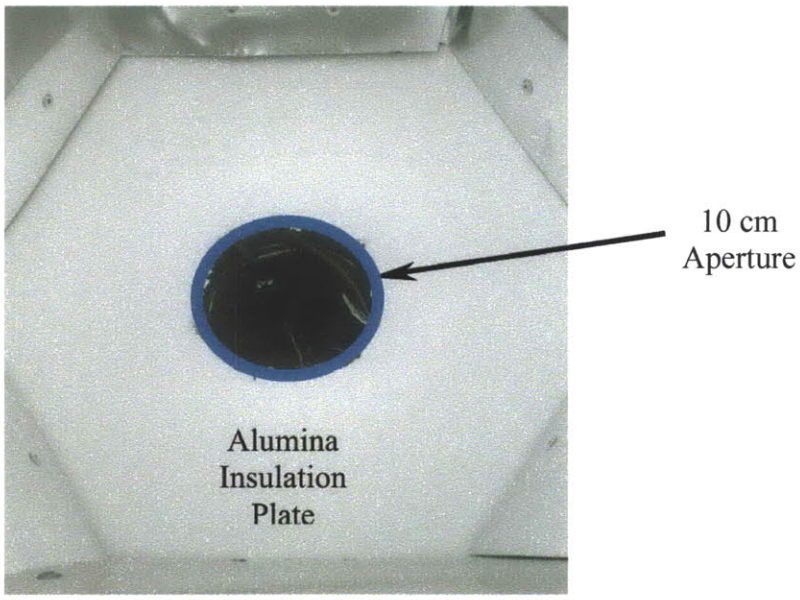

Figure 36: Top view of *P-II* with a high temperature 1/4 inch alumina insulation plate with a 10 cm diameter aperture. The system is setup in configuration II as shown in **Figure 8**. The alumina insulation plate sheet is used to reduce the energy deposited on the sheeting insulation (radial direction) to measure the effect on the radial temperature measurements.

The radial temperature measurements, shown in **Figure 37**, have the same high temperature measurements in the middle of the insulation. Therefore, the high temperatures in the insulation are not caused by the energy deposited onto the insulation by the simulator.

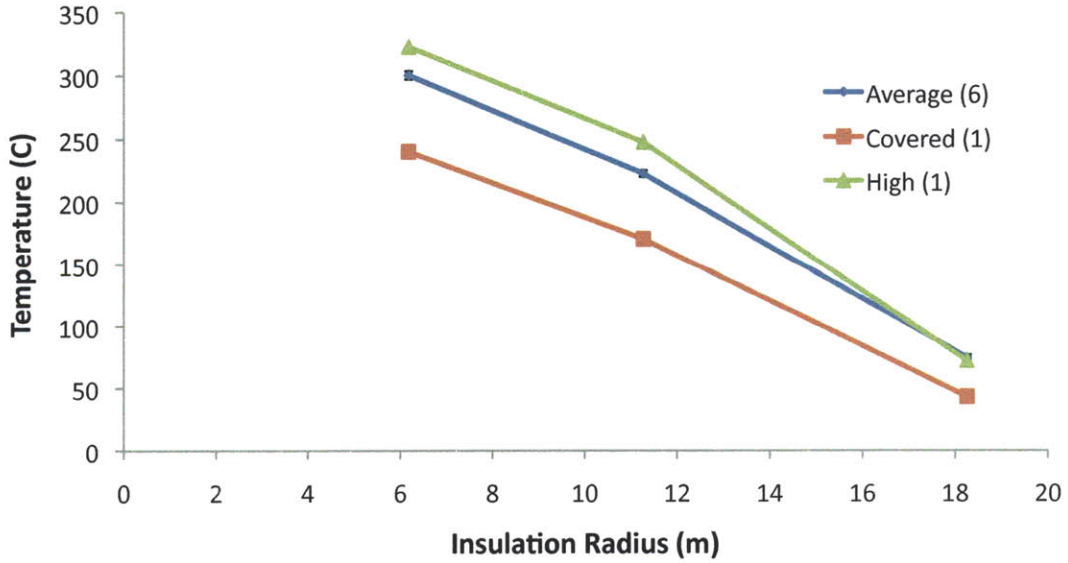

Figure 37: Insulation temperature measurements under different configurations. "Covered" refers to having a sheet of high temperature ceramic over the insulation (configuration II). "Average" data collected for heat removal, had small gaps between HX assembly and concentrator allowing for cold air to drafted into the container increasing the heat net loss. "High" refers to a configuration where there are no small gaps between the HX assembly and concentrator.

6.3.2. Energy Harvesting

Figure 38 shows the average and instantaneous extracted power for *P-II*. The bulk temperature of the salt reached temperatures as high as 367° C.

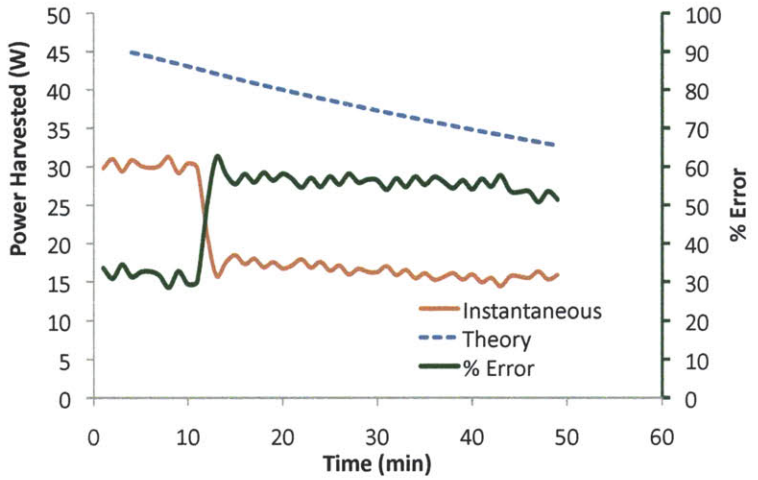

Figure 38: Theoretical and instantaneous power harvested from *P-II* with 2.32 kg of molten salt. The salt temperature goes from 367 to 275° C for the duration of extraction. Average power extracted is 19.5 W for 48 minutes. The drop in temperature is expected to a displacement of the exit thermocouple measuring the air flow temperature. The flow configuration is from bottom to top with the lights off and the top uncovered.

6.3.3. Molten Salt Temperature Gradient

The molten salt reaches almost a uniform temperature gradient through out the vessel, as shown in **Figure 39**. From the lowest point energy point to the center point the difference is less than four degrees Celsius at steady state. A uniform temperature demonstrates that there are no significant internal temperature gradients.

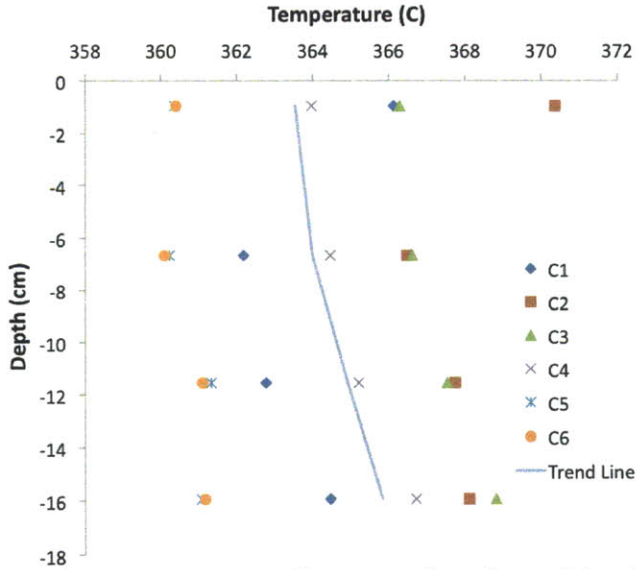

Figure 39: Molten salt temperature gradient as a function of depth below the salt surface (y=0) All of the data collected in the center of the container. *"C"* refers to the data collection. The trend line shows a uniform temperature versus depth.

6.3.4. Thermal: Casing Exterior Image

Figure 40 shows thermal images of the outside of the insulation revealing thermal gaps in the insulation leading to additional heat losses.

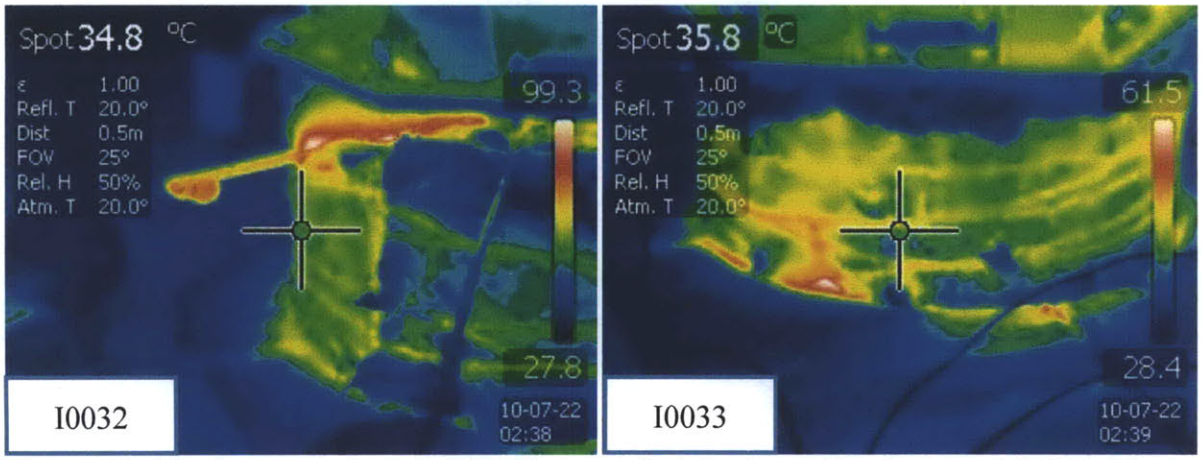

Figure 40: The image on the left (I0032) shows that the insulation is around 35° C. The image on the right (I0033) shows a similar exterior temperature of around 36° C (assuming emissivity of one, relative humidity of 50 %, and ambient temperature of 20° C). The air flow temperature may also be lower than theory since the stainless steel tubing is not insulated. The losses can be calculated for the region given the wall temperature, length, and exit temperature, see **Table 9**. The horizontal lines across the insulation are steel wires used to hold the rolled insulation as a cylinder.

The heat loss through the exposed tubing is in the order of 2 to 3 watts, as shown in **Table 9**. The drop in the temperature ratio is eight percent. *P-III* should have the tubing section insulated.

Table 9: Calculate heat loss through exposed tubing is in the order of 2 to 3 watts. Items in **black bold** are inputs, and **red bold** are outputs.

Objective: Calculate heat removal for P-II		
		$R_{tot-tube} = \frac{1}{h_{in} \cdot 2\pi \cdot r_1 \cdot L} + \frac{\ln(r_2/r_1)}{2\pi \cdot k_{pipe} \cdot L}$
r_1 = 0.00483 m **r_2 = 0.00635 m**	**L = 0.38 m**	**h_{in} = 33.3 W/(m²*K)** **k_{tube}=16.2 W/(m*K)**
$R_{tot-tube}$ = 86.7 K/W		
C_P = 1013 J/(kg*K)	**$\dot{m}$ = 10 SLPM** **$\dot{m}_{150C}$ = 1.4x10⁻⁴ kg/sec**	$\frac{T_{c,i} - T_{wall}}{T_{c,o} - T_{wall}} = \exp\left(\frac{-1}{\dot{m} \cdot c_p \cdot R_{tot-tube}}\right)$
$\Delta T_i / \Delta T_o$ = 0.92		
T_{wall} = 60° C	**$T_{c,o}$ = 240° C**	**$T_{c,o}$ = 225.6**
		$Q_P' = \dot{m} \cdot c_p \cdot (T_{b,out} - T_{b,in})$
		$\Delta Q'$ = 2-3W

6.3.5. Thermal Flow Measurements

In order to validate the flow measurements of the k-thermocouple, thermal images where taken of the region of interest. **Figure 41** shows the exit temperature k-thermocouple towards the end of an extraction run.

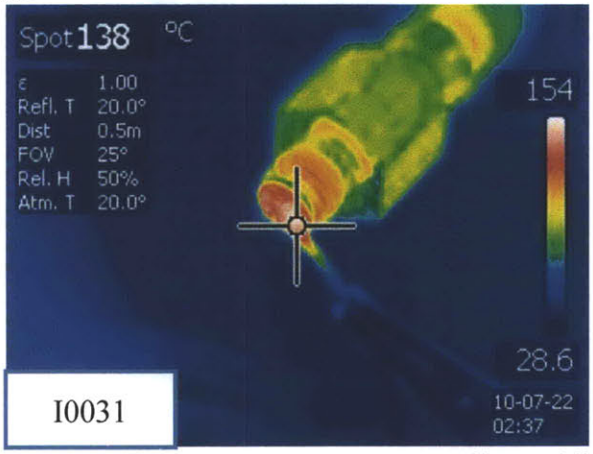

Figure 41: Image of the hot air flow measurements revealing additional energy lost to the environment. The next model will require that the tubing also be insulated in order to minimize heat loss.

6.3.6. Temperature Depth Measurements over Time

Figure 42, the temperature at different depths for *P-II* in configuration III with no extraction, shows the uniform temperature drop with depth through out time. Notice that over the depth of 16 cm the salt temperature varies by at most two degrees Celsius.

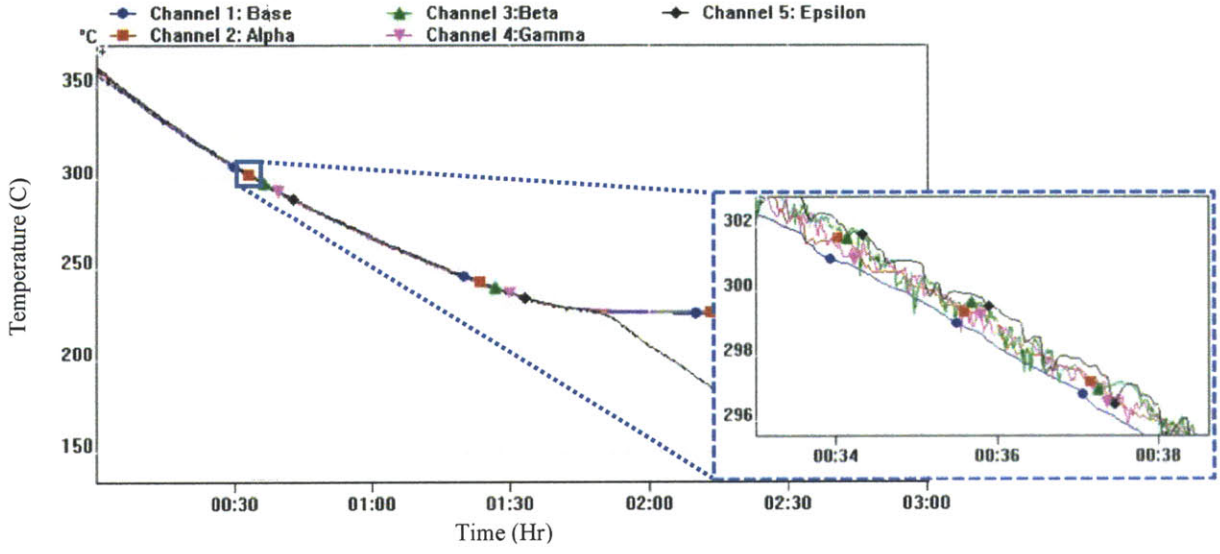

Figure 42: P-II Depth temperature as function of time under configuration III with no heat extraction thermal losses. All measurements are at the center of the molten bath unless otherwise stated. Base (r = 3 cm, depth 16.7 cm), Alpha (depth 15.9 cm), Beta (depth 11.6 cm), Gamma (depth 6.7 cm), and Epsilon (depth 1 cm). Depth is measured from the surface of the molten salt.

6.3.7. P-II Heat Loss Model Validation

Figure 43 compares the calculated (theory) bath bulk temperature as a function of time and to open surface data set in configuration III with no heat extraction.

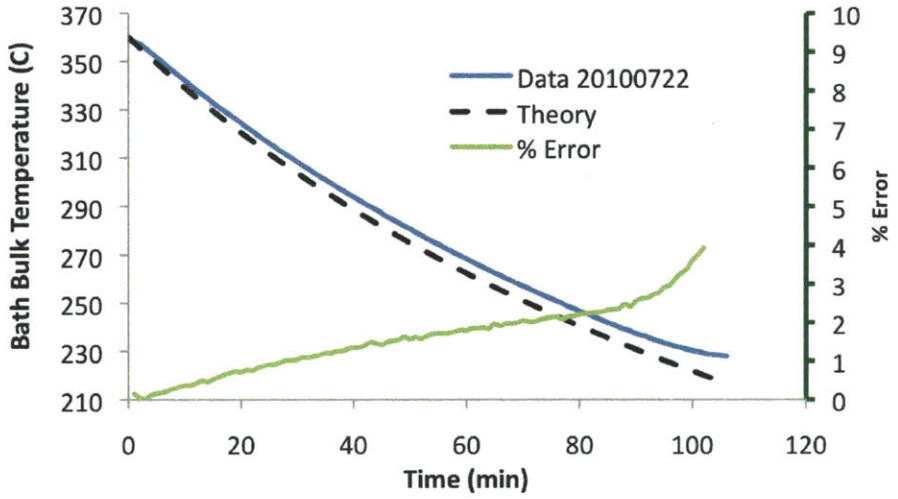

Figure 43: Comparison between theoretical bath bulk temperature to measured data (20100722) over time for *P-II*. The bulk temperature calculation is less than five percent of the measured data.

The maximum calculated heat loss for *P-II* is 126 W when the bath bulk temperature is 360° C. Over time the calculated heat loss decreases as the temperature of the bath decreases. **Figure 44** shows that the heat loss calculations for the molten salt are accurate. The theoretical calculated instantaneous heat loss matches the heat loss over time for the measured data.

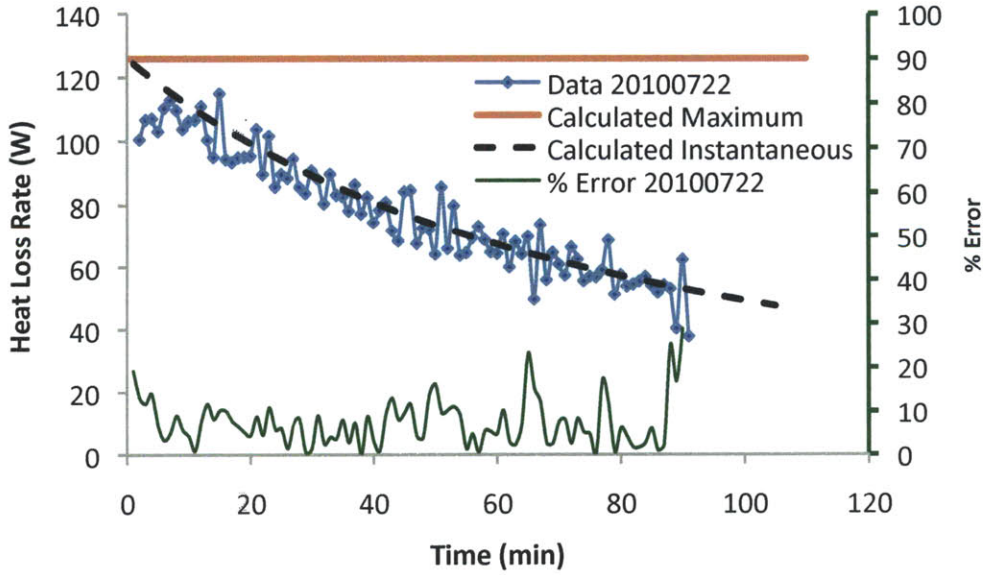

Figure 44: P-II Heat loss rate in configuration III with no extraction. The purpose is to verify that the calculated losses are correct. The heat loss for data 20100722 is obtained by finding the change in energy over time. Using welded bead k-thermocouples reduced the errors in heat loss as experienced in *P-I*. The percent error is less than thirty for the first 90 minutes.

6.3.8. Molten Salt Surface Convection

A series of time-lapse photos were taken of the top surface of the second prototype. **Table 10** shows the time photos taken around twenty seconds apart. Convection cells in the salt are evident from the thermal images of the salt. Visual inspection of the molten bath shows particles in the salt moving in convection patterns.

Table 10: Prototype two molten salt convection. Images 0043 thru 0057 were taken in about a three minute time interval

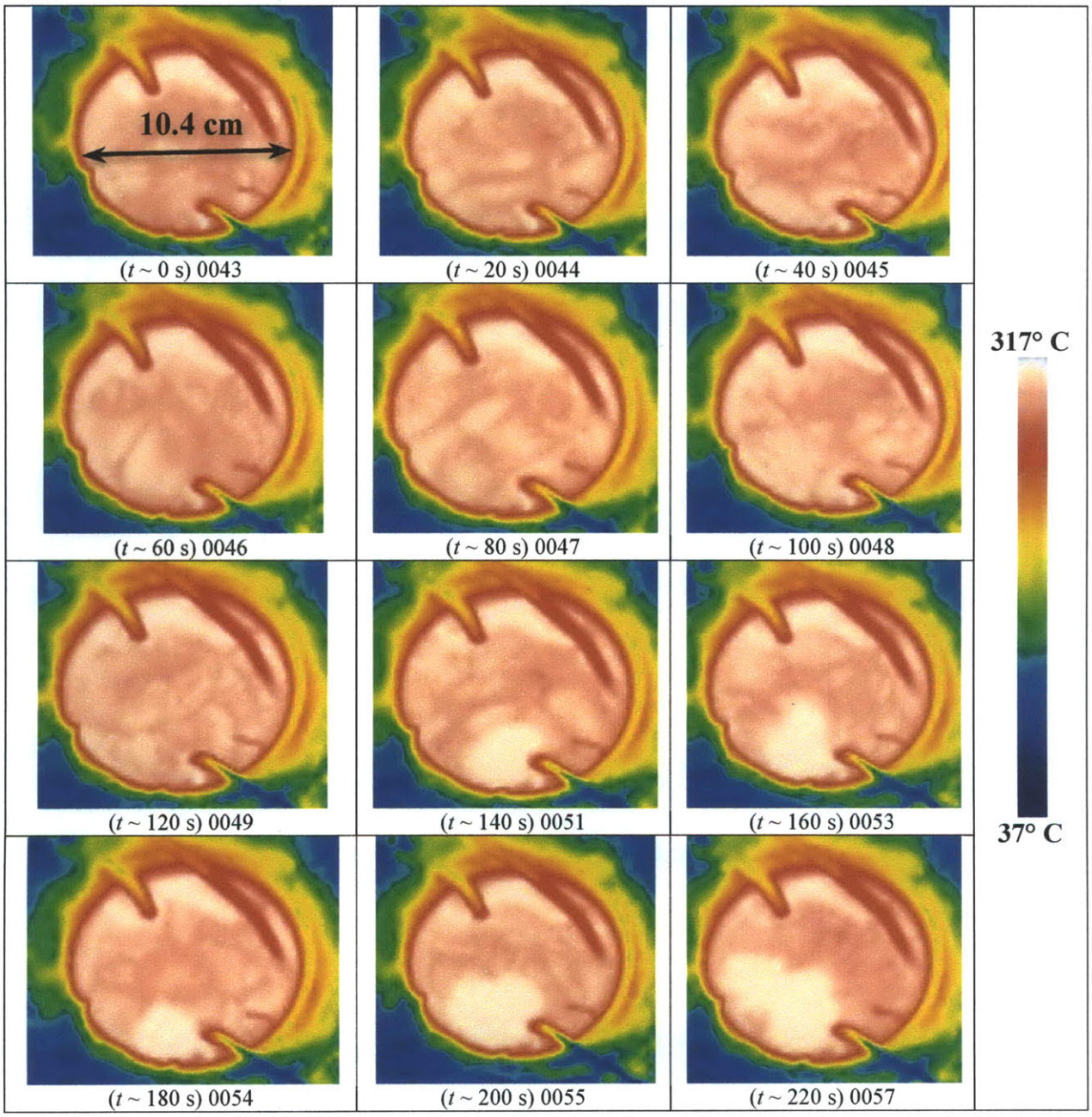

6.4. Results

The five objectives of the second prototype were met: 1) increase thermal mass, 2) find the steady state temperature gradient of the salt, 3) measure the insulation temperature gradient, 4) heat removal time longevity, and 5) salt convection. The thermal mass was increased to 2.2 kg (~ 4X previous prototype) and was melted with the solar simulator. The steady state temperature gradient in the salt proved to be only on average 4° C from the center top surface measurement to the bottom outer radius measurement. The time to reach ninety of the steady state is 6 hours 32 minutes with configuration I from a complete solid block at room temperature, without the addition of spheres[26]. The time to reach ninety percent of steady state (367° C) from melted (228° C) is around 3.8 hours[27]. The discharge time under configuration III from steady state temperature is one hour forty five minutes to go from 360 to 228° C, as shown in **Figure 42**. The duration of the heat extraction increased to forty three minutes for a bulk temperature change from 360 to 275° C. Salt convection was evident from visual inspection and thermal images of the surface captured the temperature changes induced by the convection cells.

The heat loss model was validated with experimental data. The calculated heat loss rate matches the measured experimental data with at most 29 % error, on average the error is ~7 %. Therefore, the approximation of the surface convection losses at the surface of the molten salt bath is an accurate model. The molten salt bulk temperature model has at most a 5 % error, and 1.4 % on average.

Figure 37 shows how the FEA model of the insulation compares to the measured values. The discrepancy between the model and data is attributed to the deterioration of the insulation near the vessel wall, as shown in **Figure 45**. The penetration depth is not large enough to affect the measurements. The insulation properties may also vary with temperature. An important item to note is that the insulation binds to the stainless steel wall. There is also deterioration to the heat exchanger coil, as shown in **Figure 45**. Since the radial conduction is not a predominant mode of heat loss the effect on the model is minimal, as shown from the heat loss rate comparison in **Figure 44**.

Figure 45: On the left, darkened stainless steel vessel and coiled copper tube heat exchanger after a 3-4 hour single run. On the right, insulation degradation close to the stainless steel container. The blackened copper layer can flake off thus releasing particulates into the molten salt.

[26] P-II Data 20100720-1519
[27] P-II Data 20100721-0029

6.5. Discussion

The heat exchanger air flow temperature measurements were found to be once again very sensitivity to position along the center of the exit flow tube. The second item that merits discussion is a proposed Particle Image Velocimetry (PIV) system to measure the convection cells inside of the medium. Preliminary tests were performed as a proof of concept prototype.

6.5.1. HX Air Flow Temperature Measurements

The temperature measurements are sensitive to misalignments ζ, from the center of the outflow tube stream. The welded bead can not touch the wall of the tubing or be near the wall. When the welded bead is near the wall the temperature measurements can be at least 20° C lower than the centered temperature measurement.

6.5.2. High Temperature PIV Proposal

A basic PIV uses a laser with a series of optics to illuminate a laser plane on a fluid medium. The light bounces of particles in the fluid medium that were dispersed prior to the test (seeding). Normal to the laser plane a camera records at high frame rates the illuminated particles and their location over time. The velocity profile of the particles is obtained in the post-processing state were the particle displacement between consecutive frames is used to calculate the velocity of the particles.

The objective behind a high temperature PIV system is to capture the velocity profile of particles inside molten salt bath exceeding temperatures 350° C. Existing PIV systems are not intended for high temperature applications. Changing the materials/parameters of the molten salt geometry can change the thermodynamics of the system. Therefore, conventional PIV systems can not be used for the high temperature convection cell measurements.

A simple PIV design consists of three items: 1) laser, 2) seeded medium, and 3) high speed camera. The proposed high temperature PIV measurement technique aims to minimize: biological hazards, and cost. Most PIV systems use class 3B or class 4 lasers, which can be dangerous with power ratings of 5-500mW and greater than 500mW respectively. Independent of the cost of the unit is the safety concerns to the user. Class 3B lasers can cause damage to the eye from a direct exposure. Class 4 lasers can be hazardous from direct exposure and from reflected rays. The proposed design uses class 3R (5mW) lasers pointers, which pose a lower biological risk to the user. The optics consists of a cylindrical plastic tube filled with water that takes a laser beam and modifies it to a laser plane.

The molten salt does not require seeding, like conventional PIV systems. There are particles moving in the melted salt container and they can be viewed by the naked eye. From visual inspection the particles are moving at a rate that appears to be between 1 to 3 mm/sec. The trajectory of the particles is not random. Visual inspection shows convection cell patterns. In the center of the container there is a plum that is moving hot material towards the surface and at the edges of the container there is a current that allows salt cooled by heat transfer to the HX and container wall to sink to the bottom.

The high operating temperatures and the desired thermodynamics require that the laser plane be projected from the top of the container to maintain a vertical plane. The imaging also has to be done from the top of the container to preserve the thermal properties of the container. **Figure 46** shows a proposed setup for a high temperature PIV system to capture the movement

of the convective cells. The camera is placed at an angle to the top of the bath and the image is later corrected for the Snells law and the angle distortion to capture the velocity of the particles.

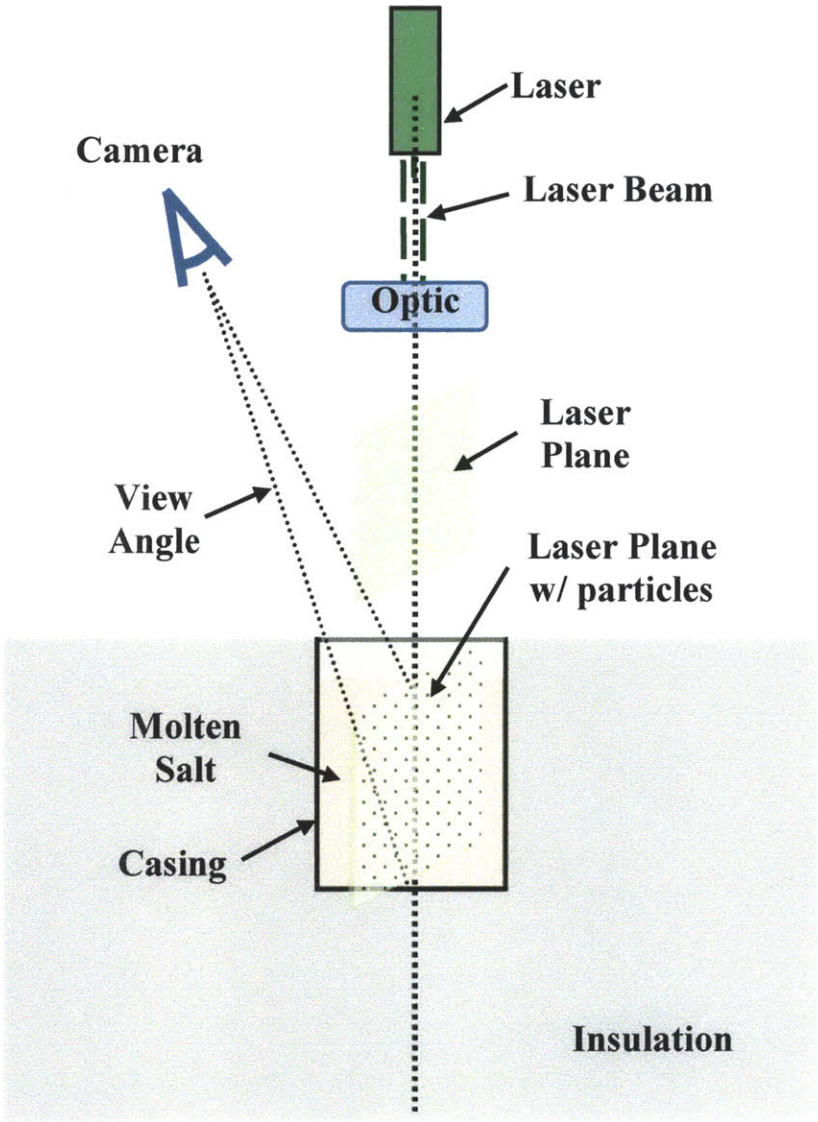

Figure 46: PIV schematic layout for capturing the convection cells inside the molten salt container. The medium, i.e. molten salt, does not require seeding as there are already particulates (impurities) inside the salt. The optics required is a simple cylinder that can turn a laser beam into a laser plane. The laser beam is converted into a plane using a polypropylene conical centrifuge tube filled with water. A green or a red laser pointer can be used to illuminate the small prototype model. The view angle does not include the angle of refraction.

The images obtained using the PIV system can be reduced using an analysis package like LabVIEW or MATLAB. The velocity profile can be determined by measuring changes between frames and the frame rate. The images can be calibrated to account for the angle of refraction.

6.5.3. Preliminary PIV Proof of Concept

Prior to making a significant time investment, it was necessary to prove the basic concept with a 5mW laser pointer. A preliminary test showed that a green laser pointer coupled with a cylinder filled with water could produce a laser plane that could easily penetrate over ten centimeters of water. Both red laser and green laser can penetrate the full depth of the molten salt container.

Figure 47 shows a green laser plane illuminating particles inside a container of molten salt at 370° C. The molten salt bath has not been seeded with particles that reflect the laser. The particles illuminated are native impurities in the molten salt.

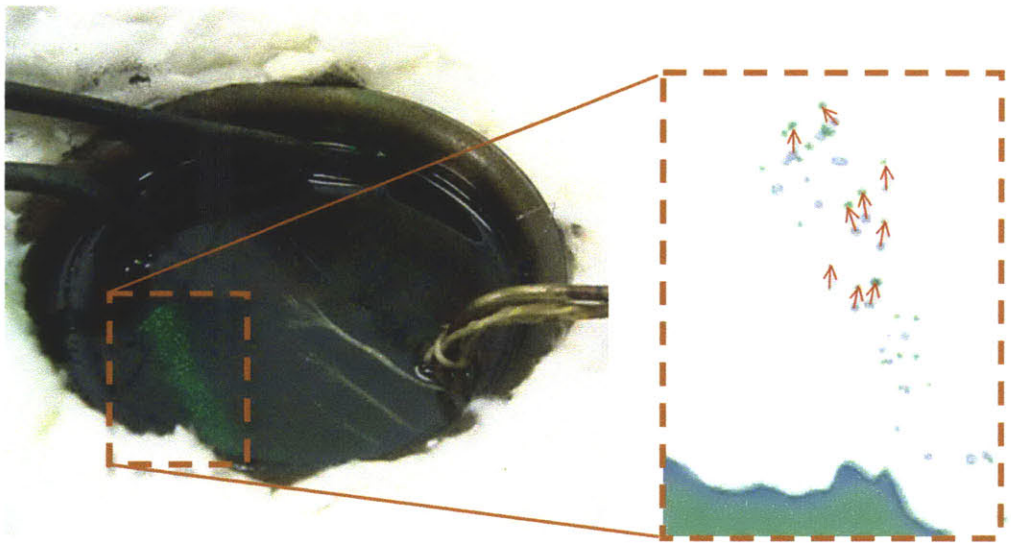

Figure 47: PIV proof of concept for high temperature molten salt. Notice that there are particles in the molten salt that reflect light. The native particles can be used to determine convection cells in the container. The image on the right is composed of two consecutive time frames (blue and green). The arrows (red) show particles from the blue frame that shifted in the green frame. The particles that are traced between the two frames can be used to find the velocity given the frame rate.

7. 10.5 kg Coiled Tube Heat Exchanger

P-III can hold approximately 10 kg of salt. The objectives of the *P-III* are the following: 1) melt salt with solar simulator, 2) radial temperature gradient, 3) steady state salt temperature gradient, 4) heat removal longevity, and 5) convection characterization.

7.1. Design

P-III also consists of a 1/4 inch copper tube (122) coiled tube heat exchanger. The heat exchanger implemented is placed inside salt bath. A gap is left between the container wall coiled tube heat exchanger to allow for a more uniform temperature surrounding the heat exchanger wall.

The container for the bath is a stainless steel cooking ware. The container was chosen to minimize the complexity of manufacturing while maintaining the integrity of the experiment. The interior diameter of the container is 20 cm (7.875 in), with a wall thickness of 0.76 mm (0.03 in). The total depth of the container is 17.8 cm (7 in). The bottom thickness of the container is 4.8 mm (3/16 in). **Figure 48** show the container with the coiled tube heat exchanger inside. The details of the coiled tube heat exchanger can be found in the next section.

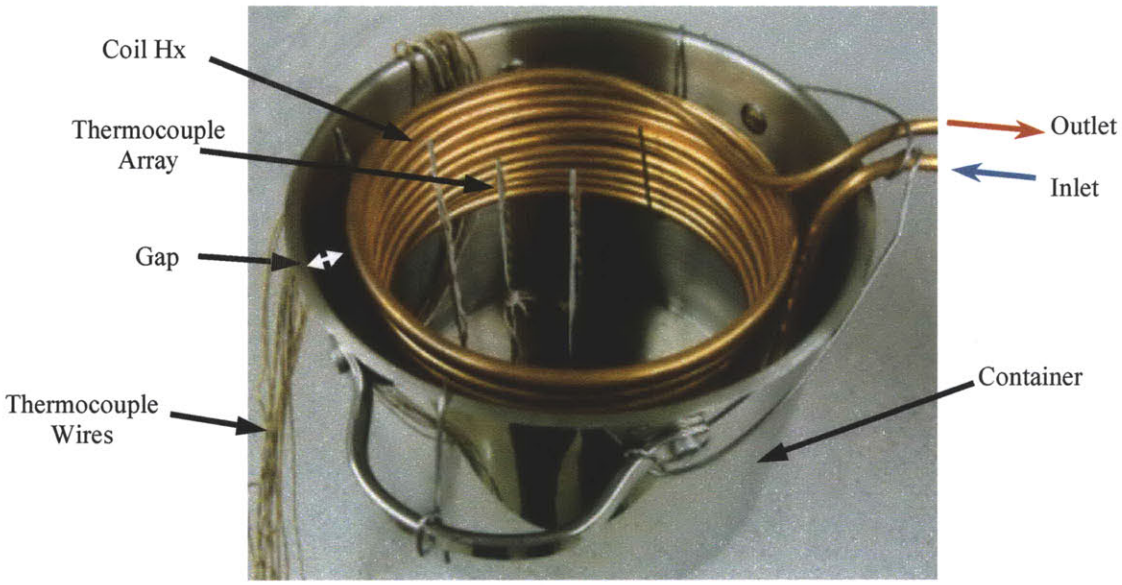

Figure 48: *P-III* copper coiled tube heat exchanger in stainless steel salt container without insulation showing the gap left between the Hx and the casing wall, inlet and outlet, and setup.

7.1.1. Coiled Tube Heat Exchanger

The coil heat exchanger consists of 1/4 inch copper (alloy 122) tubing shaped into an ten turn coil with an outer diameter of 17.1 cm (6.75 in). The tubing dimensions are the same as that in *P-II* and *P-I*. The total contact length of the copper tubing with the salt bath is 5.2 meters. Both ends of the heat exchanger have Yor-Lok fittings for 1/4 inch tubing. **Figure 50** shows the model of the coiled tube heat exchanger, with an array of k-thermocouple.

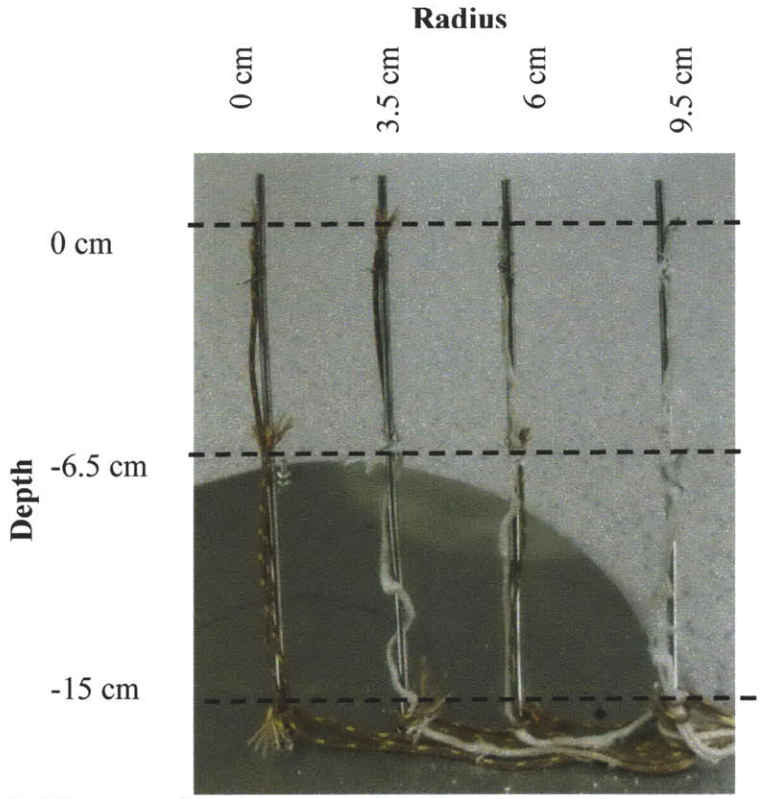

Figure 49: *P-III* array of k-thermocouples for measuring a cross section of the molten salt temperature.

7.1.2. *P-III* Schematic Layout

Figure 50 shows a schematic layout for *P-III.*

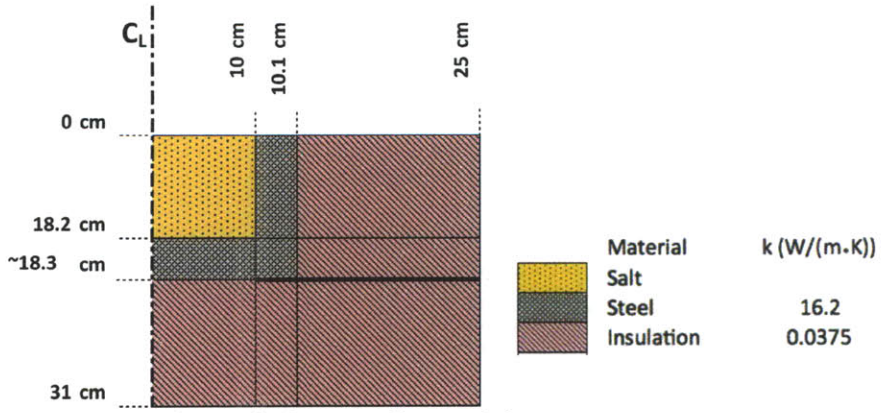

Figure 50: *P-III* schematic layout of materials.

7.1.3. Energy Deposited

The diameter of the top surface is 20 cm; therefore, the top cross sectional area of the container is 3.14×10^{-2} m^2. Assuming the solar simulator is delivering 50 kW/m^2, then the energy deposited on the pond is 1.57 kW.

7.1.4. Initial Losses

There are four main types of losses: 1) radial conduction, 2) bottom surface conduction, 3) radiation losses, and 4) surface convection losses. **Table 11** shows the loss calculations. The dominant losses are radiation losses and natural convection losses 339.7 w and 133.3 w respectively. The radial losses are estimated at 17.2 W. The heat loss through the bottom of the container due to conduction is 3.5 W. The radiation losses from the top are 339.7 W. The losses are an upper bound estimates.

Table 11: *P-III* initial thermal losses. The sum of the initial thermal losses is at most 494 watts.

Objective: Calculate Thermal Losses				
Radial Conduction				
$R_{tot} = \frac{\ln(r_2/r_1)}{2\pi \cdot k_{case} \cdot H} + \frac{\ln(r_3/r_2)}{2\pi \cdot k_{Insulation} \cdot H} + \frac{1}{h_{ext} \cdot 2\pi \cdot r_3 \cdot H}$				
$r_1 = 10$ cm	$r_2 = 10.07$ cm	$h \sim 10$ W/(m*K)	$k_{12} = 16.2$ W/(m^2*K) @ 350	$T_{1,Salt} = 395°$ C
$r_3 = 25$ cm	$H = 18.2$ cm		$k_{23} = 0.038$ W/(m^2*K)	$T_{3,Room} = 30°$ C
$R_{tot} \sim 21$ K/W				
				$Q'_{Radial} \sim 17.2$ W
Axial Conduction				
$R_{Bottom} = \frac{t_{case}}{k_{case} \cdot A} + \frac{t_{insulation}}{k_{insulation} \cdot A} + \frac{1}{h_{Bottom} \cdot A}$				
$t_{case} = 4.8$ mm	$r = 10$ cm	$k_{stainless\ steel} = 16.2$ W/(m^2*K)	$T_1 = 395°$ C	
$t_{insulation} = 12.7$ cm		$k_{insulation} = 0.038$ W/(m^2*K)	$T_2 = 30°$ C	
$R_{Bottom} \sim 105$ K/W				
				$Q'_{Bottom} \sim 3.5$ W
Surface Radiation				
$Q'_{Radiation} = A \cdot \gamma \cdot \sigma \cdot (T_{salt}^4 - T_{room}^4)$				
$A_T = 3.14 \times 10^{-2}$ m^2	$T_{room} = 30°$ C	$T_{salt} = 395°$ C	$\sigma = 5.670 \times 10^{-8}$ J/(K^4*m^2*s)	
				$Q'_{Radiation} \sim 339.7$ W
Surface Convection				
$Ra_{lc} = \frac{\beta_{air} \cdot (T_{salt} - T_{room}) \cdot g \cdot l_c^3}{\nu_{air} \cdot \alpha_{air}}$				
$\beta_{air} = 3.55 \times 10^{-3}$ K^{-1}	$g = 9.8$ m/s^2	$T_{room} = 30°$ C	$l_c = 10.4$ cm	
$\nu_{air} = 14.2 \times 10^{-6}$ m^2/s	$\alpha_{air} = 2.25 \times 10^{-5}$ m^2/s	$T_{salt} = 395°$ C		
$Ra_{lc} = 2.61 \times 10^8$				
Criteria: $2x10^7 < Ra_{lc} < 3x10^{10}$ $\Rightarrow$ $Nu = \frac{h_{surf} \cdot l_c}{k_{air}}$ $\Rightarrow$ $Q'_{surf} = h_{surf} \cdot A_T \cdot (T_{salt} - T_{room})$ $\overline{Nu_L} = 0.14 \cdot Ra_{lc}^{1/3}$				
$Nu_{Lc} \approx 89$	given $k_{air} = 0.0264$ W/(m*K)	$h_{surf} \approx 11.8$ W/(m^2*K)		
				$Q'_{Surf} \sim 133.3$ W
				Total Heat Loss Rate: 493.7 Watts

7.1.5. Heat Extraction Calculation

The convection coefficient for the airflow inside the coil tubing was calculated at 33 W/(m*K) for the previous prototypes. Since the coil tubing remains unchanged then the convection coefficient is expected to also remain the same. In order to see how a convection coefficient affects the maximum heat removal, two additional convection coefficients were used of 20 and 50 W/(m*K), with respective heat removal of 43 watts and 45.3 watts. Therefore a small error in the convection coefficient results in an even small error in the heat removal. The calculated maximum heat removal from *P-III* is 44.5 watts, as shown in **Table 12**.

Table 12: Heat removal for *P-III*.

Objective: Calculate heat removal for *P-III*		
		$R_{tot-tube} = \frac{1}{h_{in} \cdot 2\pi \cdot r_1 \cdot L} + \frac{\ln(r_2/r_1)}{2\pi \cdot k_{pipe} \cdot L}$
r_1 = 0.00483 m **r_2 = 0.00635 m**	**L = 5.2 m**	**h_{in} = 33.8 W/(m²*K)** **k_{tube}=380 W/(m*K).**
$R_{tot-tube}$ =0.19 K/W		
c_P = 1013 J/(kg*K) **ΔT_{in} = 360° C**	**$\dot{m}$ = 10 SLPM** **$\dot{m}_{150C}$ = 1.4x10⁻⁴ kg/sec**	$\frac{\Delta T_{out}}{\Delta T_{in}} = \exp\left(\frac{-\dot{m} \cdot c_p}{h_{in} \cdot 2\pi \cdot r_1 \cdot L}\right)$
ΔT_{out} = 324° C		
		$Q'_P = \dot{m} \cdot c_p \cdot (T_{b,out} - T_{b,in})$ **Q'_P = 45.5 W**

7.1.6. Capped Radiation and Surface Losses

The open surface is capped to reduce the radiation and convective losses at the surface of the molten salt. The cap consists of an 1.5 inch thick rigid alumina insulation. The experimental setup is that shown in configuration IV in **Figure 9**. There is an air gap between the molten salt surface and the insulation interior surface. Preliminary experiments showed that volume of air right on top of the salt stays at about ten degrees less than the top surface of the salt. The observation from the temperature measurements is used to calculate the radiation and convection losses in the capped configuration. Capping the molten bath results in the following loss reductions: 1) radiation from ~340 watts to ~41 watts, and 2) convective surface from ~134 watts to 7.1 watts. **Table 13** shows the detail calculation for the capped radiation and surface convection losses.

Table 13: Capped Radiation and convection losses for *P-III*.

***Radial Conduction + Axial Conduction* (Table 11)** — $Q'_{Radial+Axial} = 20.1\ W$
Surface Radiation
$$Q'_{Radiation} = A \cdot \gamma \cdot \sigma \cdot (T_{salt}^4 - T_{amb}^4)$$
$A_T = 3.14 \times 10^{-2}\ m^2$ $T_{amb} = Tsalt - 20°\ C$ $T_{salt} = 395°\ C$ $\sigma = 5.670 \times 10^{-8}\ J/(K^4 * m^2 * s)$
$Q'_{Radiation} = 40.6\ W$
Conduction Through Cap
$$R_{cap} = \frac{t_{cap}}{k_{cap} \cdot A_c} + \frac{1}{h_{cap-surf} \cdot A}$$
$t_{cap} = 3.8\ cm$ $k_{cap} = 0.18\ W/(m*K)$ $h_{cap\text{-}surf} = 10\ W/(m^2*K)$
$R_{cap} = 9.9\ K/W$
$$Q'_{Cap} = \frac{(T_{room} - T_{amb})}{R_{cap}}$$
$T_{amb} = T_{salt} - 20°\ C$ $T_{room} = 30°\ C$
$Q'_{Cap} = 32.8\ W$
Surface Convection
$$Ra_{lc} = \frac{\beta_{air} \cdot (T_{salt} - T_{amb}) \cdot g \cdot l_c^3}{\nu_{air} \cdot \alpha_{air}}$$
$\beta_{air} = 3.55 \times 10^{-3}\ K^{-1}$ $g = 9.8\ m/s^2$ $T_{amb} = 375°\ C$ $l_c = 10.4\ cm$ $\nu_{air} = 14.2 \times 10^{-6}\ m^2/s$ $\alpha_{air} = 8.35 \times 10^{-5}\ m^2/s$ $T_{salt} = 395°\ C$
$Ra_{lc} = 2.81 \times 10^8$
$Criteria: \quad 2x10^7 < Ra_{lc} < 3x10^{10} \Rightarrow \overline{Nu_L} = 0.14 \cdot Ra_{lc}^{1/3} \Rightarrow Nu = \frac{h_{surf} \cdot l_c}{k_{air}} \Rightarrow Q'_{surf} = h_{surf} \cdot A_T \cdot (T_{salt} - T_{amb})$
$Nu_{Lc} \approx 91.7$ given $k_{air} = 0.0513\ W/(m*K)$ $h_{surf} \approx 24.5\ W/(m^2*K)$
$Q'_{Surf} = 6\ W$
***Total Heat Loss Rate:* 99.5 Watts**

7.2. Data

7.2.1. Molten Salt temperature gradient

The twelve thermocouples placed inside of the molten salt bath are used to characterize any thermal gradient in the salt. The steady state thermal gradients in configuration I are plotted in **Figure 51**.

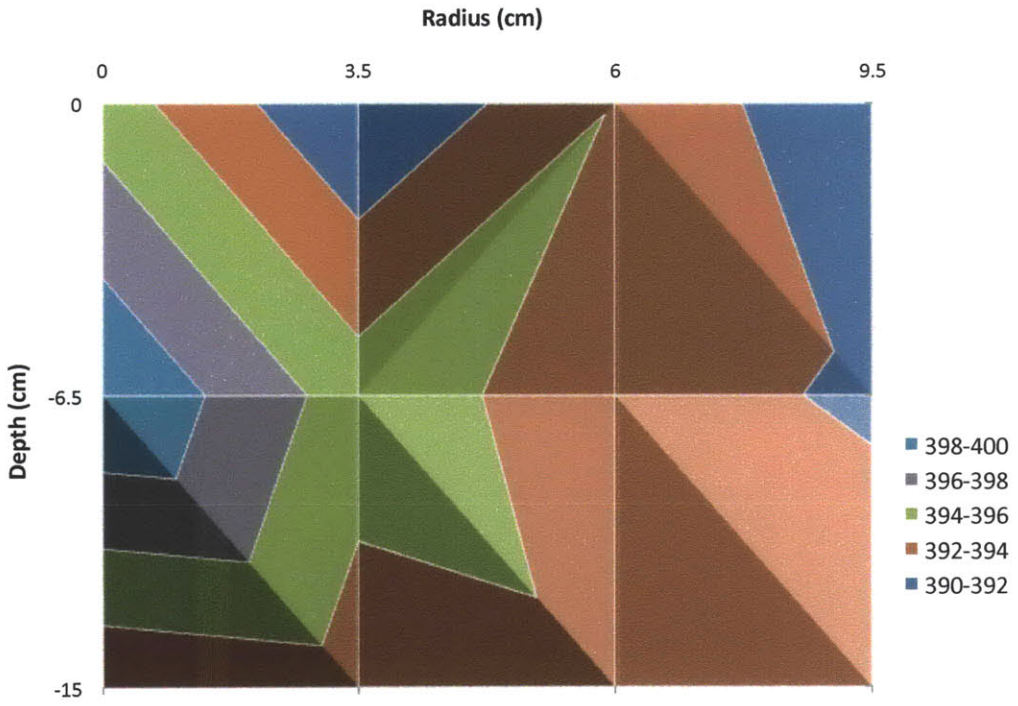

Figure 51: Radial temperature measurements for prototype three without a top insulation layer. The thermocouple located at (3.5,-15) failed, the plotted data point is the average of the two points that surround at it at the same depth. The image is not to scale.

7.2.2. Power Harvesting

The power harvesting duration from 390 to 275° C is 70 minutes for an open system in configuration III. **Figure 52** shows energy harvested for an open and capped system with the theoretical values. The cycling of the instantaneous power harvested is due to the cycling of the air pump. The open configuration lasts 45 minutes extracting 22 W to drop the bath bulk temperature from 330 to 275° C. The capped configuration lasts 123 minutes extracting 25 W to drop the same bulk temperature. The covered geometry consisting of an silica brick insulation block allows the same system to produce four times as long.

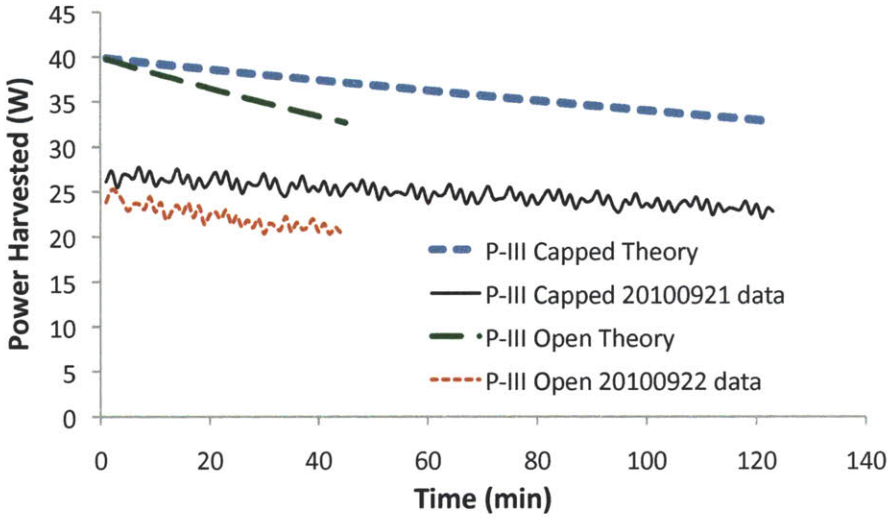

Figure 52: *P-III* power harvest for the open and capped surface compared to the theoretical values. The temperatures are plotted for bath bulk temperature change between 330 to 275° C. The cycling of the data is due to the pump cycle time. The maximum error in power harvested for the capped and open configuration are 42 % and 36 %, respectively.

7.2.3. Convection PIV

The proposed PIV detection system was also used with prototype three. One of the challenges faced with the third prototype is removing the contaminants that foam on top of the salt the first time that the salt is melted from pellets. However, the salt is almost clear to the eye after the contaminants have been removed by skimming the top once the salt is melted.

7.2.4. *P-III* Open Heat Loss Model Validation

Figure 53 compares the calculated (theory) bath bulk temperature as a function of time and to two open surface data sets in configuration III with no heat extraction for *P-III*.

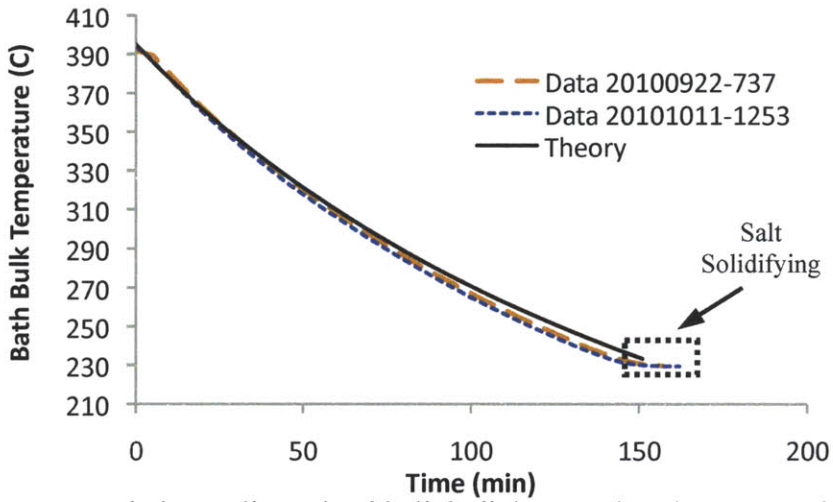

Figure 53: Comparison between theoretical bath bulk temperature to measured data (20100922-737 and 20101011-1253) over time for *P-III*.

The maximum calculated heat loss for *P-III* is 494 W when the bath bulk temperature is 395° C. Over time the calculated heat loss decreases as the temperature of the bath decreases. **Figure 54** shows that the heat loss calculations for the molten salt are accurate. The theoretical calculated instantaneous heat loss matches the heat loss over time for the measured data. The maximum error in the heat loss model is 25 percent.

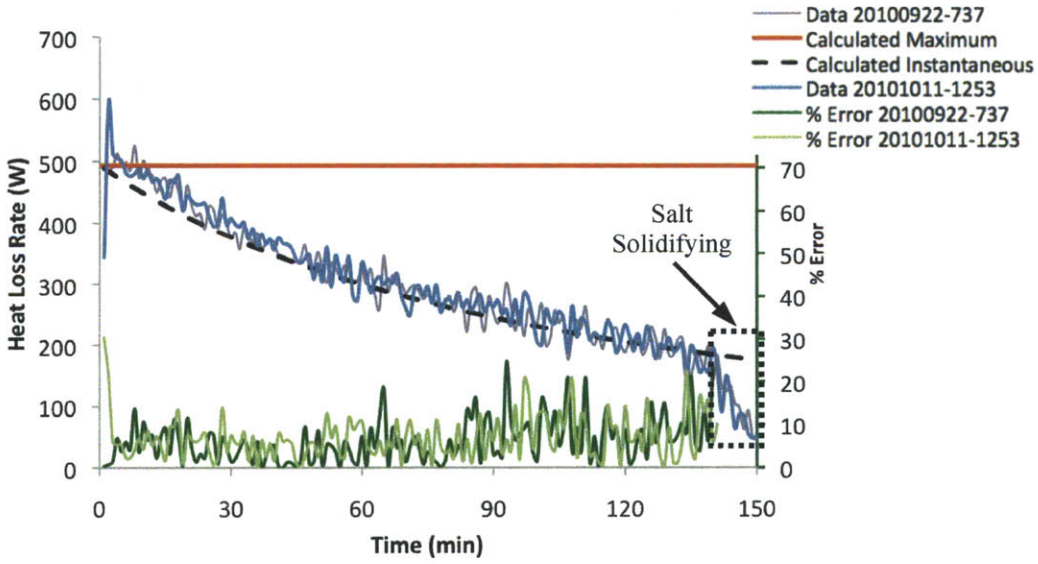

Figure 54: *P-III* Heat loss in configuration III with no extraction. The purpose is to verify that the calculated losses are correct. The heat loss rate for 20100922-737 and 20101011-1253 is obtained by finding the change in energy over time. Using welded bead k-thermocouples reduced the errors in heat loss as experienced in *P-I*.

7.2.5. *P-III* Closed Heat Loss Model Validation

Closing the container reduces the surface convection and radiation losses by a factor of 16 and 19 respectively. The calculated maximum heat loss for the capped configuration IV is 116 watts. **Figure 56** compares the heat loss model to measured data. The percentage error for the capped configuration for *P-III* is less than 30 percent.

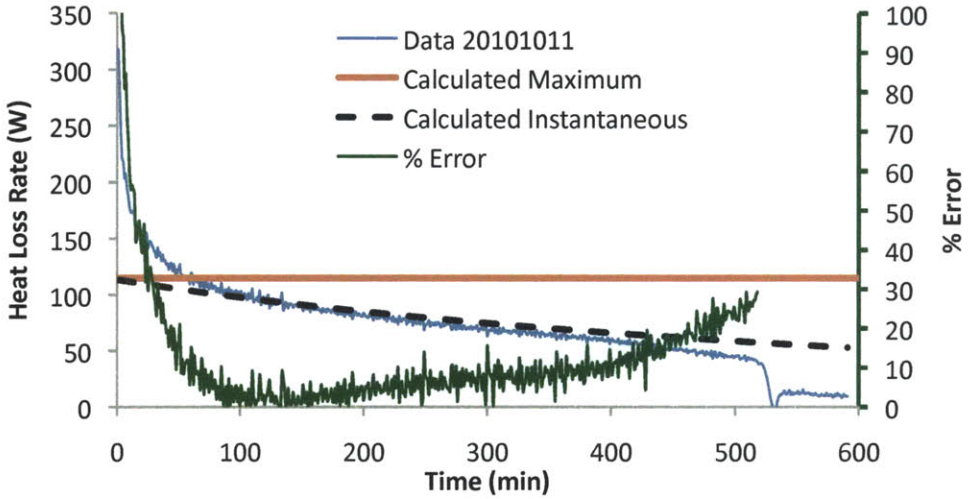

Figure 55: Capped configuration thermal losses calculation with percentage error from thermodynamic model. After reaching steady state the error is less than 30 percent. It takes about an hour to establish steady state.

7.3. Results

The molten salt bath reached steady state temperatures as high as 395° C. It takes 11.5 hours for a mass 10.5 kg of salt (no additives i.e. spheres etc.) to go from room temperature to 90 % of the steady state temperature. The time of extraction did not increase as high as expected for the volume of molten salt, attributed to the radiation losses from the open lid container. Adding a cap to the container increased the duration of extraction, the thermal losses due to surface convection and radiation where reduced by a factor of 16 and 19 respectively.

The center of the container was measured to be ten degrees higher than the outer radius in configuration I steady state. The temperature gradient is expected due to the radial heat loss. *P-III* contains well define convection cells that could be captured with a PIV or digital camera.

The thermal losses model was validated for the open configuration. The error for the losses in the opened configuration is less than 25 percent, while the error for the losses in the capped configuration is less than 30 percent after the system has reached steady state. The calculated bulk temperature matches the collected data.

8. Results

There were several trends observed comparing the three prototypes. **Table 14** shows a summary of the three prototypes and the parameter. As the diameter of the aperture increased the energy deposited on the salt increased thus allowing for higher steady state temperatures to be reached. With the increase in aperture size the thermal losses due to radiation and surface convection also increased. The heat extraction rate was kept constant in order to measure the length of extraction for a certain temperature range. Has expected the duration of extraction increases with the volume of molten salt. The duration of extraction for *P-III* did not increase significantly compared to *P-II* in the open configuration. Capping *P-III* led to a four-fold increase in the duration of extraction compared to the open *P-III* configuration.

Table 14: Prototype results comparison. Effectiveness is given for a system with the following configuration: lights off, bottom to top flow, and a flow rate of 9.5 SLPM.

	S. S. Temp (°C)	Max. Therm. Losses (W)	Max. Expected Heat Removal (W)	330° C to 275° C Heat Extraction (W)	330 - 275° C Duration (min)	Effectiveness
Prototype I Mass 0.5 kg	330	35	37.9	23	14	0.56
Prototype II Mass 2.20 kg	360	126	41.7	23	29	0.78
Prototype III Mass 10.5 kg	396	494	45.5	22	43	0.63
Prototype III Mass 10.5 kg Covered	397	49	45.5	25	123	0.68

Figure 56 shows the effectiveness of the heat exchanger as a function of flow rate, as calculated using Equation 9. The data collected from *P-II* shows how the effect of properly aligning the flow temperature k-thermocouple.

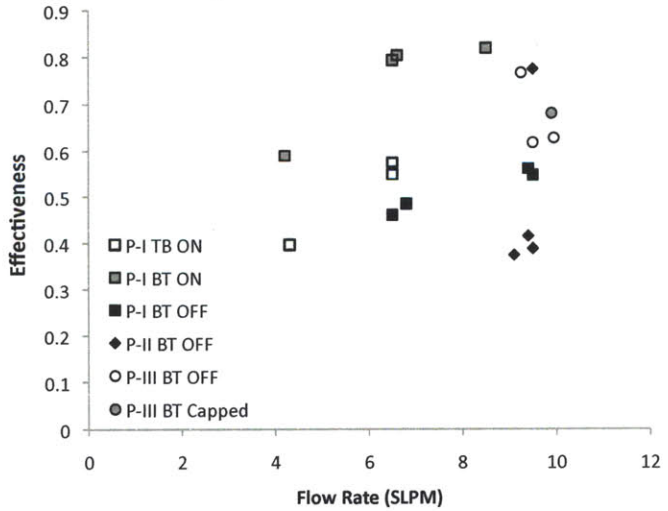

Figure 56: Flow rate (SLPM) versus effectiveness for all three prototypes. The first two letters refer to the prototype, followed by the flow configuration (TB and BT), and the solar concentrator lights status. The "Capped" status for *P-III* refers the lights off and an insulation lid on the container to reduce thermal losses.

The thermodynamic heat loss model was validated for all three prototypes. The error in the heat loss calculation is less than 30 percent. The heat loss model for *P-III* in the capped configuration was also validated.

Figure 57 shows the time to reach 90 percent of the steady state temperature versus the total mass of the reservoir. Additives such as spheres can be added to reduce the time to reach steady state temperature from a cold start.

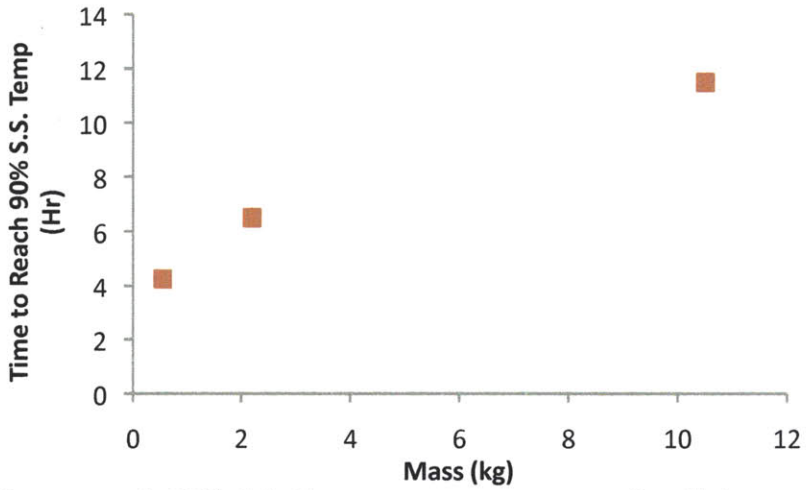

Figure 57: Time to reach 90% S.S. Temperature versus mass for all three prototypes from a solid block at room temperature

9.Conclusion

CSPonD has the potential to provide significant thermal energy storage for CSP systems. The coiled tube heat exchanger prototypes developed for harvesting energy from the molten salt were modeled, manufactured, and tested. The heat exchanger model is simplified to a tube with a constant wall temperature along its length. As heat is removed, the salt bulk temperature drops but the temperature along the tube length remains constant since the volumetric heat capacity for the molten salt is greater than that for the airflow. The power extraction model is within 46%, 42%, and 36% experimental values for prototypes I thru III respectively. The primary source of error for power extraction is the conduction through the stainless steel tubing after the heat exchanger leading out of the container assembly. Although the stainless steel tubing has a low conduction coefficient and was shielded there are still significant losses not included in the model. Placing the coiled tube heat exchanger in the molten salt bath and using a wire k-thermocouple to measure the exit flow stream temperature reduced the extraction error by ten percent between *P-I* and *P-III*. The duration of extraction increases with each prototype. The thermal loss rate model is accurate within 28.9 %, 28.7 %, and 24.7 % respectively. The proposed model over estimates the extracted power and under estimates the thermal losses.

Several recommendations can be made based on the experimental results and existing technology. The first recommendation is not to pump molten salt out of the container and change the working fluid to a gaseous medium that is non-reactive with the salt or a working fluid that can not solidify in the pump and is non-reactive with the salt. The flow rate of a gaseous working fluid may be higher in order to be able to remove as much energy as its liquid counterpart. One foreseen challenge in changing from fluid to gas is finding a high temperature air pump. Further work needs to be explored for high temperature working fluids. Complexity in the heat exchangers can be as simple as tubing along the inside walls of the molten salt bath. A third recommendation is to continue the work on the single tank separated by a raft to isolate the cold side from the hot side.

Innovations made during this study include: 1) the high temperature PIV system to characterize convection cells, 2) charactering the effect of "additives" to the salt to reduce initial melt time, and 3) using spheres for the start up process. The study proved successful at accomplishing the following: 1) heating salt with solar simulator, 2) verify heat removal concept, 3) verify heat loss model, and 4) characterized heat removal from molten salt bath.

10. Future Work

One recommendation for future work is to use the high temperature cast Zircar insulation to test the quality of the insulation and its properties when in contact with the nitrate salt. Additional work also needs to be done in the detailed design and implementation of a high temperature PIV system. The PIV system can be used in conjunction with a finite element analysis model to predict alternative design parameters.

Future work should also look at building on the Navier Stokes derived convection program for comparing PIV measurements to theoretical behavior. Attempts were made to model the molten salt convection using the finite element package ADINA. However, the attempt was unsuccessful since ADINA does not have the feature of delivering an energy spectrum, or applying an energy absorption curve to a medium. There is a program written in C by JC Nave that uses the Navier Stokes equation that models the convection in the CSPonD molten salt.

11. Works Cited

[1] Afloresm. Solucar Platform PS10: The first commercial tower of the world. http://www.abengoasolar.com/corp/web/en/our_projects/solucar/ps10/index.html ((May 10, 2010)

[2] Andasol I with NREL site http://www.nrel.gov/csp/solarpaces/project_detail.cfm/projectID=3

[3] Coastal Chemical Company Brochure of Hitech Solar Salt.

[4] Codd, D., Carlson, A., Rees, J., Slocum, A. (2010) A Low Cost High Flux Solar Simulator. Submitted to Solar Energy pending review.

[5] Cravalho, E. *2.006 Thermal Fluid Engineering II.* Printed Spring 2008.

[6] Epstein, M., Segal, A., Yogev, A., "A molten salt system with ground base-integrated solar receiver storage tank. (Journal De Physique , France 9 (1999) Pr3- 95-104

[7] Figueredo, S. MIT MechE PhD 2011

[8] Glicksman and Lienhard *Modeling and Approximation Het Transfer* MIT Coop Printed course.

[9] Kolb, G., "Economic evaluation of solar only and hybrid power towers using molten salt technology," ibid pp 99-124.

[10] McAdams, W.H., in Heat Transmission (McGraw-Hill, New York 1954) 3rd ed p 242.

[11] Noone, C., Mitsos, A., "Optimization of heliostat field layout for hillside configurations" August 2010 {Submitted}

[12] Noone, C., Ghobeity, A., Slocum, A., Tzamtzis, G., Mitsos, A., "Site Selection for Hillside Central Receiver Solar thermal Plants" September 2010 {Submitted}

[13] Passerini, S., "Optical and Chemical Properties of Molten Salt Mixtures for Use in High Temperature Power Systems" M.S. Nuclear Engineering at the Massachusetts Institute of Technology (May 2010)

[14] Slocum, A. Codd, D., Buongiorno, J., Forsberg, C., McKrell, T., Nave, J., Papanicolas, C.N., Ghobeity, A., Noone, C., Passerini, S., Rojas, F., Mitsos, A., "Concentrated Solar Power on Demand" Septemeber 2010 {Submitted to Science for Publication}

[15] Srisawad, K., Wongwises, S., "Heat transfer characteristics of a new hically coiled crimped spriral finned tube heat exchanger, Springer Verlag 2008 Sept 27.

[16] Zircar Insulation http://www.zircarceramics.com/pages/rigidmaterials/specs/zal45.htm